ISSN 2413-5577

№ 3 Июль – Сентябрь 2022

Экологическая безопасность прибрежной и шельфовой зон моря

Ecological Safety of Coastal and Shelf Zones of Sea

No. 3 July – September 2022

ecological-safety.ru

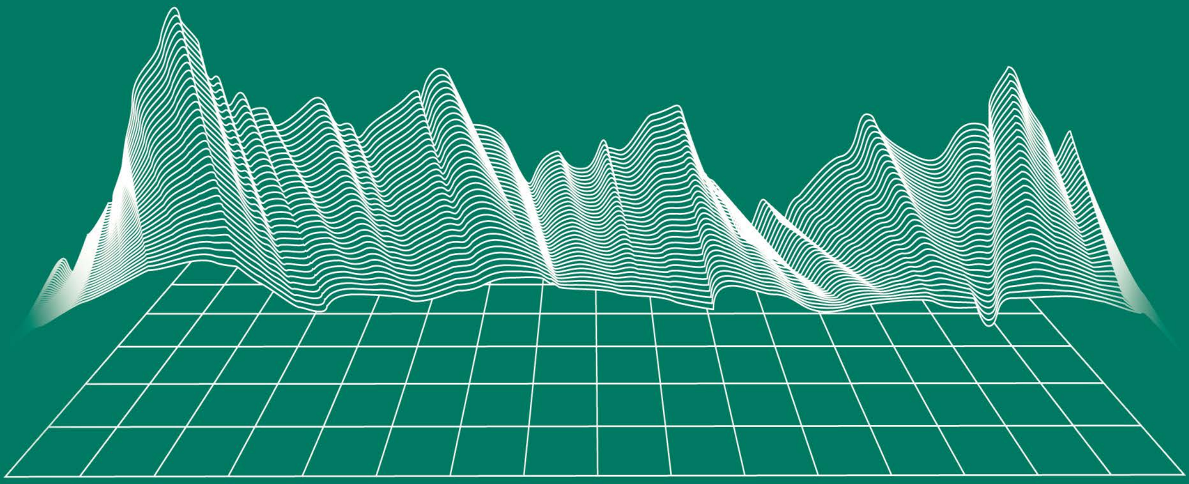

No. 3, 2022
July – September

Publication frequency:
Quarterly

16+

ECOLOGICAL SAFETY OF COASTAL AND SHELF ZONES OF SEA

Scientific and theoretical peer reviewed journal

FOUNDER AND PUBLISHER:
Federal State Budget Scientific Institution
Federal Research Centre
“Marine Hydrophysical Institute of RAS”

The Journal publishes original research results, review articles (at the editorial board's request) and brief reports.

The Journal aims at publication of results of original scientific research concerning the state and interaction of geospheres (atmosphere, lithosphere, hydrosphere, and biosphere) within coastal and shelf areas of seas and oceans, methods and means of study thereof, ecological state of these areas under anthropogenic load as well as environmental protection issues.

The Journal's editorial board sees its mission as scientific, educational and regulatory work to preserve the ecological balance and restore the resource potential of coastal and shelf areas believing that despite the geographical limitations of the areas under study, the processes taking place within them have a significant impact on the waters of the seas and oceans and economic activity.

The Journal publishes original research materials, results of research performed by national and foreign scientific institutions in the coastal and shelf zones of seas and oceans, review articles (at the editorial board's request) and brief reports on the following major topics:
- Scientific basis for complex use of shelf natural resources
- Marine environment state and variability
- Coastal area state and variability; coast protection structures
- Monitoring and estimates of possible effects of anthropogenic activities
- Development and implementation of new marine environment control and monitoring technologies

The outcome of the research is information on the status, variability and possible effects of anthropogenic activities in the coastal and shelf marine areas, as well as the means to perform calculations and to provide information for making decisions on the implementation of activities in the coastal zone.

e-mail: ecology-safety@mhi-ras.ru

website: http://ecological-safety.ru

Founder, Publisher and Editorial Office address:
2, Kapitanskaya St.,
Sevastopol, 299011, Russia

Phone, fax: + 7 (8692) 54-57-16

EDITORIAL BOARD

Yuri N. Goryachkin – **Editor-in-Chief**, Chief Research Associate of FSBSI FRC MHI, Dr.Sci. (Geogr.), Scopus ID: 6507545681, ResearcherID: I-3062-2015, ORCID 0000-0002-2807-201X (Sevastopol, Russia)

Vitaly I. Ryabushko – **Deputy Editor-in-Chief**, Head of Department of FSBSI FRC A. O. Kovalevsky Institute of Biology of the Southern Seas of RAS, Chief Research Associate, Dr.Sci. (Biol.), ResearcherID: H-4163-2014, ORCID ID: 0000-0001-5052-2024 (Sevastopol, Russia)

Elena E. Sovga – **Deputy Editor-in-Chief**, Leading Research Associate of FSBSI FRC MHI, Dr.Sci. (Geogr.), Scopus ID: 7801406819, ResearcherID: A-9774-2018 (Sevastopol, Russia)

Vladimir V. Fomin – **Deputy Editor-in-Chief**, Head of Department of FSBSI FRC MHI, Dr.Sci. (Phys.-Math.), ResearcherID: H-8185-2015, ORCID ID: 0000-0002-9070-4460 (Sevastopol, Russia)

Tatyana V. Khmara – **Executive Editor**, Junior Research Associate of FSBSI FRC MHI, Scopus ID: 6506060413, ResearcherID: C-2358-2016 (Sevastopol, Russia)

Vladimir N. Belokopytov – Leading Research Associate, Head of Department of FSBSI FRC MHI, Dr.Sci. (Geogr.), Scopus ID: 6602809060, ORCID ID: 0000-0003-4699-9588 (Sevastopol, Russia)

Sergey V. Berdnikov – Chairman of FSBSI FRC Southern Scientific Centre of RAS, Dr.Sci. (Geogr.), ORCID ID: 0000-0002-3095-5532 (Rostov-on-Don, Russia)

Valery G. Bondur – Director of FSBSI Institute for Scientific Research of Aerospace Monitoring “AEROCOSMOS”, vice-president of RAS, academician of RAS, Dr.Sci. (Tech.), ORCID ID: 0000-0002-2049-6176 (Moscow, Russia)

Elena F. Vasechkina – Deputy Director of FSBSI FRC MHI, Dr.Sci. (Geogr.), ResearcherID: P-2178-2017 (Sevastopol, Russia)

Isaac Gertman – Head of Department of Israel Oceanographic and Limnological Research Institute, Head of Israel Marine Data Center, Ph.D. (Geogr.), ORCID ID: 0000-0002-6953-6722 (Haifa, Israel)

Sergey G. Demyshev – Head of Department of FSBSI FRC MHI, Chief Research Associate, Dr.Sci. (Phys.-Math.), ResearcherID C-1729-2016, ORCID ID: 0000-0002-5405-2282 (Sevastopol, Russia)

Nikolay A. Diansky – Chief Research Associate of Lomonosov Moscow State University, associate professor, Dr.Sci. (Phys.-Math.), ResearcherID: R-8307-2018, ORCID ID: 0000-0002-6785-1956 (Moscow, Russia)

Vladimir A. Dulov – Head of Laboratory of FSBSI FRC MHI, professor, Dr.Sci. (Phys.-Math.), ResearcherID: F-8868-2014, ORCID ID: 0000-0002-0038-7255 (Sevastopol, Russia)

Victor N. Egorov – Scientific Supervisor of FSBSI FRC A. O. Kovalevsky Institute of Biology of the Southern Seas of RAS, academician of RAS, professor, Dr.Sci. (Biol.), ORCID ID: 0000-0002-4233-3212 (Sevastopol, Russia)

Vladimir V. Efimov – Head of Department of FSBSI FRC MHI, Dr.Sci. (Phys.-Math.), ResearcherID: P-2063-2017 (Sevastopol, Russia)

Vladimir B. Zalesny – Leading Research Associate of FSBSI Institute of Numerical Mathematics of RAS, professor, Dr.Sci. (Phys.-Math.), ORCID ID: 0000-0003-3829-3374 (Moscow, Russia)

Andrey G. Zatsepin – Head of Laboratory of P.P. Shirshov Institute of Oceanology of RAS, Chief Research Associate, Dr.Sci. (Phys.-Math.), ORCID ID: 0000-0002-5527-5234 (Moscow, Russia)

Vasiliy V. Knysh – Leading Research Associate of FSBSI FRC MHI, professor, Dr.Sci. (Phys.-Math.), ResearcherID: B-3603-2018 (Sevastopol, Russia)

Sergey K. Konovalov – Director of FSBSI FRC MHI, corresponding member of RAS, Dr.Sci. (Geogr.), ORCID ID: 0000-0002-5200-8448 (Sevastopol, Russia)

Gennady K. Korotaev – Scientific Supervisor of FSBSI FRC MHI, corresponding member of RAS, professor, Dr.Sci. (Phys.-Math.), ResearcherID: K-3408-2017 (Sevastopol, Russia)

Ruben D. Kosyan – Chief Research Associate of Southern Branch of P.P. Shirshov Institute of Oceanology of RAS, professor, Dr.Sci. (Geogr.), ORCID ID: 0000-0003-0788-6644 (Gelendzhik, Russia)

Alexander S. Kuznetsov – Leading Research Associate, Head of Department of FSBSI FRC MHI, Ph.D. (Tech.), ORCID ID: 0000-0002-5690-5349 (Sevastopol, Russia)

Michael E. Lee – Head of Department of FSBSI FRC MHI, Dr.Sci. (Phys.-Math.), professor, ORCID ID: 0000-0002-2292-1877 (Sevastopol, Russia)

Ludmila V. Malakhova – Leading Research Associate of A. O. Kovalevsky Institute of Biology of the Southern Seas of RAS, Ph.D. (Biol.), ResearcherID: E-9401-2016, ORCID: 0000-0001-8810-7264 (Sevastopol, Russia)

Gennady G. Matishov – Deputy Academician – Secretary of Earth Sciences Department of RAS, Head of Section of Oceanology, Physics of Atmosphere and Geography, Scientific Supervisor of FSBSI FRC Southern Scientific Centre of RAS, Scientific Supervisor of FSBSI Murmansk Marine Biological Institute KSC of RAS, academician of RAS, Dr.Sci. (Geogr.), professor, ORCID ID: 0000-0003-4430-5220 (Rostov-on-Don, Russia)

Sergey V. Motyzhev – Chief Research Associate of Sevastopol State University, Dr.Sci. (Tech.), ResearcherID: G-2784-2014, ORCID ID: 000 0-0002-8438-2602 (Sevastopol, Russia)

Alexander V. Prazukin – Leading Research Associate of FSBSI FRC A. O. Kovalevsky Institute of Biology of the Southern Seas of RAS, Dr.Sci. (Biol.), ResearcherID: H-2051-2016, ORCID ID: 0000-0001-9766-6041 (Sevastopol, Russia)

Anatoly S. Samodurov – Head of Department of FSBSI FRC MHI, Dr.Sci. (Phys.-Math.), ResearcherID: V-8642-2017 (Sevastopol, Russia)

Dimitar I. Trukhchev – Institute of Metal Science, equipment, and technologies “Academician A. Balevski” with Center for Hydro- and Aerodynamics at the Bulgarian Academy of Sciences, Dr.Sci. (Phys.-Math.), professor (Varna, Bulgaria)

Naum B. Shapiro – Leading Research Associate of FSBSI FRC MHI, Dr.Sci. (Phys.-Math.), ResearcherID: A-8585-2017 (Sevastopol, Russia)

РЕДАКЦИОННАЯ КОЛЛЕГИЯ

Горячкин Юрий Николаевич – **главный редактор**, главный научный сотрудник ФГБУН ФИЦ МГИ, д. г. н., Scopus Author ID: 6507545681, ResearcherID: I-3062-2015, ORCID ID: 0000-0002-2807-201X (Севастополь, Россия)

Рябушко Виталий Иванович – **заместитель главного редактора**, заведующий отделом ФГБУН ФИЦ «ИнБЮМ им. А.О. Ковалевского РАН», главный научный сотрудник, д. б. н., ResearcherID: H-4163-2014, ORCID ID: 0000-0001-5052-2024 (Севастополь, Россия)

Совга Елена Евгеньевна – **заместитель главного редактора**, ведущий научный сотрудник ФГБУН ФИЦ МГИ, д. г. н., Scopus Author ID: 7801406819, ResearcherID: A-9774-2018 (Севастополь, Россия)

Фомин Владимир Владимирович – **заместитель главного редактора**, заведующий отделом ФГБУН ФИЦ МГИ, д. ф.-м. н., ResearcherID: H-8185-2015, ORCID ID: 0000-0002-9070-4460 (Севастополь, Россия)

Хмара Татьяна Викторовна – **ответственный секретарь**, младший научный сотрудник ФГБУН ФИЦ МГИ, Scopus Author ID: 6506060413, ResearcherID: C-2358-2016 (Севастополь, Россия)

Белокопытов Владимир Николаевич – ведущий научный сотрудник, заведующий отделом ФГБУН ФИЦ МГИ, д. г. н., Scopus Author ID: 6602809060, ORCID ID: 0000-0003-4699-9588 (Севастополь, Россия)

Бердников Сергей Владимирович – председатель ФГБУН ФИЦ ЮНЦ РАН, д. г. н., ORCID ID: 0000-0002-3095-5532 (Ростов-на-Дону, Россия)

Бондур Валерий Григорьевич – директор ФГБНУ НИИ «АЭРОКОСМОС», вице-президент РАН, академик РАН, д. т. н., ORCID ID: 0000-0002-2049-6176 (Москва, Россия)

Васечкина Елена Федоровна – заместитель директора ФГБУН ФИЦ МГИ, д. г. н., ResearcherID: P-2178-2017 (Севастополь, Россия)

Гертман Исаак – глава департамента Израильского океанографического и лимнологического исследовательского центра, руководитель Израильского морского центра данных, к. г. н., ORCID ID: 0000-0002-6953-6722 (Хайфа, Израиль)

Демышев Сергей Германович – заведующий отделом ФГБУН ФИЦ МГИ, главный научный сотрудник, д. ф.-м. н., ResearcherID: C-1729-2016, ORCID ID: 0000-0002-5405-2282 (Севастополь, Россия)

Дианский Николай Ардальянович – главный научный сотрудник МГУ им. М. В. Ломоносова, доцент, д. ф.-м. н., ResearcherID: R-8307-2018, ORCID ID: 0000-0002-6785-1956 (Москва, Россия)

Дулов Владимир Александрович – заведующий лабораторией ФГБУН ФИЦ МГИ, профессор, д. ф.-м. н., ResearcherID: F-8868-2014, ORCID ID: 0000-0002-0038-7255 (Севастополь, Россия)

Егоров Виктор Николаевич – научный руководитель ФГБУН ФИЦ ИнБЮМ им. А.О. Ковалевского РАН, академик РАН, профессор, д. б. н., ORCID ID: 0000-0002-4233-3212 (Севастополь, Россия)

Ефимов Владимир Васильевич – заведующий отделом ФГБУН ФИЦ МГИ, д. ф.-м. н., ResearcherID: P-2063-2017 (Севастополь, Россия)

Залесный Владимир Борисович – ведущий научный сотрудник ФГБУН ИВМ РАН, профессор, д. ф.-м. н., ORCID ID: 0000-0003-3829-3374 (Москва, Россия)

Зацепин Андрей Георгиевич – руководитель лаборатории ФГБУН ИО им. П.П. Ширшова РАН, главный научный сотрудник, д. ф.-м. н., ORCID ID: 0000-0002-5527-5234 (Москва, Россия)

Кныш Василий Васильевич – ведущий научный сотрудник ФГБУН ФИЦ МГИ, профессор, д. ф.-м. н., Researcher ID: B-3603-2018 (Севастополь, Россия)

Коновалов Сергей Карпович – директор ФГБУН ФИЦ МГИ, член-корреспондент РАН, д. г. н., ORCID ID: 0000-0002-5200-8448 (Севастополь, Россия)

Коротаев Геннадий Константинович – научный руководитель ФГБУН ФИЦ МГИ, член-корреспондент РАН, профессор, д. ф.-м. н., ResearcherID: K-3408-2017 (Севастополь, Россия)

Косьян Рубен Дереникович – главный научный сотрудник ЮО ИО РАН, профессор, д. г. н., ORCID ID: 0000-0003-0788-6644 (Геленджик, Россия)

Кузнецов Александр Сергеевич – ведущий научный сотрудник, заведующий отделом ФГБУН ФИЦ МГИ, к. т. н., ORCID ID: 0000-0002-5690-5349 (Севастополь, Россия)

Ли Михаил Ен Гон – заведующий отделом ФГБУН ФИЦ МГИ, профессор, д. ф.-м. н., ORCID ID: 0000-0002- 2292-1877 (Севастополь, Россия)

Малахова Людмила Васильевна – ведущий научный сотрудник ФГБУН ФИЦ ИнБЮМ им. А.О. Ковалевского РАН, к. б. н., ResearcherID: E-9401-2016, ORCID ID: 0000-0001-8810-7264 (Севастополь, Россия)

Матишов Геннадий Григорьевич – заместитель академика-секретаря Отделения наук о Земле РАН – руководитель Секции океанологии, физики атмосферы и географии, научный руководитель ФГБУН ФИЦ ЮНЦ РАН, научный руководитель ФГБУН ММБИ КНЦ РАН, академик РАН, д. г. н., профессор, ORCID ID: 0000-0003-4430-5220 (Ростов-на-Дону, Россия)

Мотыжев Сергей Владимирович – главный научный сотрудник СевГУ, д. т. н., ResearcherID: G-2784-2014, ORCID ID: 0000-0002-8438-2602 (Севастополь, Россия)

Празукин Александр Васильевич – ведущий научный сотрудник ФГБУН ФИЦ ИнБЮМ им. А.О. Ковалевского РАН, д. б. н., Researcher ID: H-2051-2016, ORCID ID: 0000-0001-9766-6041 (Севастополь, Россия)

Самодуров Анатолий Сергеевич – заведующий отделом ФГБУН ФИЦ МГИ, д. ф.-м. н., ResearcherID: V-8642-2017 (Севастополь, Россия)

Трухчев Димитър Иванов – старший научный сотрудник Института океанологии БАН, профессор, д. ф.-м. н. (Варна, Болгария)

Шапиро Наум Борисович – ведущий научный сотрудник ФГБУН ФИЦ МГИ, д. ф.-м. н., ResearcherID: A-8585-2017 (Севастополь, Россия)

CONTENTS

№ 3. 2022 July – September, 2022

СОДЕРЖАНИЕ

№ 3. 2022 Июль – Сентябрь, 2022

DOI: 10.22449/2413-5577-2022-3-6-15

Probability of the Appearance of Abnormal Waves in the Coastal Zone of the Black Sea at the Southern Coast of Crimea

A. S. Zapevalov *, A. V. Garmashov

Marine Hydrophysical Institute of RAS, Sevastopol, Russia
**e-mail: sevzepter@mail.ru*

Abstract

The paper analyzes the probability of appearance of abnormal waves in the coastal zone of the Black Sea. The analysis is based on the data of wave measurements carried out on a stationary oceanographic platform of the Marine Hydrophysical Institute of RAS. Two indices were used to identify abnormal waves. The first index AI is the ratio of the maximum and significant wave heights, the second index CI is the ratio of the maximum crest height and significant wave height. The values of the AI index are mainly in the range from 1.25 to 2.75, the values of the CI index are in the range from 0.7 to 1.5. It is shown that both indices are statistically independent of the steepness and the skewness, a high correlation is observed only with the excess kurtosis λ_4. The correlation coefficients between AI and λ_4 and between CI and λ_4 are 0.57 and 0.49, respectively. The probability of appearance of abnormal waves calculated on the basis of the AI index is higher than that calculated on the basis of the CI index. This is explained by the fact that there are three forms of abnormal waves, which are identified as follows: positive form, whose crest is more than 50 % higher than its trough with respect to the mean sea level, negative form, whose troughs are more than 50 % greater than their crests and a sign-variable form (intermediate). The CI index does not allow distinguishing abnormal waves of a negative form and not always distinguishes abnormal waves of a sign-variable form. The correlation coefficient between indices AI and CI is 0.64.

Keywords: abnormal wave, abnormality index, steepness, skewness, excess kurtosis, Black Sea

Acknowledgments: the work was carried out under state assignment of FSBSI FRC MHI no. FNNN-2021-0003, no. FNNN-2022-0003.

For citation: Zapevalov, A.S. and Garmashov, A.V., 2022. Probability of the Appearance of Abnormal Waves in the Coastal Zone of the Black Sea at the Southern Coast of Crimea. *Ecological Safety of the Coastal and Shelf Zones of the Sea*, (3), pp. 6–15. doi:10.22449/2413-5577-2022-3-6-15

Вероятность появления аномальных волн в прибрежной зоне Черного моря у Южного берега Крыма

А. С. Запевалов *, А. В. Гармашов

Морской гидрофизический институт РАН, Севастополь, Россия
**e-mail: sevzepter@mail.ru*

Аннотация

Проведен анализ вероятности появления аномальных волн в прибрежной зоне Черного моря. Анализ основан на данных волновых измерений, проведенных на стационарной океанографической платформе Морского гидрофизического института РАН. Для выделения аномальных волн использовались два индекса. Первый индекс AI является соотношением максимальной и значимой высот волн, второй индекс CI является отношением максимальной высоты гребня и значимой высоты волн. Значения индекса AI в основном лежат в пределах от 1.25 до 2.75, значения индекса CI – в пределах от 0.7 до 1.5. Показано, что оба индекса статистически не зависят от крутизны волн и коэффициента асимметрии, высокая корреляция наблюдается только с коэффициентом эксцесса λ_4. Коэффициенты корреляции между AI и λ_4 и между CI и λ_4 соответственно равны 0.57 и 0.49. Вероятность появления аномальных волн, рассчитанная на основе индекса AI, выше, чем рассчитанная на основе индекса CI. Это объясняется тем, что существуют три формы аномальных волн, которые идентифицируются следующим образом: положительная, при которой высота гребня в полтора раза больше глубины впадины, отрицательная, при которой глубины впадины в полтора раза больше высоты гребня, и знакопеременная (промежуточная). Индекс CI не позволяет выделять аномальные волны отрицательной формы и не во всех ситуациях выделяет аномальные волны знакопеременной формы. Коэффициент корреляции между индексами AI и CI равен 0.64.

Ключевые слова: аномальные волны, индекс аномальности, крутизна, коэффициент асимметрии, коэффициент эксцесса, Черное море

Благодарности: работа выполнена в рамках государственного задания ФГБУН ФИЦ МГИ № FNNN-2021-0003, № FNNN-2022-0003.

Для цитирования: *Запевалов А. С., Гармашов А. В.* Вероятность появления аномальных волн в прибрежной зоне Черного моря у Южного берега Крыма // Экологическая безопасность прибрежной и шельфовой зон моря. 2022. № 3. С. 6–15. doi:10.22449/2413-5577-2022-3-6-15

Introduction

Despite their long history, the studies of the conditions resulting in the appearance of abnormally high waves have been continuing to attract increased attention. Several physical mechanisms can answer for the appearance of abnormally high waves [1, 2]. In deep water, such mechanisms are as follows: modulation instability of wave packets [3, 4]; nonlinear dispersive focusing [5, 6]; interaction with currents [7]; geometric focusing and nonlinear interaction of nonparallel wave systems [8, 9].

To identify abnormal waves such a criterion as AI (abnormality index) is used [10–12]

$$\mathrm{AI} = H_{\max} / H_S ,$$

where $H_{\max}$ – maximum wave height during the measurement period; H_S – significant wave height equal to the average height of one third of the highest waves. The waves with their height, which is more than two times greater than the significant height of background waves, i.e. the waves, for which the following condition is satisfied:

$$\mathrm{AI} > 2 , \qquad (1)$$

are considered to be abnormal ones. In recent years, intensive attempts have been made to find a relationship between the appearance of abnormal waves and the characteristics of the sea surface state [12].

The probability that AI > 2 (it will be denoted as P_A) varies over a broad area depending on the region, which is possible due to the variety of physical mechanisms resulting in the appearance of abnormal waves. Measurements taken off the western coast of India show P_A = 0.46 % [11]. Measurements taken under stormy conditions with a downward radar on two platforms in the North Sea, with a wave recorder on a platform in the Gulf of Mexico, and with a wave buoy off the coast of Portugal, show that the average P_A makes 3.6 % [13].

The purpose of this work is to analyze the dependence of the AI index on the integral parameters characterizing the state of the sea surface in the coastal zone of the Black Sea.

Measurements of wave parameters and measurement conditions

The surface wave measurements were carried out on a stationary oceanographic platform of the Marine Hydrophysical Institute of RAS located in the coastal zone of the Black Sea, near the South Coast of Crimea. The minimum distance from the platform to the coastline makes about 600 m. The depth of the sea at the point where the platform is located makes about 30 m. To measure the parameters of the waves, a resistive wave recorder was used, with its sensor represented by a nichrome string wound with fixed spacing on the carrying wireline. To minimize the effect of sea surface disturbances created by the platform supports, wave measurements were carried out at a point at least 6 m away from the nearest support. The description of the measuring equipment and conditions for carrying out measurements on a stationary oceanographic platform is given in [14–17].

Wave and wind speed measurements were carried out regularly from 01.05.2018 to 31.01.2019 with several short breaks. Continuous measurements were divided into periods lasting 20 min. For each period, the statistical characteristics of the waves were calculated, as well as the average wind speed and direction. The total amount of data is more than 17,000 measurement periods.

During the whole period, the wind speed varied from free from rough activity of water to 26 m/s, with the maximum significant wave height H_S – 2.3 m, and the maximum wave height $H_{\max}$ – up to 5.0 m. The probability density empirical

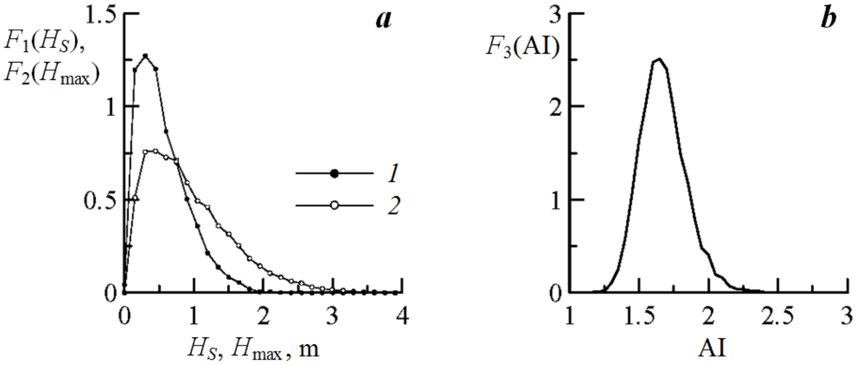

Fig. 1. Distributions of surface wave characteristics during the measurement period: *a* – significant wave height $F_1(H_S)$ (curve *1*) and maximum height $F_2(H_{max})$ (curve *2*), *b* – abnormality index F_3(AI)

functions of these wave parameters denoted as $F_1(H_S)$ and $F_2(H_{max})$ are shown in Fig. 1. Fig. 1 also shows the probability density empirical function of the abnormality index $F_3(AI)$.

The AI values obtained for the coastal zone of the Black Sea lie in the following range: 1.1 < AI < 2.8. The probability of occurrence of abnormal waves with AI > 2 made 3.3 %.

Correlation of AI abnormality index with steepness and skewness

Nonlinear physical mechanisms result in the appearance of abnormal waves [12]. To compare the relative level of nonlinearity, the steepness of the waves is used [18, 19]. The steepness of gravity waves in deep water satisfying the dispersion relation $\omega^2 = gk$ is defined as follows

$$\varepsilon = \sqrt{\overline{\xi^2}}k_0 = \sqrt{\overline{\xi^2}}\,\omega_0{}^2/g\,,$$

where $\overline{\xi^2}$ – sea surface elevation dispersion; k – wave number; ω – frequency; g – gravitational acceleration; index “0” means that this parameter corresponds to a peak in the wave spectrum.

The correlation between the abnormality index and the steepness of the waves is shown in Fig. 2. It can be seen that AI is almost independent of the steepness of the waves. The correlation coefficient between AI and ε makes 0.06.

A consequence of the nonlinearity of sea surface waves is the deviation of the distribution of sea surface elevations from the Gauss distribution. The main parameters that describe the effect of nonlinearity on the geometric characteristics of waves are skewness and excess kurtosis [9, 19], which can be used as a measure

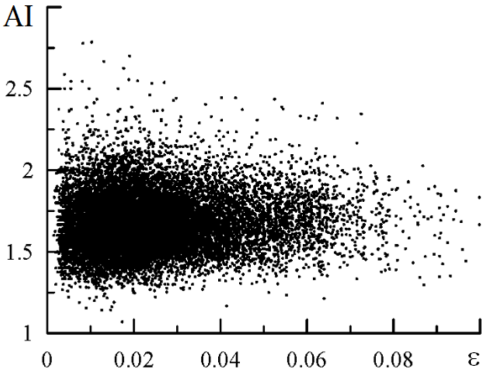

Fig. 2. Dependence of the abnormality index AI on the steepness ε

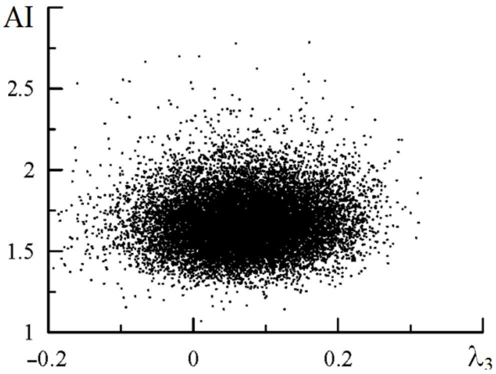

Fig. 3. Dependence of the abnormality index AI on the skewness λ_3

of nonlinearity [3]. For a random variable ξ with zero mean, the skewness is as follows

$$\lambda_3 = \overline{\xi^3} \Big/ \overline{\xi^2}^{\,3/2},$$

where the overbar means averaging.

The correlation between the abnormality index and the skewness is shown in Fig. 3. The correlation coefficient between AI and λ_3 makes 0.06.

Within the framework of the analysis of various physical mechanisms, a number of theoretical works showed that an increase in the excess kurtosis should lead to an increase in the probability of the appearance of abnormal waves [5, 20]. The excess kurtosis is as follows

$$\lambda_4 = \overline{\xi^4} \Big/ \overline{\xi^2}^{\,2} - 3.$$

As Fig. 4 shows, the general trend is the AI growth with the increase of λ_4. The correlation coefficient between AI and λ_4 makes 0.57. The linear regression describing the dependence of the AI index on the excess kurtosis, has the following form

$$\mathrm{AI} = 0.628\lambda_4 + 1.665. \quad (2)$$

The standard deviation makes 0.10. In previous studies, the following close regression dependences were obtained:

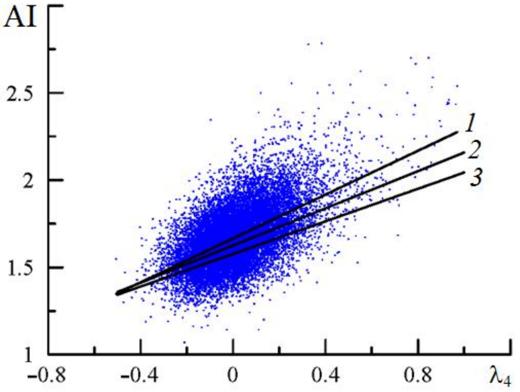

Fig. 4. Dependence of the abnormality index AI on the excess kurtosis λ_4. Lines 1–3 correspond to regressions (2)–(4)

in [13]

$$\mathrm{AI} = 0.533\lambda_4 + 1.625 \tag{3}$$

and in [10]

$$\mathrm{AI} = 0.467\lambda_4 + 1.577\ . \tag{4}$$

The dependence of the AI index on λ_4 was also observed in a storm in the Black Sea studied in detail (autumn 2009) [21].

Thus, of three parameters considered here (ε, λ_3, λ_4), only the excess kurtosis is statistically related to the abnormality index.

Correlation of the abnormality index with the height of the wave crest

Along with the condition $\mathrm{AI} > 2$ to identify the abnormal waves, condition [12] is sometimes used

$$\mathrm{CI} = C_{\max} / H_S > 1.25\,, \tag{5}$$

where $C_{\max}$ – maximum crest height. The crest height is defined as the highest point on the wave line for the period between two consecutive crossings of the mean water level from bottom to top and from top to bottom [6].

The dependences of the CI index on the parameters characterizing the wave nonlinearity are shown in Fig. 5. For the calculations, the same data array was used as for the AI calculations. The correlation coefficients between CI and ε, λ_3, λ_4 make 0.09, 0.13 and 0.49, correspondingly. The dependence

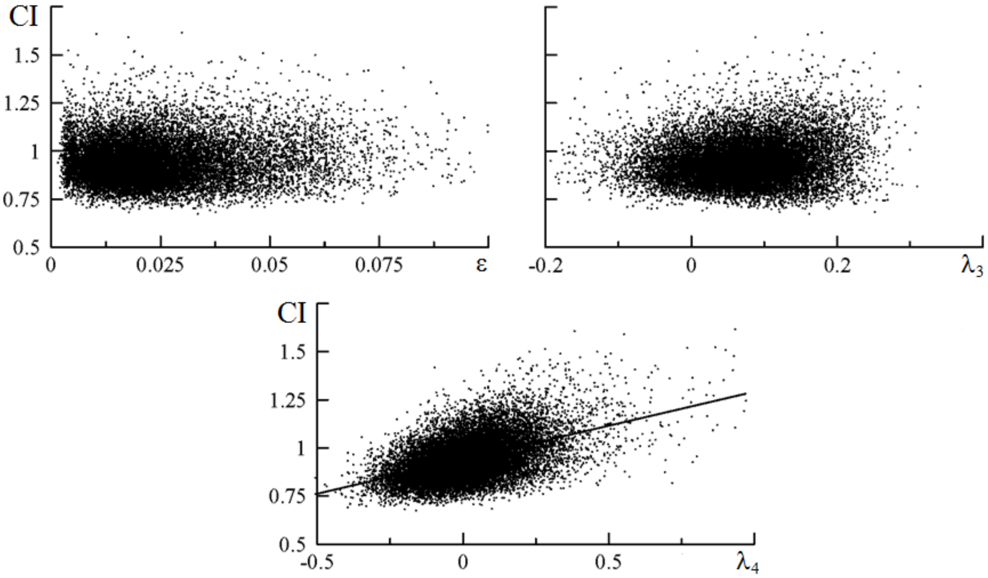

Fig. 5. Dependencies of the index CI on the parameters ε, λ_3 and λ_4. The line on the lower fragment corresponds to regression (6)

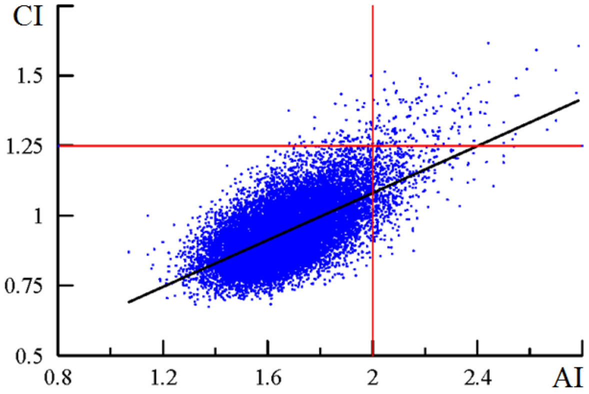

Fig. 6. Interrelation of indices AI and CI. The red lines show the critical values of the indices, above which the wave is considered abnormal, the black line is the regression (7)

of CI on λ_4 can be approximated by the following linear regression

$$\mathrm{CI} = 0.353\lambda_4 + 0.939\,, \qquad (6)$$

with standard deviation equal to 0.10.

Let us consider the relationship between AI and CI indices, which is shown in Fig. 6. The correlation coefficient between these indices makes 0.64. The relationship between AI and CI indices is described by the following linear regression

$$\mathrm{CI} = 0.42\mathrm{AI} + 0.241 \qquad (7)$$

with standard deviation equal to 0.085.

Let us compare the probability of occurrence of abnormal waves determined in accordance with criteria (1) and (5). The number of points above the horizontal red line in Fig. 6 is noticeably smaller than those lying to the right of the vertical red line. This means that the probability of the appearance of an abnormal wave in accordance with criterion (5) (it will be denoted as P_C) is less than that with criterion (1). For the data array analyzed here, P_C = 1.3 % and P_A = 3.3 %.

Such a discrepancy in the estimates of the probability of the appearance of abnormal waves can be explained as follows. By the analogy with the determination of the crest height, we define the depth of the trough as the distance from the average water level to the lowest point on the wave profile for the period between two successive crossings of the average level from top to bottom and from bottom to top. There are three main forms of abnormal waves: positive, negative and sign-variable [11, 22]. Positive is the form in which the height of the crest is one and a half times more than the depth of the trough. Correspondingly, the form is negative, when the depth of the trough is one and a half times more than the height of the crest. The form with an intermediate ratio of the height of the crest and the depth of the trough is called sign-variable. According to the data of measurements in the coastal zone of the Baltic Sea (with the depth of 2.7 m), 63 % of abnormal waves had a positive form, 19.5 % had a sign-variable form, and 17.5 % had a negative form [22].

It should be noted that within the framework of the standard procedures for the calculation of the AI and CI indices, the characteristics of the largest of the abnormal waves are determined. This procedure does not take into account that several abnormal waves can take place during a measurement period.

Conclusion

Based on *in situ* wave measurements, the analysis was made concerning the appearance of abnormal waves in the coastal zone of the Black Sea. Two indices were used to identify abnormal waves. The first index is equal to the ratio of the maximum and significant wave heights AI, while the second index represents the ratio of the maximum crest height to the significant wave height CI.

It is shown that the AI and CI indices do not depend on the steepness of the waves and on the skewness of the sea surface elevations. A statistical correlation was found only for the excess kurtosis, which makes it possible to use it as a predictor in the problems on the forecast of the appearance of abnormal waves.

It is also shown that the probability of appearance of abnormal waves calculated on the basis of the AI index is higher than that calculated on the basis of the CI index. This is explained by the fact that there are three forms of abnormal waves, which are identified by different correlation of the height of the crest and the depth of the trough. The CI index allows distinguishing effectively only abnormal waves with their height of the crest greater than the depth of the trough.

REFERENCES

1. Divinsky, B.V., Levin, B.V., Lopatukhin, L.I., Pelinovsky, E.N. and Slyunyaev, A.V., 2004. A Freak Wave in the Black Sea: Observations and Simulation. *Doklady Earth Sciences*, 395(3), pp. 438–443.
2. Tao, A.-F., Peng, J., Zheng, J.-H., Wang, Y. and Wu, Y.-Q., 2015. Discussions on the Occurrence Probabilities of Observed Freak Waves. *Journal of Marine Science and Technology*, 23(6), pp. 923–928. doi:10.6119/JMST-015-0610-10
3. Janssen, P.A.E.M., 2003. Nonlinear Four-Wave Interactions and Freak Waves. *Journal of Physical Oceanography*, 33(4), pp. 863–884. https://doi.org/10.1175/1520-0485(2003)33<863:NFIAFW>2.0.CO;2
4. Ruban, V.P., 2013. Rogue Waves at Low Benjamin-Feir Indices: Numerical Study of the Role of Nonlinearity. *JETP Letters*, 97(12), pp. 686–689. https://doi.org/10.1134/S0021364013120096
5. Pelinovsky, E.N. and Shurgalina, E.G., 2016. Formation of Freak Waves in a Soliton Gas Described by the Modified Korteweg–de Vries Equation. *Doklady Physics*, 61(9), 423–426. doi:10.1134/S1028335816090032
6. Forristall, G.Z., 2005. Understanding Rogue Waves: Are New Physics Really Necessary? In: University of Hawaii, 2005. *Proceedings of the 14th ‘Aha Huliko’a Winter Workshop 2005 on Rogue Waves January 25–28, Honolulu, USA.* Honolulu: University of Hawaii. Available at: http://www.soest.hawaii.edu/PubServices/2005pdfs/foreword.pdf [Accessed: 8 August 2022].

7. Hjelmervik, K. and Trulsen, K., 2009. Freak Wave Statistics on Collinear Currents. *Journal of Fluid Mechanics*, 637, pp. 267–284. doi:10.1017/S0022112009990607
8. Semedo, A., Sušelj, K., Rutgersson, A. and Sterl, A., 2011. A Global View on the Wind Sea and Swell Climate and Variability from ERA-40. *Journal of Climate*, 24(5), pp. 1461–1479. doi:10.1175/2010JCLI3718.1
9. Luxmoore, J.F., Ilic S. and Mori, N., 2019. On Kurtosis and Extreme Waves in Crossing Directional Seas: a Laboratory Experiment. *Journal of Fluid Mechanics*, 876, pp. 792–817. doi:10.1017/jfm.2019.575
10. Guedes Soares, C., Cherneva, Z. and Antão, E.M., 2003. Characteristics of Abnormal Waves in North Storm Sea States. *Applied Ocean Research*, 25(6), pp. 337–344. doi:10.1016/j.apor.2004.02.005
11. Glejin, J., Kumar, V.S., Nair, T.M.B., Singh, J. and Nherakkol, A., 2014. Freak Waves off Ratnagiri, West Coast of India. *Indian Journal of Geo-Marine Sciences*, 43(7), pp. 1339–1342. Available at: http://nopr.niscpr.res.in/handle/123456789/34450 [Accessed: 8 August 2022].
12. Cattrell, A.D., Srokosz, M., Moat, B.I. and Marsh, R., 2018. Can Rogue Waves Be Predicted Using Characteristic Wave Parameters? *Journal of Geophysical Research: Oceans*, 123(8), pp. 5624–5636. doi:10.1029/2018JC013958
13. Guedes Soares, C., Cherneva, Z. and Antão, E.M., 2004. Steepness and Asymmetry of the Largest Waves in Storm Sea States. *Ocean Engineering*, 31(8–9), pp. 1147–1167. doi:10.1016/J.OCEANENG.2003.10.014
14. Toloknov, Yu.N. and Korovushkin, A.I., 2010. The System of Collecting Hydrometeorological Information. In: MHI, 2010. *Monitoring Systems of Environment*. Sevastopol: ECOSI-Gidrofizika. Iss. 13, pp. 50–53 (in Russian).
15. Efimov, V.V. and Komarovskaya, O.I., 2019. Disturbances in the Wind Speed Fields due to the Crimean Mountains. *Physical Oceanography*, 26(2), pp. 123–134. doi:10.22449/1573-160X-2019-2-123-134
16. Solov'ev, Y.P. and Ivanov, V.A., 2007. Preliminary Results of Measurements of Atmospheric Turbulence over the Sea. *Physical Oceanography*, 17(3), pp. 154–172. https://doi.org/10.1007/s11110-007-0013-9
17. Zapevalov, A.S. and Garmashov, A.V., 2022. The Appearance of Negative Values of the Skewness of Sea-Surface Waves. *Izvestiya, Atmospheric and Oceanic Physics*, 58(3), pp. 263–269. doi:10.1134/S0001433822030136
18. Fedele, F., Brennan, J., Ponce De León, S., Dudley, J. and Dias, F., 2016. Real World Ocean Rogue Waves Explained without the Modulational Instability. *Scientific Reports*, 6, 27715. doi:10.1038/srep27715
19. Zapevalov, A.S. and Garmashov, A.V., 2021. Skewness and Kurtosis of the Surface Wave in the Coastal Zone of the Black Sea. *Physical Oceanography*, 28(4), pp. 414–425. doi:10.22449/1573-160X-2021-4-414-425
20. Mori, N. and Janssen, P.A.E.M., 2006. On Kurtosis and Occurrence Probability of Freak Waves. *Journal of Physical Oceanography*, 36(7), pp. 1471–1483. doi:10.1175/JPO2922.1
21. Ivanov, V.A., Dulov, V.A., Kuznetsov, S.Yu., Dotsenko, S.F., Shokurov, M.V., Saprykina, Ya.V., Malinovsky, V.V. and Polnikov, V.G., 2012. Risk Assessment of Encountering Killer Waves in the Black Sea. *Geography, Environment, Sustainability*, 5(1), pp. 84–111. https://doi.org/10.24057/2071-9388-2012-5-1-84-111

22. Didenkulova, I. and Anderson, C., 2010. Freak Waves of Different Types in the Coastal Zone of the Baltic Sea. *Natural Hazards and Earth System Sciences*, 10(9), pp. 2021–2029. doi:10.5194/nhess-10-2021-2010

Submitted 13.05.2022; accepted after review 23.06.2022;
revised 06.07.2022; published 26.09.2022

About the authors:

Alexander S. Zapevalov, Chief Research Associate, Marine Hydrophysical Institute of RAS (2 Kapitanskaya St., Sevastopol, 299011, Russian Federation), Dr.Sci. (Phys.-Math.), **Scopus Author ID: 7004433476, ResearcherID: 6784-7782**, *sevzepter@mail.ru*

Anton V. Garmashov, Senior Research Associate, Marine Hydrophysical Institute of RAS (2 Kapitanskaya St., Sevastopol, 299011, Russian Federation), Ph.D. (Geogr.), **Scopus Author ID: 54924806400, ResearcherID: P-4155-2017**, *ant.gar@mail.ru*

Contribution of the authors:

Alexander S. Zapevalov – problem statement, data processing and analysis, article text and graphic materials preparation

Anton V. Garmashov – data processing and analysis, analysis of literary sources

All the authors have read and approved the final manuscript.

DOI: 10.22449/2413-5577-2022-3-16-27

Characteristics of Short-Period Internal Waves in the Laptev Sea and Adjacent Regions of the Kara and East Siberian Seas Based on Satellite Radar Data during Summer-Autumn Period of 2019

A. V. Kuzmin, I. E. Kozlov *

Marine Hydrophysical Institute of RAS, Sevastopol, Russia
**e-mail: ik@mhi-ras.ru*

Abstract

This paper presents the results of short-period internal waves (SIWs) observations in the Laptev Sea and adjacent areas of the Kara and East Siberian Seas based on analysis of satellite synthetic aperture radar (SAR) Sentinel-1 A/B data between July and October 2019. Analysis of 639 SAR images allowed identifying 2081 surface manifestations (SM) of SIWs. Main regions of SIW observations were determined and their spatial characteristics mapped. More than 60 % of registered SIWs were identified in September, and the lowest number of manifestations (9 %) was registered in July. Maximum number of SIW observations was found near the Arctic Cape, over the large area of the continental slope and in the northeastern shelf of the Laptev Sea. It is shown that the total number of SIW identifications in 2019 was much higher than in 2011, and the principal regions of SIW observations expanded. Moreover, new regions of regular SIW generation were determined in the Shokalsky Strait, between the New Siberian Islands and over the deep sea regions. The most intensive generation area was determined north of the Kotelny Island, between 50 m and 200 m isobaths. In this region, the total number of SIW detections exceeded 15 cases. While a significant increase in the number of SIW detections is observed in 2019, the overall range of the values of SIW spatial characteristics in 2019 is almost the same as in 2011.

Keywords: short period internal waves, Laptev Sea, Kara Sea, East Siberian Sea, satellite radar images, tidal currents

Acknowledgement : the study was carried out under state assignment no. FNNN-2021-0010 of FSBSI FRC MHI.

For citation: Kuzmin, A.V. and Kozlov, I.E., 2022. Characteristics of Short-Period Internal Waves in the Laptev Sea and Adjacent Regions of the Kara and East Siberian Seas Based on Satellite Radar Data during Summer-Autumn Period of 2019. *Ecological Safety of Coastal and Shelf Zones of Sea*, (3), pp. 16–27. doi:10.22449/2413-5577-2022-3-16-27

Характеристики короткопериодных внутренних волн в море Лаптевых и прилегающих районах Карского и Восточно-Сибирского морей по данным спутниковых радиолокационных наблюдений в летне-осенний период 2019 года

А. В. Кузьмин, И. Е. Козлов *

Морской гидрофизический институт РАН, Севастополь, Россия
**e-mail: ik@mhi-ras.ru*

Аннотация
Представлены результаты наблюдения короткопериодных внутренних волн в море Лаптевых и прилегающих районах Карского и Восточно-Сибирского морей, полученные на основе анализа измерений спутниковых радиолокаторов с синтезированной апертурой *Sentinel*-1 *A*/*B* с июля по октябрь 2019 г. Анализ 639 радиолокационных изображений позволил идентифицировать 2081 случай поверхностных проявлений короткопериодных внутренних волн. Определены основные районы наблюдения короткопериодных внутренних волн и построены карты распределения их основных пространственных характеристик. Более 60 % случаев наблюдения короткопериодных внутренних волн пришлось на сентябрь, а наименьшее количество проявлений – на июль (9 %). В исследуемый летне-осенний период максимальное количество поверхностных проявлений короткопериодных внутренних волн зарегистрировано в районе м. Арктического, а также на обширной области континентального склона и северо-восточной части шельфа моря Лаптевых. Показано, что общее число случаев регистрации короткопериодных внутренних волн в 2019 г. на порядок выше, чем в 2011 г., а районы обнаружения короткопериодных внутренних волн существенно расширились. Кроме того, обнаружены новые районы регулярной генерации короткопериодных внутренних волн в прол. Шокальского, между Новосибирскими о-вами, а также в глубоководной части акватории. Наиболее интенсивный район генерации поверхностных проявлений короткопериодных внутренних волн располагался в области между изобатами 50 и 200 м, севернее о-ва Котельный. На данном участке акватории максимальное суммарное количество поверхностных проявлений короткопериодных внутренних волн превышало 15. Отмечается, что при значительном увеличении общего количества наблюдений короткопериодных внутренних волн в 2019 г. диапазон изменчивости значений их основных пространственных характеристик в 2019 г. примерно такой же, как и в 2011 г.

Ключевые слова: короткопериодные внутренние волны, море Лаптевых, Карское море, Восточно-Сибирское море, спутниковые радиолокационные изображения, приливные течения

Благодарности: исследование выполнено в рамках государственного задания ФГБУН ФИЦ МГИ по теме № FNNN-2021-0010.

Для цитирования: *Кузьмин А. В., Козлов И. Е.* Характеристики короткопериодных внутренних волн в море Лаптевых и прилегающих районах Карского и Восточно-Сибирского морей по данным спутниковых радиолокационных наблюдений в летне-осенний период 2019 года // Экологическая безопасность прибрежной и шельфовой зон моря. 2022. № 3. С. 16–27. doi:10.22449/2413-5577-2022-3-16-27

Introduction

The Laptev Sea is a marginal water body of the Arctic Ocean (AO), characterized by active generation of sea ice and formation of polynyas [1]. The hydrological regime of the water area is characterized by intense river runoff.

Short-period internal waves (SIWs) are an important element of the dynamic structure of the ocean, which largely determines horizontal and vertical transfer of matter, momentum, and energy. Due to the increase in the rate of development of the shelf of the Arctic seas, the issue of studying the mechanisms and areas of SIW generation, the features of their distribution and the impact on the hydrological regime of the Arctic Basin is becoming more acute [2]. An important influence on the formation of SIWs is exerted by tidal currents and their interaction with inhomogeneities of benthic topography in the shelf zone and in areas of submarine slopes [3–5].

It is known that, according to satellite observation data, it is possible to determine the main areas of generation and propagation of surface manifestations (SM) of SIWs [3, 6]. In general, there are not so many works on the study of SIWs in the Laptev Sea based on satellite data. Previous work in this area using satellite data for 2007 and 2011 showed that SIW packets are regularly observed in the water area [7, 8]. In the same works, it was noted that the detected internal waves, apparently, were mainly of a tidal nature of formation and spread in certain areas of the shelf and continental slope.

This paper analyzes a vast array of Sentinel-1 A/B satellite radar data (RD) for the summer-autumn period of 2019 and presents the results of a study of the characteristics of the SIW field in the Laptev Sea and partially adjacent water areas of the Kara and East Siberian Seas. In the course of the work, the main areas of SIW generation and propagation in the water area were identified, their main spatial characteristics for the indicated period were determined and mapped.

Data and methods

The study of the spatial distribution of SIWs and their characteristics in the waters of the Laptev Sea was carried out based on the analysis of data from Sentinel-1 A/B satellite synthetic aperture radars (SAR), launched in 2014–2016. Regular SAR imaging makes it possible to obtain data with a high frequency (every 1–2 days) in a wide swath (about 250 km) and a spatial resolution of 40–90 m.

Processing of satellite data and identification of internal wave surface manifestations in radar images (RI) were carried out in accordance with the technique described in [6].

Fig. 1 shows a map of the study area covered by the SAR survey. As can be seen, the coverage of the radar imagery is quite uneven: most of the images are in the western part of the water area (west of the Arctic Cape), the central deep-water part, and the region near the New Siberian Islands. The least data-rich areas are in the Vilkitsky Strait and the coastal part of the Laptev Sea, as well as near the Anabar Bay, Khatanga Gulf, Olenyok Gulf and Yana Bay.

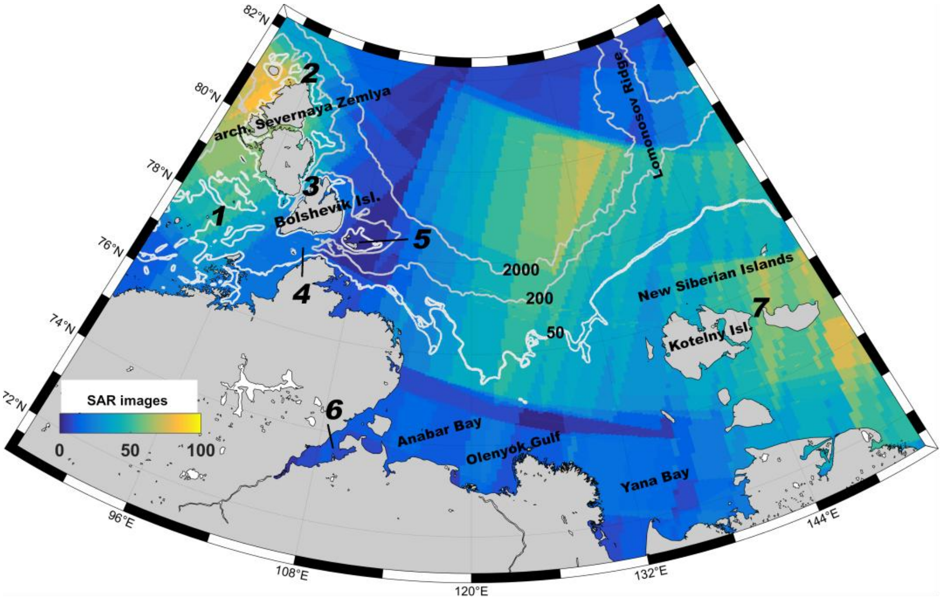

Fig. 1. Coverage of the Laptev Sea by Sentinel-1 SAR data from 1 July to 31 October 2019. White lines indicate 50-m, 200-m, and 2000-m isobaths. Numbered positions: *1* – Sergey Kirov Islands, *2* – Arctic Cape, *3* – Shokalsky Strait, *4* – Vilkitsky Strait, *5* – Maly Taymyr Island, *6* – Khatanga Gulf, *7* – Blagoveshensky Strait

Analysis of the spatial distribution of surface manifestations of SIWs was carried out using the SNAP program (Sentinel Application Platform). Fig. 2 shows an enlarged fragment of the Sentinel-1 RI for 09.19.2019 (22:50 UTC), which clearly shows manifestations of two SIW packets directed to the southeast.

Satellite observation results

In total, during the study, 639 Sentinel-1 A/B radar images were processed for the period from July 1 to October 31, 2019. A detailed study of the received radar images made it possible to detect 30 images with SIW surface manifestations. The largest part of SIW surface manifestations occurred in September (1318 SIW surface manifestations, ~60 %), and the smallest part occurred in July (239 SIW surface manifestations, ~9 %). Variations in the number of identified SIW manifestations for different months can be associated both with the intraseasonal variability of vertical stratification, which determines intensity of SIW generation, and with the variability of wind and ice conditions, which determine the possibility of identifying SIW surface manifestations in satellite data. The table shows the statistics of the analyzed data from July to October 2019.

As a result of processing of 639 radar images, 2081 SIW surface manifestations were found for the summer-autumn period of 2019. The spatial distribution of the leading waves in SIW packets is shown in Fig. 3, *a*. The SIW propagation was observed mainly in the form of solitary wave packets with consistent analysis

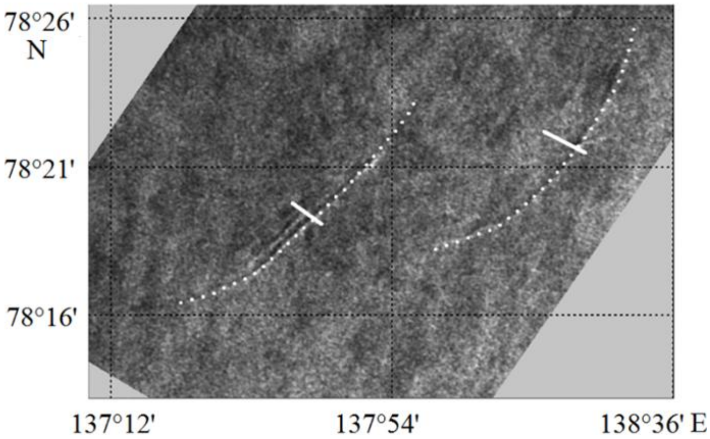

Fig. 2. An example of manifestation of SIWs in Sentinel-1 SAR image acquired on 09.10.2019 (22:50 UTC) in the Laptev Sea. White dotted lines indicate positions of leading waves in the SIW packets, the white solid line shows wave lengths of the relevant packets

Statistics of analyzed Sentinel-1 A/B SAR data and the number of the SIW SM from July to October 2019

Month	Number of		
	analyzed images	images with SIWs	registered SIW packets
July	164	4	191
August	147	7	422
September	175	16	1318
October	153	3	150
Total	**639**	**30**	**2081**

results; the SIW packets were directed both along the isobaths, towards increasing depths, and towards the shallow shelf. Fig. 3, *a* shows that the distribution of SIW packets over the sea area is uneven.

According to the data analysis of 2011 [7, 8], manifestations of internal waves were most often observed in four key areas: northwest of the Severnaya Zemlya archipelago, east of Bolshevik Island, near the mouths of the Anabar, Lena, and Khatanga rivers, and also north of the New Siberian Islands.

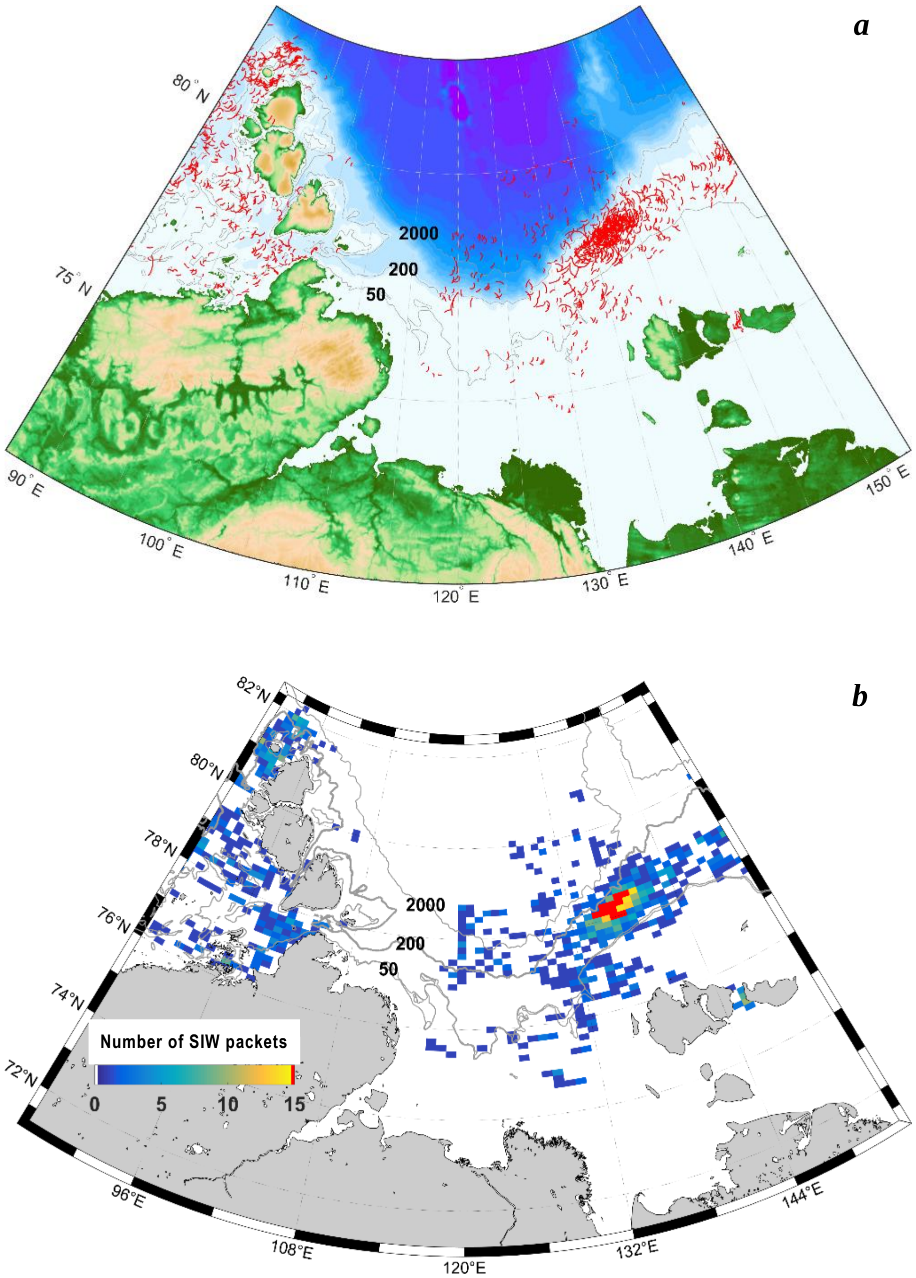

F i g . 3 . Distribution maps of the SIW packets in the Laptev Sea and adjacent regions from July to October 2019: *a* – locations of the leading wave crests in the SIW packets; *b* – total number of SIW surface manifestation. Grey lines indicate 50-m, 200-m, and 2000-m isobaths

A very similar distribution of SIW SMs was also observed in 2019, with the exception of coastal areas with a pronounced runoff of rivers and to the east of Maly Taymyr Island. This can be partly explained by the fact that the availability of radar images of these areas in 2019 was significantly lower. From July to October 2019, the maximum number of SIW SMs was registered in a vast area of the northeastern shelf of the Laptev Sea. In contrast to the results of 2011, a large number of SIW manifestations is also observed above the continental slope and near the edge of the shelf in the central part of the sea. Also, for the first time, SIW manifestations are observed in large numbers in the deep-water part of the water area southwest of the Lomonosov Ridge. In the western part of the water area, a large number of SIWs were found northwest of the Arctic Cape, as well as west of the islands of the Severnaya Zemlya archipelago. New areas of observation of SIWs were discovered to the northwest of Kotelny Island, in the Blagoveshensky Strait and between Kirov Island and the Nizkiy Cape, including the Vilkitsky Strait from the Kara Sea.

Fig. 3, *b* shows a distribution map of the total number of observed SIW SMs in the waters of the Laptev Sea at the nodes of a grid of 100 × 60 cells. In the most part of the study area, the total number of SIW SMs, on average, did not exceed five cases of registration over the entire observation period. However, in the Blagoveshensky Strait and north-west of the Arctic Cape, the number of SIW recording cases reached ten. The most intense area of SIW SM generation is the area between 50 and 200 m isobaths to the north of Kotelny Island. Here, the total number of SIW SMs in some areas exceeds 15 cases, and on average is at the level of 10–15 cases. This area is characterized by average data availability, while SIW SMs are recorded quite often in it. This confirms that this area is a key place for generation of internal waves in the Laptev Sea. Let us note that this area is characterized by the maximum velocities of tidal currents for the study area, reaching 1 m/s [4, 9].

Comparison of the obtained results with the results of the work of previous years allows us to conclude that the areas of SIW generation can change from year to year. For example, in 2019, the minimum number of SIW SMs was observed in sectors located east of Maly Taymyr Island and north of Bolshevik Island, where, according to 2011 data, it was maximum [7]. On the other hand, the areas north of the New Siberian Islands, in the Vilkitsky Strait and north-west of the Arctic Cape are fairly stable areas for internal wave generation. These areas have expanded significantly in recent years, which may be caused by the so-called atlantification of this sector of the Arctic [10–13]. We also note that the background ice conditions were somewhat different in 2019 and 2011: for the period under consideration, the average position of the ice edge in 2019 was more to the north than in 2011. This fact could affect both formation of more favorable conditions for the generation of SIWs due to the melting of a larger amount of ice, and ability to observe large areas of open water in the northern part of the study area.

Fig. 4 shows maps of distribution of some spatial SIW characteristics – the crest length SIWs (Fig. 4, *a*) and the length of the SIW packets (Fig. 4, *b*).

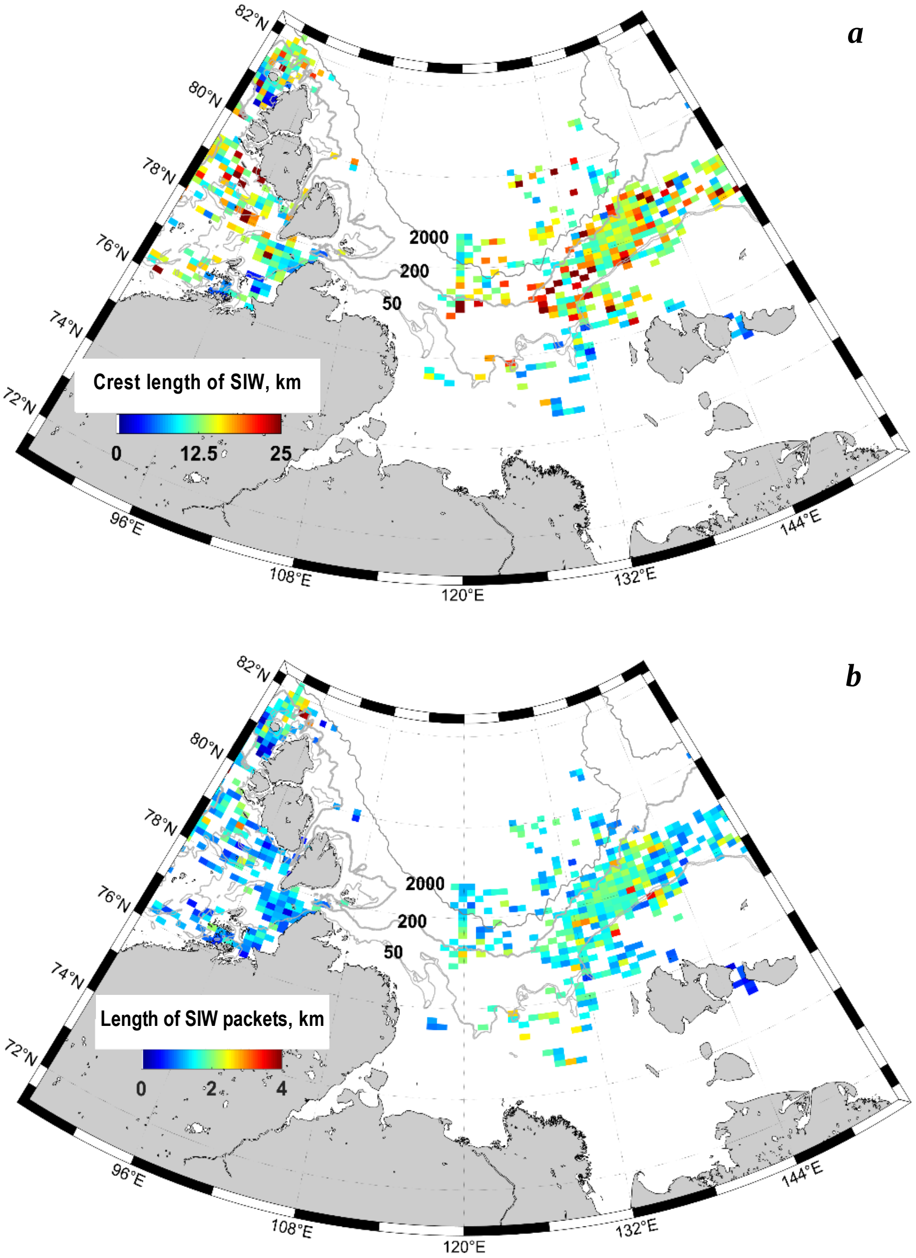

Fig. 4. Spatial distribution maps of the SIW characteristics in the Laptev Sea and adjacent regions from July to October 2019: *a* – crest length of the SIW packets; *b* – length of SIW packets. Grey lines indicate 50-m, 200-m, and 2000-m isobaths

Fig. 4, *a* shows that generation of SIW packets with longer crest lengths is noted along the entire shelf of the Laptev Sea. The most extended crests were found in the central part of the water area and northwest of Kotelny Island. In these areas, the crest length reaches maximum values (50–60 km). In the Vilkitsky, Shokalsky, and Blagoveshensky Straits, shorter SIW trains were observed, the value of the crest lengths did not exceed 12 km.

The distribution of SIW packet length values is shown in Fig. 3, *b*. SIW packets with maximum packet lengths up to 3.3 km were found north of Kotelny Island. In the region of the straits, the packet length varies from 0.9 km to 2.1 km. In the area north of the New Siberian Islands, more extended SIW packets are formed. A similar trend is also observed to the north of the Arctic Cape, where the values of the length of SIW SM packets are somewhat smaller. The zone in the Kara Sea basin is noteworthy: there are SIWs with more extended crest lengths, but with smaller packet widths. In the section from the Sergey Kirov Islands to Maly Taymyr Island and along the entire length of the Vilkitsky Strait the generation of SIWs with crest lengths of smaller ranges (7–10 km) at the same packet length is observed. This can probably be explained by the influence of background non-tidal currents, which can affect the spatial characteristics of internal waves depending on the current direction [14, 15].

Distribution of the average values of the crest length and the length of SIW packets is shown in the histograms in Fig. 5. The crest lengths characteristic of the Laptev Sea vary from 2 to 60 km, with an average value of 15.8 km.

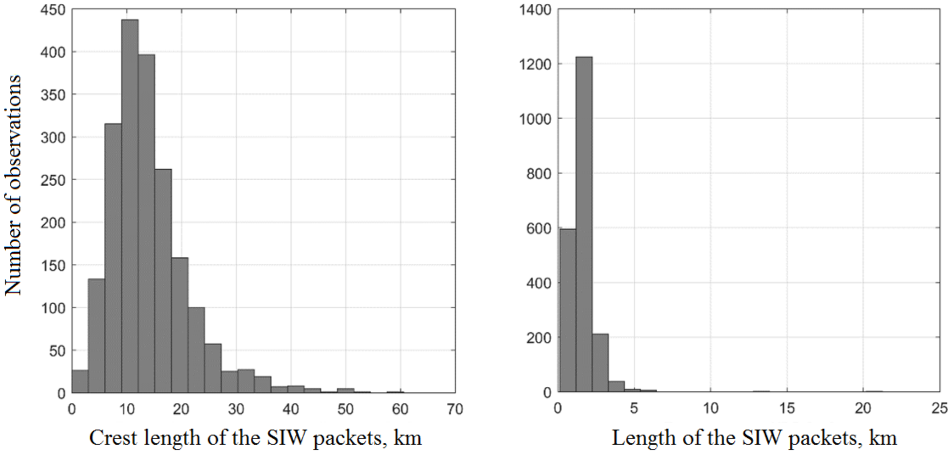

Fig. 5. Histograms of the SIW characteristics in the Laptev Sea and adjacent regions from July to October 2019: *a* – crest length of the SIW packets; *b* – length of the SIW packets

Most often, waves with a length of more than 20 km are observed in the central and eastern parts of the water area. The range of variations in the length of SIW packets is from 400 m to 5.2 km, with an average value of 1.85 km over the entire water area (Fig. 5, *b*).

Conclusion

The paper presents the results of a study of the field of short-period internal waves in the Laptev Sea, as well as the adjacent waters of the Kara and East Siberian Seas, obtained during the analysis of the Sentinel-1 A/B satellite data array for the summer-autumn period of 2019. In the course of 639 radar images processing, 30 images with pronounced internal wave surface manifestations were identified. A total of 2081 SIW SMs were registered, maps with the internal wave location and their spatial characteristics were constructed.

In the course of work, it was found that in 2019 the total number of SIW cases was significantly higher compared to 2011. The number of used satellite radar images for the summer-autumn period of 2019 was twice higher than their number in 2011, while the total number of SIW SM cases in 2019 was approximately 20 times higher than their number in 2011. It is interesting to note that with a significant increase in the total number of SIW observations in 2019, the variability range of the values of their main spatial characteristics is approximately the same as in 2011.

It is important that, in addition to the general increase in the cases of SIWs by an order of magnitude, the areas of SIW manifestation also expanded significantly. Besides, new regions of regular SIW generation were discovered in the Shokalsky Strait, between the New Siberian Islands, as well as in the deep-water part of the water area. All these facts indirectly confirm the hypothesis that the observed "atlantication" of the Eurasian sector of the Arctic, which is characterized, among other things, by intensification of currents against the background of a general weakening of vertical stratification, can contribute to an increase in the SIW generation in the Arctic.

REFERENCES

1. Morozov, E.G. and Pisarev, S.V., 2004. Internal Waves and Polynya Formation in the Laptev Sea. *Doklady Earth Sciences*, 398(7), pp. 983–986.
2. Talipova, T.G., Polukhin, N.V., Kurkin, A.A. and Lavrenov, I.V., 2003. [Modelling of Internal Wave Soliton Transformation in the Laptev Sea Shelf]. *News Academy of Engineering Sciences A.M. Prokhorov*, (4), pp. 3–16 (in Russian).
3. Zimin, A.V., Kozlov, I.E., Atadzhanova, O.A. and Chapron, B., 2016. Monitoring Short-Period Internal Waves in the White Sea. *Izvestiya, Atmospheric and Oceanic Physics*, 52(9), pp. 951–960. doi:10.1134/S0001433816090309
4. Fer, I., Koenig, Z., Kozlov, I.E., Ostrowski, M., Rippeth, T.P., Padman, L., Bosse, A. and Kolas, E., 2020. Tidally Forced Lee Waves Drive Turbulent Mixing along the Arctic Ocean Margins. *Geophysical Research Letters*, 47(16), e2020GL088083. doi:10.1029/2020GL088083
5. Marchenko, A.V., Morozov, E.G., Kozlov, I.E. and Frey, D.I., 2021. High-Amplitude Internal Waves Southeast of Spitsbergen. *Continental Shelf Research*, 227, 104523. doi:10.1016/j.csr.2021.104523

6. Kozlov, I.E., Kudryavtsev, V.N., Zubkova, E.V., Zimin, A.V. and Chapron, B., 2015. Characteristics of Short-Period Internal Waves in the Kara Sea Inferred from Satellite SAR Data. *Izvestiya, Atmospheric and Oceanic Physics*, 51(9), pp. 1073–1087. doi:10.1134/S0001433815090121
7. Zubkova, E.V., Kozlov, I.E. and Kudryavtsev, V.N., 2016. Spaceborne SAR Observations of Short-Period Internal Waves in the Laptev Sea. *Sovremennye Problemy Distantsionnogo Zondirovaniya Zemli iz Kosmosa*, 13(6), pp. 99–109. doi:10.21046/2070-7401-2016-13-6-99-109 (in Russian).
8. Kozlov, I.E., Zubkova, E.V. and Kudryavtsev, V.N., 2017. Internal Solitary Waves in the Laptev Sea: First Results of Spaceborne SAR Observations. *IEEE Geoscience and Remote Sensing Letters*, 14(11), pp. 2047–2051. doi:10.1109/LGRS.2017.2749681
9. Kagan, B.A. and Timofeev, A.A., 2020. High-Resolution Modeling of Semidiurnal Internal Tidal Waves in the Laptev Sea in the Ice-Free Period: Their Dynamics and Energetics. *Izvestiya, Atmospheric and Oceanic Physics*, 56(5), pp. 512–521. doi:10.1134/S0001433820050047
10. Polyakov, I.V., Pnyushkov, A.V., Alkire, M.B., Ashik, I.M., Bauman, T.M., Carmack, E.C., Goszczko, I., Guthrie, J., Ivanov, V.V. [et al.], 2017. Greater Role for Atlantic Inflows on Sea-Ice Loss in the Eurasian Basin of the Artic Ocean. *Science*, 356(6335), pp. 285–291. doi:10.1126/science.aai8204
11. Morozov, E.G., Kozlov, I.E., Shchuka, S.A. and Frey, D.I., 2017. Internal Tide in the Kara Gates Strait. *Oceanology*, 57(1), pp. 8–18. doi:10.1134/S0001437017010106
12. Kagan, B.A. and Timofeev, A.A., 2020. Dynamics and Energetics of Tides in the Laptev Sea: the Results of High-Resolving Modeling of the Surface Semidiurnal Tide M_2. *Fundamentalnaya i Prikladnaya Gidrofizika*, 13(1), pp. 15–23. doi:10.7868/S2073667320010025 (in Russian).
13. Polyakov, I.V., Rippeth, T.P., Fer, I., Baumann, T.M., Carmack, E.C., Ivanov, V.V., Janout, M., Padman, L., Pnyushkov, A.V. and Rember, R., 2020. Intensification of Near-Surface Currents and Shear in the Eastern Arctic Ocean. *Geophysical Research Letters*, 47(16), e2020GL089469. doi:10.1029/2020GL089469
14. Rippeth, T.P., Vlasenko, V., Stashchuk, N., Scannell, B.D., Green, J.A.M., Lincoln, B.J. and Bacon, S., 2017. Tidal Conversion and Mixing Poleward of the Critical Latitude (an Arctic Case Study). *Geophysical Research Letters*, 44(24), pp. 12349–12357. doi:10.1002/2017GL075310
15. Kagan, B.A. and Sofina, E.V., 2022. Effect of Diapycnal Mixing on Climatic Characteristics of the Laptev Sea in the Ice-Free Period. *Physical Oceanography*, 29(2), pp. 204–219. doi:10.22449/1573-160X-2022-2-204-219

Submitted 5.04.2022; accepted after review 7.05.2022;
revised 6.07.2022; published 26.09.2022

About the authors:

Alexey V. Kuzmin, Junior Research Associate, Marine Hydrophysical Institute of RAS (2 Kapitanskaya St., Sevastopol, 299011, Russian Federation)

Igor E. Kozlov, Leading Research Associate, Marine Hydrophysical Institute of RAS (2 Kapitanskaya St., Sevastopol, 299011, Russian Federation), **ORCID ID: 0000-0001-6378-8956, ResearcherID: G-1103-2014**, *ik@mhi-ras.ru*

Contribution of the authors:

Alexey V. Kuzmin – data processing and analysis, article text preparation and revision

Igor E. Kozlov – problem statement, data processing and analysis, preparation of visual materials, article text revision

All the authors have read and approved the final manuscript.

DOI: 10.22449/2413-5577-2022-3-28-42

Features of River Plume Formation in a Shallow Lagoon (the Case of the Sivash Bay, the Sea of Azov)

V. V. Fomin, A. A. Polozok *

Marine Hydrophysical Institute of RAS, Sevastopol, Russia
**e-mail: polozok.umi@gmail.com*

Abstract

Features of the thermohaline structure of the waters of lagoons and bays have a significant impact on the biological diversity, productivity and quality of the waters of these areas. In this paper, the characteristics of a freshwater plume in the area of the Salgir River outlet into the Sivash Bay are studied. The study was performed on the basis of a three-dimensional hydrodynamic model POM with 10 m horizontal resolution and 0.1 m vertical one. Data from field observations of river runoff, temperature and salinity of river and sea water, which were carried out in the area of the mouth of the Salgir River in June 2021, were used as input parameters of the model. Based on a series of numerical experiments, the influence of various types of currents on the position, shape and size of the plume was studied. It is shown that under the influence of river runoff a plume several hundred meters in size is formed at the debouchment from the river mouth. Due to the rotation of the Earth, the shape of the plume is asymmetric. This asymmetry appears regardless of the presence of any currents in the basin. Alongshore currents cause a decrease in the transverse size of the plume by a factor of two. When the wind is directed towards the shore, the plume is blocked, and fresh water spreads in a narrow strip on both sides of the river mouth. The plume is concentrated in the upper layer 20–40 cm thick. The thickness of the plume shows the smallest value in the immediate vicinity of the river mouth due to the rise of fresh water coming from the bottom layers of the river to the surface of the basin.

Keywords: Sea of Azov, Crimea, Salgir, Sivash, fresh runoff, river plume, mathematical modeling

Acknowledgments: the study was carried out within the theme of the Marine Hydrophysical Institute of RAS no. 0555-2021-0005 “Coastal studies”. Model calculations were carried out on the MHI computing cluster.

For citation: Fomin, V.V. and Polozok, A.A., 2022. Features of River Plume Formation in a Shallow Lagoon (the Case of the Sivash Bay, the Sea of Azov). *Ecological Safety of the Coastal and Shelf Zones of the Sea*, (3), pp. 28–42. doi:10.22449/2413-5577-2022-3-28-42

Особенности формирования речного плюма в мелководной лагуне (на примере залива Сиваш, Азовское море)

В. В. Фомин, А. А. Полозок *

Морской гидрофизический институт РАН, Севастополь, Россия

e-mail: polozok.umi@gmail.com

Аннотация

Особенности термохалинной структуры вод лагун и заливов оказывают значительное влияние на биологическое разнообразие, продуктивность и качество вод этих акваторий. В работе исследуются характеристики пресноводного плюма в районе впадения реки Салгир в залив Сиваш. Исследование выполнено на основе трехмерной гидродинамической модели типа *POM* с разрешением 10 м по горизонтали и 0.1 м по вертикали. В качестве входных параметров модели использованы данные натурных наблюдений за речным стоком, температурой и соленостью речной и морской воды, выполненных в районе устья реки Салгир в июне 2021 г. На основе серии численных экспериментов изучено влияние различного типа течений на положение, форму и размеры плюма. Показано, что под воздействием речного стока на выходе из устья реки формируется плюм диаметром (горизонтальным размером) несколько сотен метров. Из-за вращения Земли форма плюма асимметричная. Эта асимметрия проявляется независимо от того, существуют ли в бассейне течения. Вдольбереговые течения вызывают уменьшение поперечного размера плюма в два раза. Когда ветер направлен в сторону берега, происходит запирание плюма и пресная вода растекается узкой полосой по обе стороны от устья реки. Плюм сосредоточен в верхнем слое толщиной 20–40 см. В непосредственной близости от устья реки толщина плюма наименьшая, что обусловлено подъемом к поверхности бассейна пресной воды, поступающей из придонных слоев реки.

Ключевые слова: Азовское море, Крым, Салгир, Сиваш, речной сток, речной плюм, математическое моделирование

Благодарности: исследование выполнялось в рамках темы Морского гидрофизического института РАН № 0555-2021-0005 «Прибрежные исследования». Модельные расчеты проводились на вычислительном кластере МГИ.

Для цитирования: *Фомин В. В., Полозок А. А.* Особенности формирования речного плюма в мелководной лагуне (на примере залива Сиваш, Азовское море) // Экологическая безопасность прибрежной и шельфовой зон моря. 2022. № 3. С. 28–42. doi:10.22449/2413-5577-2022-3-28-42

Introduction

The Sivash Bay is a shallow lagoon separated from the Sea of Azov by the Arabat Spit, a sandy spit elongated in the meridional direction (Fig. 1). Water exchange between the bay and the sea occurs through the Tonkiy Strait. Estimates of the components of the water and salt balance of the Sivash Bay, such as atmospheric precipitation, evaporation, and water exchange, were obtained in [1–5]. Nevertheless, the component of the water balance associated with surface fresh runoff, i.e., the inflow of water into the bay from the rivers of the Crimean Peninsula, especially during floods, has remained insufficiently studied. Among these rivers, the largest water artery is the Salgir, which provides about 70% of the fresh runoff into the Sivash Bay [1]. A plume can form in the area where the Salgir River flows into the Sivash Bay.

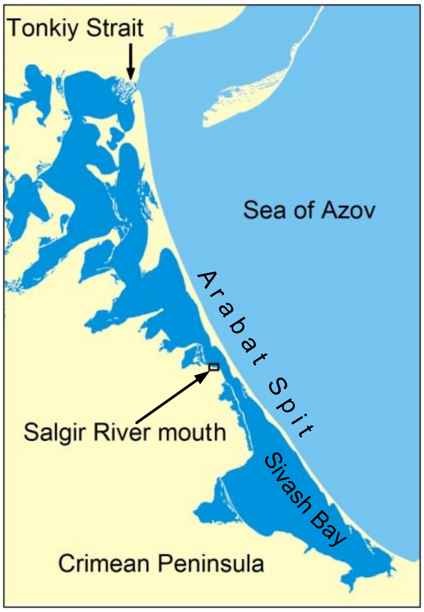

Fig. 1. Location of the Sivash Bay and the Salgir River mouth (selected rectangular area)

Plumes are a kind of lenses of freshened waters that are usually formed in the mouth areas of rivers [6–11]. As long as the inflow of fresh water is maintained, the plume exists permanently. However, currents of various origins, primarily wind currents, can influence its position, shape, and size.

The structure of the plume in the region of the Salgir mouth has almost not been studied. On June 24, 2021, the Sevastopol branch of the SOI conducted an areal survey of water temperature and salinity in the area of the Salgir mouth (the survey data were kindly provided by N. N. Dyakov). A plume was identified successfully in the salinity field (Fig. 2). The estimated horizontal extent of the plume along the isohaline of ~ 55 ‰ showed that it had a size of ~ 75–100 m. From the right side of the river mouth, the plume is somewhat elongated in the southeasterly direction, which indicates the presence of an alongshore flow here. The water temperature in the river and the bay was almost the same.

The results of this survey gave reasons for this work, the purpose of which was to study the general characteristics of the plume in the region of the Salgir

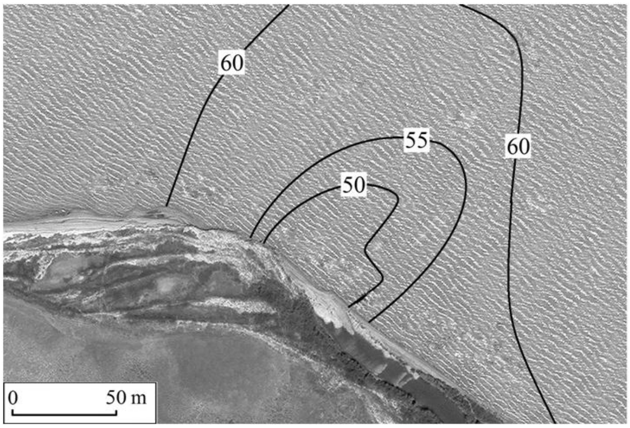

Fig. 2. Surface distribution of water salinity (‰) in the area of the mouth of the Salgir River according to measurements dated June 24, 2021

mouth based on mathematical modeling. It appears that the results of model calculations will help to approach the planning of further field studies of river plumes in the Sivash Bay and other regions more reasonably.

When modeling the plume, the following parameters were used:

$$Q_p = 0.81\ \text{m}^3/\text{s};\quad T_0 = 27.5\ °\text{C};\quad S_0 = 60\ ‰;\quad T_p = T_0;\quad S_p = 0,$$

where Q_p, T_0, S_0 – water discharge of the Salgir River, background distributions of water temperature and salinity in the Sivash Bay area of study; T_p, S_p – temperature and salinity of river water. The average velocity of the inflowing fresh water u_p was determined from the water discharge and the cross-sectional area of the river outlet. According to the given parameters, the water temperature in the river and in the bay are the same. Therefore, the formation of the plume is due to the difference in salinity between the inflowing fresh water and the bay water.

Mathematical model of plume

A shallow basin $L_x \times L_y$ in size bounded by free surface and flat bottom is considered (Fig. 3). The x-axis is east-facing and the y-axis is north-facing. The area has a solid lateral boundary: $y = 0$. Depending on the context of the tasks under consideration, the remaining three boundaries can be either open (liquid) or solid. At the initial moment of time ($t = 0$)

$$u = u_0,\ \ v = 0,\ \ w = 0,\ \ T = T_0,\ \ S = S_0,$$

where u, v, w – flow velocity components along the x, y, z axes, respectively; T, S – water temperature and salinity; u_0 – alongshore background current velocity.

When $t > 0$ at the point (x_p, y_p) a local source of mass begins to act, thus simulating the fresh runoff. The problem is set to study the evolution of fields T and S for given values of the parameters.

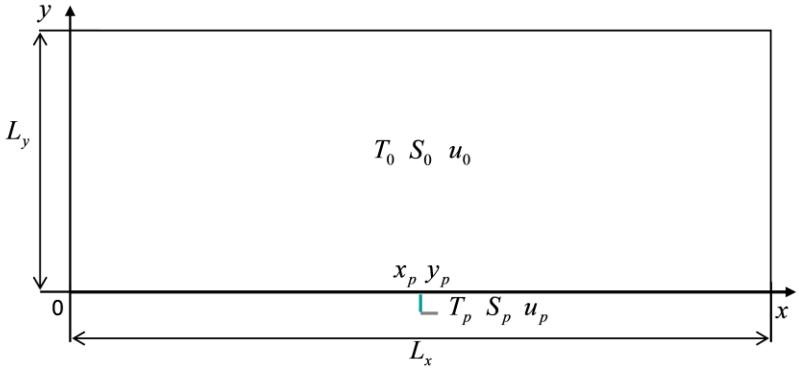

Fig. 3. Computational domain and input parameters of the model. A fragment of the riverbed is shown in gray

In this work, the numerical model [12, 13] is used. The model is based on three-dimensional σ-coordinate equations of ocean dynamics in the Boussinesq approximation and hydrostatics of the following form (terms of the equations with repeated indices α and β are summed from 1 to 2):

$$\frac{\partial}{\partial t}\left(Du_\alpha\right)+\Lambda u_\alpha+\varepsilon_{\alpha\beta} fDu_\beta+gD\frac{\partial\eta}{\partial x_\alpha}+DB_\alpha=\frac{\partial}{\partial x_\beta}\left(D\tau_{\alpha\beta}\right)+\frac{\partial}{\partial\sigma}\left(\frac{K_M}{D}\frac{\partial u_\alpha}{\partial\sigma}\right),$$

$$\frac{\partial\eta}{\partial t}+\frac{\partial}{\partial x_\alpha}\left(Du_\alpha\right)+\frac{\partial w_*}{\partial\sigma}=0,$$

$$\frac{\partial}{\partial t}\left(DT\right)+\Lambda T=\frac{\partial}{\partial x_\beta}\left(A_T\frac{\partial T}{\partial x_\beta}\right)+\frac{\partial}{\partial\sigma}\left(\frac{K_T}{D}\frac{\partial T}{\partial\sigma}\right),$$

$$\frac{\partial}{\partial t}\left(DS\right)+\Lambda S=\frac{\partial}{\partial x_\beta}\left(A_S\frac{\partial S}{\partial x_\beta}\right)+\frac{\partial}{\partial\sigma}\left(\frac{K_S}{D}\frac{\partial S}{\partial\sigma}\right),$$

$$\rho=\rho\left(T,S\right), \qquad (1)$$

$$\Lambda\varphi=\frac{\partial}{\partial x_\beta}\left(Du_\beta\varphi\right)+\frac{\partial}{\partial\sigma}\left(w_*\varphi\right),\qquad B_\alpha=\frac{g}{\rho_0}\left(\frac{\partial}{\partial x_\alpha}D\int_\sigma^0\rho d\sigma'+\sigma\frac{\partial D}{\partial x_\alpha}\rho\right),$$

$$\tau_{\alpha\alpha}=2A_M\frac{\partial u_\alpha}{\partial x_\alpha},\qquad \tau_{\alpha\beta}=\tau_{\beta\alpha}=A_M\left(\frac{\partial u_\beta}{\partial x_\alpha}+\frac{\partial u_\alpha}{\partial x_\beta}\right),$$

where $(x_1, x_2) = (x, y)$; σ – dimensionless vertical coordinate ranging from –1 to 0; $(u_1, u_2) = (u, v)$ – horizontal components of the current velocity; $D = h_0 + \eta$; h_0 – basin depth; η – free surface coordinate; w_* – normal to surfaces σ = const current velocity constant (at the constant value of h_0 value $w_* = w$); f – Coriolis parameter; $\varepsilon_{\alpha\beta}$ – Kronecker symbol; $\tau_{\alpha\beta}$ – turbulent stress tensor components; $A_M, K_M, A_T, K_T, A_S, K_S, K_C$ – turbulent viscosity and diffusion coefficients; g – acceleration of gravity; ρ – sea water density; ρ_0 – average density of water.

On the free surface (σ = 0), the boundary conditions are as follows:

$$w_*=0,\qquad \frac{K_M}{D}\frac{\partial u_\alpha}{\partial\sigma}=c_a|u|u_\alpha,\qquad \frac{K_T}{D}\frac{\partial T}{\partial\sigma}=0,\qquad \frac{K_S}{D}\frac{\partial S}{\partial\sigma}=0.$$

The boundary conditions at the bottom are written as follows:

$$w_*=0,\qquad \frac{K_M}{D}\frac{\partial u_\alpha}{\partial\sigma}=c_b|u|u_\alpha,\qquad \frac{K_T}{D}\frac{\partial T}{\partial\sigma}=0,\qquad \frac{K_S}{D}\frac{\partial S}{\partial\sigma}=0.$$

where c_a, c_b – friction coefficients; $|u|=\sqrt{u_1^2+u_2^2}$.

On solid meridional walls ($x_1 = 0$; $x_1 = L_x$), the following conditions are given:

$$u_1 = 0, \quad u_2 = 0, \quad \frac{\partial T}{\partial x_1} = 0, \quad \frac{\partial S}{\partial x_1} = 0.$$

On solid zonal walls ($x_2 = 0$; $x_2 = L_y$), the following conditions are given:

$$u_2 = 0, \quad u_1 = 0, \quad \frac{\partial T}{\partial x_2} = 0, \quad \frac{\partial S}{\partial x_2} = 0. \qquad (2)$$

The setting of boundary conditions in liquid areas is discussed below.

The coefficient of horizontal turbulent viscosity A_M was calculated using the Smagorinskiy formula [14]. The coefficients of horizontal turbulent diffusion of heat, salts were taken equal to 0.5 A_M. The equation of state of sea water (1) was given by the *UNESCO* formula, which is widely used in the sea water dynamics modeling. It should be noted that the Sivash Bay is a hypersaline reservoir. The choice of the equation of state for such reservoirs is a separate problem that is beyond the scope of this work. Note that this problem has not yet been solved for the Sivash Bay.

In problems with background current u_0, vertical exchange coefficients were constant: $K_M = \overline{K}_M$; $K_S = K_T = \overline{K}_S$, where $\overline{K}_M = 2 \cdot 10^{-5}$ m^2/s; $\overline{K}_S = 10^{-6}$ m^2/s. In problems with wind current, K_M and K_S were determined on the basis of the Mellor-Yamada theory [15].

The numerical algorithm of the model is based on the division of the problem into barotropic and baroclinic modes and the use of explicit schemes for horizontal coordinates and implicit schemes for the σ-coordinate. Advective operator Λ in the model equations is approximated by *TVD*-schemes [16], which ensure the monotonicity of the numerical solution, which is necessary for the correct description of fields with large spatial gradients.

In numerical experiments, the computational domain had the following dimensions (Fig. 3): L_x = 4,000 m; L_y = 1,500 m; h_0 = 1.5 m. The river bed coordinates are as follows: x_p = 2,000 m, y_p = 50 m. Horizontally, a rectangular computational grid was used with step Δx = 10 m. On the vertical coordinate, the number of calculated levels makes n = 16. This value of n was chosen on the basis of preliminary calculations for a satisfactory resolution of the vertical structure of the plume concentrated in the upper half-meter layer.

To take into account the source of fresh water in the model, the computational domain was supplemented with an *L*-shaped fragment of the riverbed (see Fig. 3), consisting of four cells vertically and horizontally. When $t = 0$ in this section of the riverbed, $S = S_0$. The values of parameters T_p, S_p and u_p were set in the rightmost cell. The average velocity of river water inflow into the bay makes $u_p = Q_p / (\Delta x\, h_p) = 0.16$ m/s, where h_p = 0.5 m – river bed depth. Thus, due to the source movement upstream in the riverbed, partial mixture of fresh and salt water takes place. This reduces the horizontal salinity gradients in the river outlet and, thus, reduces the likelihood of hydrodynamic instability here. Similar methods of specifying a source of fresh water were used in [6, 10, 16] when modeling river plumes.

When $u_0 = 0$ on the liquid boundaries of the computational domain, the condition of smooth continuation was set, assuming the equality to zero of the normal derivative of the desired prognostic variable. As practice shows, on small intervals of integration over time, such a set of conditions on open boundaries works quite satisfactorily.

Calculation results and discussion

The configuration of the numerical model proposed above made it possible to study the initial phase of the formation of freshwater plume in the area of the mouth of the Salgir River. The integration was carried out for a period of 6–8 h with step $\Delta t = 4$ s. In all calculations for the first hour of the model time, the water flow in the source increased linearly from 0 to Q_p and then remained unchanged.

The main object of analysis was the relative salinity of water

$$C = (1 - S/S_0)\cdot 100\ \%. \qquad (3)$$

This value characterizes the degree of dilution of the salty water of the bay with river water, i.e. C shows by what percent S at a particular point in the bay is less than S_0. From formula (3) it follows that $C = 0$ when $S = S_0$ and $C = 100\ \%$ when $S = 0$. The plume boundaries were determined from the position of the isoline $C = 10\ \%$, which approximately corresponds to the isohaline 55 ‰ in the field experiment (Fig. 2).

1. *Influence of the Coriolis force*. When $u_0 = 0$, two numeric fields C were performed on the upper horizon, which is shown in Fig. 4. Here, the experiment is performed with and without consideration to the Coriolis force ($f > 0$ and $f = 0$). Corresponding isolines C in other figures are given with step 5 %. The first isoline corresponds to $C = 5\ \%$ (57 ‰). As is obvious, under the influence of river runoff, the plume is formed at the exit from the river mouth in the form of the low salinity

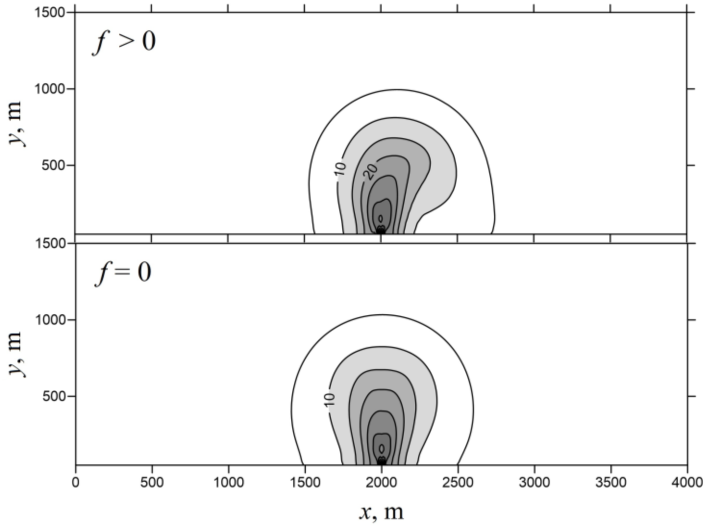

Fig. 4. Field $C(x, y, 0, t)$ at $t = 8$ h with ($f > 0$) and without ($f = 0$) the Coriolis force

area extended towards the bay. Over time, the plume spreads in all directions and increases in size. When $f > 0$, the plume tends to shift to the right side of the source. When $f = 0$, the shape of the plume is symmetrical with respect to the position of the source (straight $x = x_p$).

Note that the effect of the Earth's rotation on plumes is known in the literature [6, 10, 11, 16]. When leaving the mouth, the fresh flow turns to the right under the influence of the Coriolis force in the Northern Hemisphere ($f > 0$). In our case, it is noteworthy that even for such a small plume, the influence of the Coriolis force is noticeable. This effect acts constantly and in its pure form can be clearly observed in low wind weather.

2. *Influence of the alongshore current*. Let us consider the effect of the direction and velocity of the alongshore current u_0 on the position, shape and size of the plume. To simplify the problem, we assume that the alongshore current is constant in depth and does not change in time. In this case, the nature of the flow is not fundamental. Considering the direction of the effect of the Coriolis force on the plume, the alongshore current at $u_0 > 0$ will be referred to as the associated current (directed to the right from the mouth), and the alongshore current at $u_0 < 0$ – counter current (directed to the left from the mouth).

The left side of Fig. 5 shows the salinity fields on the basin surface for three values of the associated current velocity: $u_0 = a_1$; $u_0 = a_2$; $u_0 = a_3$, where constants a_i

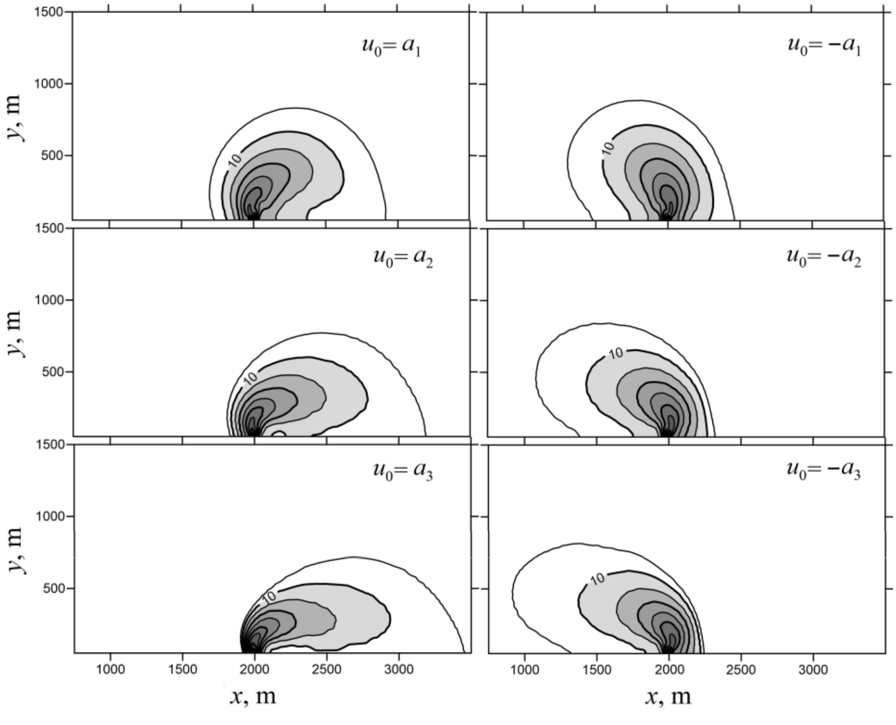

F i g . 5 . Field $C(x, y, 0, t)$ at $t = 6$ h for different velocities u_0 of the associated (left) and counter (right) current depend on the average flow velocity in the river station u_p: $a_1 = u_p/6$, $a_2 = u_p/3$ and $a_3 = u_p/2$. As can be seen, the associated flow causes plume deformations, which are expressed in its compression in the transverse direction and extension in the longitudinal direction. In this case, the plume moves downstream. All these deformations are clearly traced by the configuration of isolines $C \geq 10$ %.

The results of calculations of the field C for different values of the velocities of the counter current are shown in Fig. 5, right. Concerning the counter current, the behavior of the plume is somewhat different. The plume also shifts in the direction of the current (to the left), but its pressing against the shore is less noticeable compared to the case of the associated current. Thus, the influence of the Coriolis force on the characteristics of the plume in the case of alongshore currents manifests itself in different ways: in the case of the associated current, the plume is more pressed to the shore and more elongated in the direction of the flow.

The vertical structure of the field C in the cross section $x = x_p$ for three values of u_0 is shown in Fig. 6. The plume is concentrated in a very thin surface layer 15–20 cm thick. Consideration of the background current leads to a decrease in the extent of the plume along the y-coordinate and its pressing against the shore, which is most noticeable in the case of the associated current ($u_0 = a_3$).

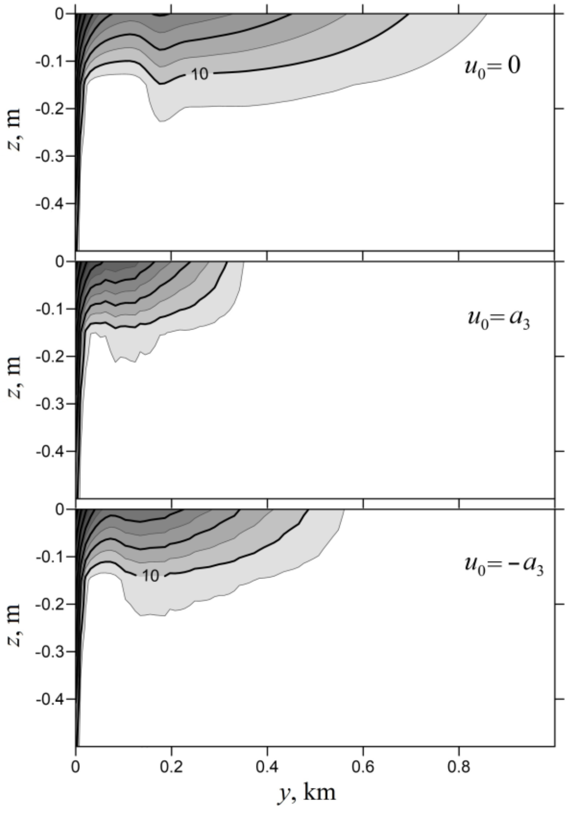

Fig. 6. Field $C(x_p, y, z, t)$ at $t = 6$ h for different values of u_0

Attention is drawn to the decrease in the thickness of the plume in the area immediately adjacent to the river mouth, which is due to the effect of buoyancy – the rise (emergence) of fresh water entering the basin from the bottom layers of the river to the surface of the basin.

3. *Influence of wind currents*. It is of interest to consider the influence of wind currents of different directions on the plume configuration. To simplify the calculations, the basin is considered to be closed. The vertical exchange coefficients were determined according to the Mellor-Yamada model, and the constants $\overline{K}_M$ and $\overline{K}_S$ were used as their minimum values. In the process of integration, the wind speed was multiplied by a coefficient, which linearly increased from 0 to 1 for the first hour of model time and then remained unchanged.

Fig. 7 shows the distribution of C on the surface of the model basin for four wind directions at t = 8 h. The wind velocity makes W = 7.5 m/s. It can be seen that for the alongshore wind direction the plume configuration qualitatively coincides with the calculation options for the alongshore background current. In particular, the asymmetry of the plume shape is manifested, which is associated with the influence of the Coriolis force. With wind from the shore, the plume extends in the form of an oval into the bay. When the wind is directed towards the shore, the plume is blocked and fresh water spreads in a narrow strip on both sides of the river mouth.

Fig. 8 shows the vertical section of the field C when $x = x_p$ for the wind directions shown in Fig. 7. The largest plume thickness corresponds to the wind directed towards the shore (θ = 0°). In this case, the lower boundary of the plume C = 10 % reaches the depth of 0.4 m. When the wind is directed away from the shore (θ = 270°), the plume becomes significantly eroded and its boundary recedes from the coast by 1.2 km.

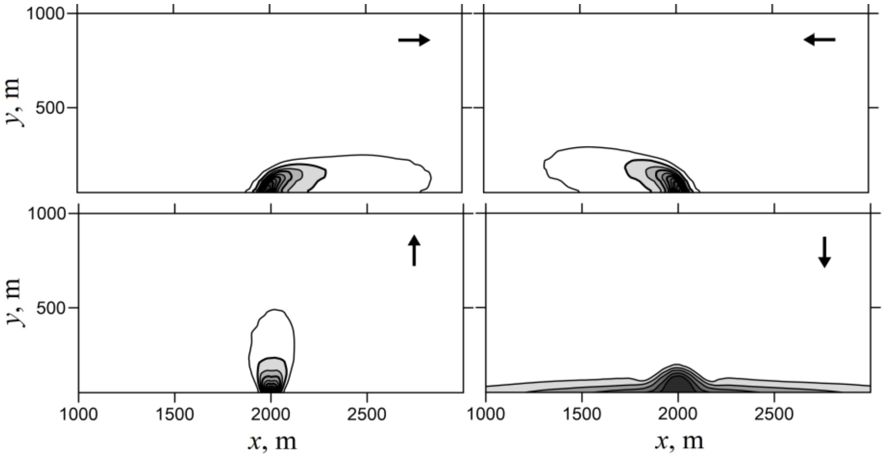

F i g . 7 . Field $C(x, y, 0, t)$ at t = 8 h for four wind directions at W = 7.5 m/s. The arrows show the direction of the wind

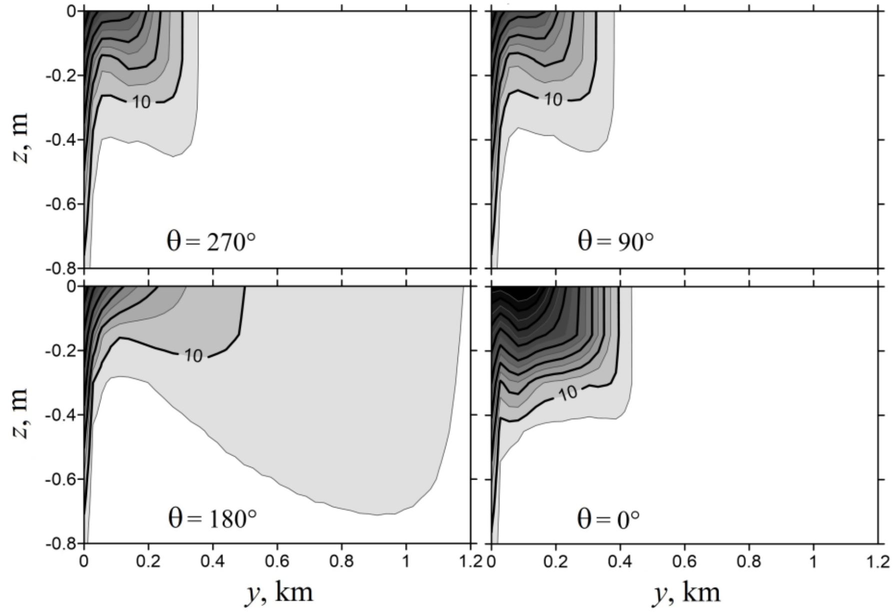

Fig. 8. Field $C(x_p, y, z, t)$ at t = 8 h for different wind directions θ at W = 7.5 m/s (270° – West; 90° – East; 180° – South; 0° – North)

In the final numerical experiment, an unsteady wind of the following type was specified

$$W_x = W_0 \cos \omega t, \quad W_y = W_0 \sin \omega t, \qquad (4)$$

where W_0 = 7.5 m/s; $\omega = 2\pi/T_w$; T_w = 8 h. The purpose of the experiment is to show how the plume reacts to a change in wind direction.

The results of calculation of the salinity field on the basin surface with an interval of 2 h are given in Fig. 9. According to formulas (4), for the period of time T_w, the wind speed vector makes a full turn counterclockwise.

Constant change in wind direction leads to constant change in the configuration of the plume. When $0 < t < 4$ h, the wind is directed from the shore towards the bay and the plume is localized near the river mouth. When $t > 4$ h, the wind is directed towards the shore. In this case, alongshore currents arise, which stretch and move the plume along the coast in the western and then eastern directions.

Fig. 10 shows the vertical sections of the field C when $x = x_p$ for the moments of time shown in Fig. 9. As can be seen, the horizontal extent of the plume is approximately the same (200–300 m). When the wind is directed toward the shore, the lower boundary of the plume deepens by 15–20 cm.

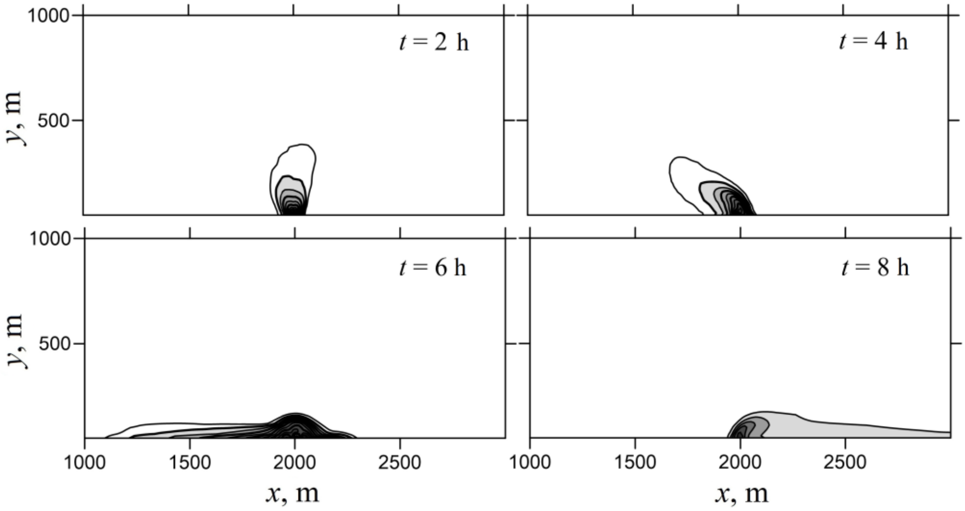

Fig. 9. Field $C(x, y, 0, t)$ with unsteady wind of the form (2) for four time stations

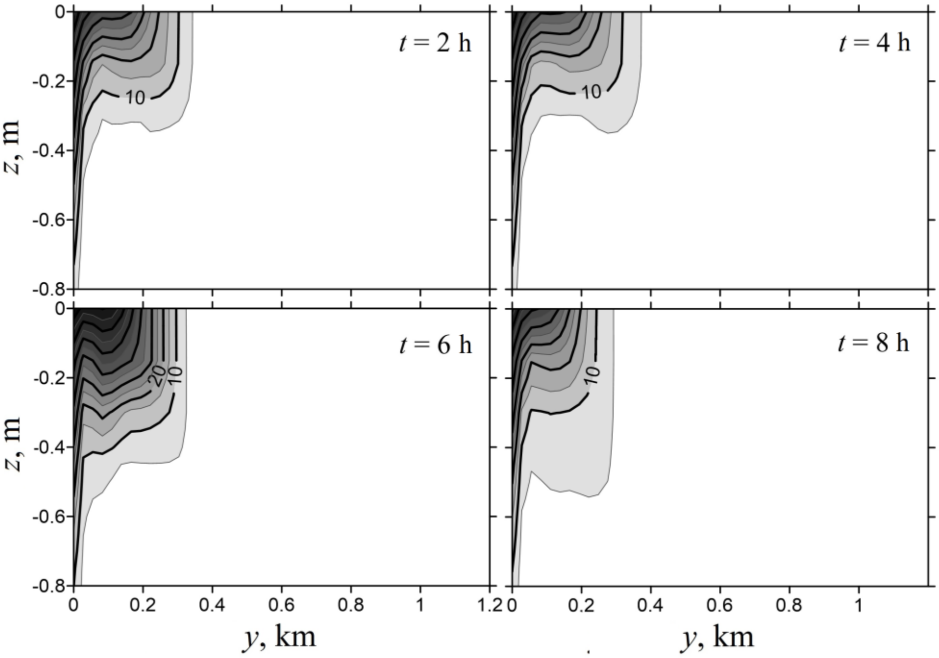

Fig. 10. Field $C(x_p, y, z, t)$ with unsteady wind of the form (2) for four time stations

Conclusion

Based on the analysis of the results of numerical modeling of the water salinity field in the area of the mouth of the Salgir River, the following conclusions were drawn.

Under the influence of river runoff, a plume is formed at the outlet of the river mouth in the form of a low salinity area extended towards the bay. Over time, the plume spreads in all directions and increases in size. Without taking into account the Earth's rotation, the shape of the plume is symmetrical with respect to the position of the source (river mouth). When the Earth's rotation is taken into account, the plume shifts to the right side of the mouth. This asymmetry in the shape of the plume manifests itself regardless of whether there are any currents in the basin.

When the Earth's rotation is taken into account, the influence of the direction of alongshore currents on the shape of the plume turns out to be significant. In the case of an associated current (directed to the right from the mouth), the plume is more elongated and pressed against the shore compared to the case of a counter current (directed to the left from the mouth). Subject to the existence of associated currents, the transverse size of the plume decreases by about a factor of two. When the wind is directed from the shore, the resulting currents stretch the plume in the transverse direction. When the wind is directed towards the shore, the plume is blocked and fresh water spreads in a narrow strip on both sides of the river mouth.

The water salinity field has a well-defined two-layer structure. The plume is concentrated in the upper layer with a thickness of 15–40 cm. In the immediate vicinity of the river mouth, the thickness of the upper layer decreases, which is due to the effect of buoyancy – the rise of fresh water coming from the bottom layers of the river to the surface of the basin.

The results obtained in the work are preliminary, since the simplified geometry of the basin and the simplest current fields were used in the model. In the future, it is planned to study the dynamics of the plume, taking into account real bathymetry, real wind fields, and different types of the equation of sea water state.

REFERENCES

1. Dyakov, N.N. and Belogudov, A.A., 2015. Water Exchange of the Gulf Sivash with the Sea of Azov through the Strait Genichesk (Thin). In: SOI, 2015. *Proceedings of N.N. Zubov State Oceanographic Institute*. Moscow: Artifex. Iss. 216, pp. 240–253.
2. Sovga, E.E., Eremina, E.S. and Khmara, T.V., 2018. Water Balance in the Sivash Bay as a Result of Variability of the Natural-climatic and Anthropogenic Factors. *Physical Oceanography*, 25(1), pp. 67–76. doi:10.22449/1573-160X-2018-1-67-76
3. Evstigneev, V.P. and Eremina, E.S., 2019. Calculation of Precipitation over the Sivash Bay. *Ecological Safety of Coastal and Shelf Zones of Sea*, (2), pp. 19–29. doi:10.22449/2413-5577-2019-2-19-29 (in Russian).
4. Eremina, E.S. and Evstigneev, V.P., 2020. Inter-Annual Variability of Water Exchange between the Azov Sea and the Sivash Bay through the Tonky Strait. *Physical Oceanography*, 27(5), pp. 489–500. doi:10.22449/1573-160X-2020-5-489-500

5. Lomakin, P.D., 2021. Features of the Oceanological Values Fields in the Sivash Bay (The Sea of Azov). *Physical Oceanography*, 28(6), pp. 647–659. doi:10.22449/1573-160X-2021-6-647-659
6. Fong, D.A. and Geyer, W.R., 2002. The Alongshore Transport of Freshwater in a Surface-Trapped river Plume. *Journal of Physical Oceanography*, 32(3), pp. 957–972. https://doi.org/10.1175/1520-0485(2002)032<0957:TATOFI>2.0.CO;2
7. Yankovsky, A.E., Lemeshko, E.M. and Ilyin, Y.P., 2004. The Influence of Shelfbreak Forcing on the Alongshelf Penetration of the Danube Buoyant Water, Black Sea. *Continental Shelf Research*, 24(10), pp. 1083–1098. https://doi.org/10.1016/j.csr.2004.03.007
8. Osadchiev, A.A. and Zavialov, P.O., 2013. Lagrangian Model of a Surface-Advected River Plume. *Continental Shelf Research*, 58, pp. 96–106. doi:10.1016/j.csr.2013.03.010
9. Osadchiev, A. and Korshenko, E., 2017. Small River Plumes off the Northeastern Coast of the Black Sea under Average Climatic and Flooding Discharge Conditions. *Ocean Science*, 13(3), pp. 465–482. doi:10.5194/os-13-465-2017
10. Fomin, V.V., Polozok, A.A. and Fomina, I.N., 2015. Simulation of the Azov Sea Water Circulation Subject to the River Discharge. *Physical Oceanography*, (1), pp. 15–26. doi:10.22449/1573-160X-2015-1-15-26
11. Tsyganova, M.V., Lemeshko, E.M., Ryabcev, Yu.N., 2016. Modelling of Hydrofront Forming on the Danube Mouth Area. *Ecological Safety of Coastal and Shelf Zones of Sea*, (3), pp. 26–31 (in Russian).
12. Ivanov, V.A. and Fomin, V.V., 2010. *Mathematical Modeling of Dynamical Processes in the Sea–Land Area*. Kiev: Akademperiodica, 286 p.
13. Ivanov, V.A., Fomin, V.V. and Polozok, A.A., 2017. Propagation of Contaminated Water from a Nonstationary Underwater Source in a Stratified Environment with the Vertical Shift of the Current Velocity. *Ecological Safety of Coastal and Shelf Zones of Sea*, (4), pp. 4–13 (in Russian).
14. Smagorinsky, J., 1963. General Circulation Experiments with the Primitive Equations. I. The Basic Experiment. *Monthly Weather Review*, 91(3), pp. 99–164. https://doi.org/10.1175/1520-0493(1963)091<0099:GCEWTP>2.3.CO;2
15. Mellor, G.L. and Yamada, T., 1982. Development of a Turbulence Closure Model for Geophysical Fluid Problems. *Reviews of Geophysics*, 20(4), pp. 851–875. https://doi.org/10.1029/RG020i004p00851
16. Fomin, V.V., 2006. Application of TVD Schemes to Numerical Modeling of Frontal Salinity Zones in a Shallow Sea. *Russian Meteorology and Hydrology*, (2), pp. 39–47.

Submitted 02.02.2022; accepted after review 25.02.2022;
revised 08.07.2022; published 25.09.2022

About the authors:

Vladimir V. Fomin, Head of Department of Computer Engineering and Mathematical Modeling, Marine Hydrophysical Institute of RAS (2 Kapitanskaya St., Sevastopol, 299011, Russian Federation), Dr.Sci. (Phys.-Math.), **ORCID ID: 0000-0002-9070-4460**, *fomin.dntmm@gmail.com*

Anton A. Polozok, Senior Engineer-Programmer, Marine Hydrophysical Institute of RAS (2 Kapitanskaya St., Sevastopol, 299011, Russian Federation), **ORCID ID: 0000-0002-0825-8669**, *polozok.umi@gmail.com*

Contribution of the authors:

Vladimir V. Fomin – statement of the problem, calculations, analysis of simulation results and preparation of the article

Anton A. Polozok – model data processing and preparation of the article

All the authors have read and approved the final manuscript.

DOI: 10.22449/2413-5577-2022-3-43-53

Numerical Modeling of Extreme Flash Flood in Yalta in September 2018

I. A. Svisheva, A. E. Anisimov *

Marine Hydrophysical Institute of RAS, Sevastopol, Russia
**e-mail: anatolii.anisimov@mhi-ras.ru*

Abstract

The paper considers the results of numerical modeling of the extreme flash flood in Yalta on September 6, 2018, which led to a number of negative socio-economic consequences. The flood occurred as a result of extreme rainfall on the Ai-Petri plateau, Yalta and Gurzuf yailas. The purpose of the study was to obtain and analyze the quantitative characteristics of flash floods based on modern methods of numerical modeling of hydrological processes. To achieve it, the WRF-Hydro hydrological model with a spatial resolution of 90 m was adapted to the territory of Crimea. The atmospheric forcing fields for WRF-Hydro were based on the verified convective-resolving WRF simulations. Quantitative characteristics of surface runoff and channel discharge of mountain rivers were obtained, and hydrographs of discharge at their mouths were constructed. It is noted that the main inflow into the rivers occurs in the upper reaches in the area of the plateau and mountain slopes, and this is true both for the total surface and channel runoff. The channel discharge is characterized by a sharp rise and a gradual decrease in time; within 9 hours from the start of the rainfall, most of the moisture reached the mouths of the rivers. The maximum calculated discharge values for the Derekoika (6 m^3/s) and Uchan-Su (8 m^3/s) Rivers are less than historical peaks, but they are in good agreement with typical discharge estimates during extreme flash floods in the warm season. The significant channel discharge is also reproduced for other rivers of the southern coast of Crimea, in particular for the Avunda River.

Keywords: hydrological modeling, Crimea, precipitation, flash flood, WRF-Hydro

Acknowledgements: the study was carried out under state assignment no. 0555-2021-0002 of FSBSI FRC MHI RAS “Fundamental studies of the interaction processes in the ocean-atmosphere system conditioning the regional spatial-temporal variability of natural environment and climate”.

For citation: Svisheva, I.A. and Anisimov, A.E., 2022. Numerical Modeling of Extreme Flash Flood in Yalta in September 2018. *Ecological Safety of Coastal and Shelf Zones of Sea*, (3), pp. 43–53. doi:10.22449/2413-5577-2022-3-43-53

Численное моделирование экстремального ливневого паводка в Ялте в сентябре 2018 года

И. А. Свищева, А. Е. Анисимов *

Морской гидрофизический институт РАН, Севастополь, Россия
**e-mail: anatolii.anisimov@mhi-ras.ru*

Аннотация
В работе рассмотрены результаты численного моделирования случая экстремального ливневого паводка в Ялте 6 сентября 2018 г., приведшего к ряду негативных социо-экономических последствий. Паводок произошел в результате выпадения экстремального количества осадков на плато Ай-Петри, Ялтинской и Гурзуфской яйлах. Цель исследования состояла в получении и анализе количественных характеристик ливневого паводка на основе современных методов численного моделирования гидрологических процессов. Для ее достижения к территории Крыма была адаптирована гидрологическая модель *WRF-Hydro* с пространственным разрешением 90 м. В качестве входных полей данных использовались верифицированные результаты расчета по атмосферной модели *WRF* с конвективно-разрешающим шагом по пространству. Получены количественные характеристики поверхностного стока и руслового расхода горных рек, построены гидрографы расхода в их устьях. Отмечено, что основной приток в реки происходит в верховьях в районе плато и горных склонов, причем это верно как для общего поверхностного, так и для руслового стока. Русловый расход характеризуется резким подъемом и постепенным по времени снижением, за 9 ч с момента начала ливня бóльшая часть влаги достигла устьев рек. Максимальные рассчитанные значения расхода для Дерекойки (6 м^3/с) и Учан-Су (8 м^3/с) меньше, чем пиковые значения, наблюдавшиеся в прошлые периоды, однако они хорошо согласуются с типичными оценками расхода при экстремальных ливневых паводках в теплое время года. Значимый русловый расход воспроизводится и для прочих рек Южного берега Крыма, в частности для р. Авунды.

Ключевые слова: гидрологическое моделирование, Крым, осадки, экстремальный ливневый паводок, *WRF-Hydro*

Благодарности: работа выполнена в рамках государственного задания ФГБУН ФИЦ МГИ по теме № 0555-2021-0002 «Фундаментальные исследования процессов взаимодействия в системе океан – атмосфера, определяющих региональную пространственно-временную изменчивость природной среды и климата».

Для цитирования: *Свищева И. А., Анисимов А. Е.* Численное моделирование экстремального ливневого паводка в Ялте в сентябре 2018 года // Экологическая безопасность прибрежной и шельфовой зон моря. 2022. № 3. С. 43–53. doi:10.22449/2413-5577-2022-3-43-53

Introduction

The mountainous regions of the Black Sea region are characterized by shower-type atmospheric precipitation, which causes extreme floods on rivers, called *flash floods* in the English-language literature [1]. These are short-term, but extremely intense phenomena, bringing significant socio-economic damage. A flood is known on the rivers of the southern coast of Crimea on June 19–20, 1987, as well as floods in the 1960s, when historical maximums of water flow were recorded on the Derekoika and Uchan-Su (Vodopadnaya) Rivers in Yalta. In June 2021, according to the data from gauging stations, the discharges of these rivers exceeded the norm by 3.4–6.0 times and set new records. The water level at that time rose by more than one and a half meters: on June 18, 2021, the water level rose by 167 cm on the Derekoika River, and by 163 cm on the Vodopadnaya River. Hundreds of houses were damaged in Yalta, 117 streets are in need of major repairs or reconstruction. Global warming makes this problem even more urgent due to the increase in the frequency and intensity of rainstorms in the region. It is known that in other regions the forecast of such hazardous phenomena based on hydrological numerical models [2] has been introduced into operational practice, while in Crimea this issue has been bypassed. Adaptation, testing and evaluation of the reproducibility of such extreme hydrological phenomena in the Crimean territory is a very relevant scientific and applied task. The purpose of this study was to obtain and analyze the quantitative characteristics of the flash flood in Yalta in September 2018 based on the use of modern methods of numerical modeling of hydrological processes.

Materials and methods

In modern conditions, it is possible to use numerical models of river runoff to determine the probability of occurrence of extreme flush floods and construct scenarios for their development. In particular, the WRF-Hydro model has been adapted for Crimea. This model consists of four main blocks: models of the earth's surface, surface water, groundwater and channel runoff.

Input data

As input data with a discreteness of 1 hour in time and 900 m in space, the following results of calculations using the WRF atmospheric model with the ARW dynamic core[1] with a convective-resolving step in space are used: shortwave and longwave radiation, specific humidity and air temperature at a height of 2 m, atmospheric pressure at the surface, wind speed component at a height of 10 m, quantity of precipitation, properties of the underlying surface (share of vegetation, LAI (Leaf Area Index)). The description of the numerical experiment and the WRF model configuration is given in [3, 4]. The terrain data is generated based on the HydroSHEDS data from the Shuttle Radar Topography Mission satellite instrument with a resolution of 90 m [5]. Since the fallout of extreme precipitation and the occurrence of a flash flood are fast processes, the WRF-Hydro calculation was performed for an interval of one day. The initial time point of the calculation was taken to be 6 hours from the beginning of precipitation, as in earlier works on the rivers of this region [6].

NOAH Land Surface Model

In the NOAH one-dimensional model of the land surface with a spatial resolution of 900 m, based on the radiation-heat balance equation, the vertical fluxes and the heat and moisture content of the soil are calculated. Taking into account the properties of the underlying surface, data on vegetation and soil porosity, the following are calculated: the amount of moisture retained by the forest canopy, direct evaporation from the soil surface and vegetation cover, transpiration, surface and subsurface

---

[1] Skamarock, W.C, Klemp, J.B., Dudhia, J., Gill, D.O., Liu, Z., Berner, J., Wang, W., Powers, J.G., Duda, M.G. et al., 2019. *A Description of the Advanced Research WRF Model*. Version 4. NCAR/TN-556+STR. Boulder: NCAR, 148 p. doi:10.5065/1dfh-6p97

runoff, moisture flow into the soil. The depth of the soil layers in WRF-Hydro can be set manually, while the total depth of the soil column and the thickness of the individual soil layers are constant throughout the model area. In our case, in a two-meter soil column in WRF-Hydro, four layers of soil are used with a thickness from top to bottom of 100, 300, 600 and 1000 mm. The land cover classification is given according to the USGS or MODIS Modified IGBP product; the soil classifications are provided by the STATSGO database with a step of 1 km [7].

After calculating NOAH, the model variables (excess infiltration (surface runoff), depth of accumulated water and soil moisture) are interpolated from the low-resolution grid (900 m) to the high-resolution grid (90 m) and fed to the groundwater and surface water modules. The underground runoff occurs on a coarse grid, while ground runoff occurs on a fine grid. WRF-Hydro then calculates the groundwater depth according to the depth of the upper subsurface saturated soil.

Underground runoff

In WRF-Hydro, the underground lateral runoff is calculated before surface runoff to ensure that exfiltration from fully saturated grid cells is added to the excess infiltration calculated by the land surface model, which ultimately updates the surface head value for surface runoff. The mass balance for each cell at the model time step Δt can be calculated from the change in groundwater level Δz:

$$\Delta z = \frac{1}{\varphi(i,j)} \frac{Q_{net(i.j)}}{A} \Delta t,$$

where φ is soil porosity; A is cell area; Q_{net} is horizontal flow of saturated underground moisture for a cell i, j:

$$Q_{net(i,j)} = h_{i,j} \sum \gamma_{x(i,j)} + h_{i,j} \sum \gamma_{y(i,j)},$$

where $h_{i,j} = \left(1 - \frac{z_{i,j}}{D_{i,j}}\right)^{n_{i,j}}$ and $\gamma_{x,y(i.j)} = -\left(\frac{w_{i,j} Ksat_{i,j} D_{i,j}}{n_{i,j}}\right) \cdot \beta_{x,y_{(i,j)}}$.

Here z is groundwater level; D is soil thickness; $Ksat$ is saturated hydraulic conductivity; n is the parameter that determines the rate of decrease of $Ksat$ with depth (= 1 at present); w is cell width specified for a regular grid; β is groundwater level slope (calculated as the ratio of the difference in groundwater depth between two adjacent grid cells to the grid step).

This method considers the soil as a single homogeneous column. Therefore, the change in groundwater depth needs to be re-mapped to the soil layers of the land surface model. Considering the timescale of groundwater movement and the limitation in the model structure, there is considerable uncertainty in the time required for the proper “acceleration” of groundwater systems.

Surface runoff

At the next stage, surface runoff is determined. Hydraulic gradients are approximated as the slope of the groundwater level between adjacent grid cells using the D8 steepest descent method [8]. A fully non-stationary, explicit finite-difference diffusion wave formulation [9] with a later modification by Ogden is a way of representing land runoff that occurs when the depth of water in a grid cell exceeds the retention depth. As in [9], the continuity equation for a ground-based one-dimensional flood wave is combined with a diffusion wave formulation of the momentum equation. To account for friction, the Manning equation is used, indicating the roughness coefficient for surface runoff. This coefficient was obtained from [10] and compared with land cover classifications.

For terrain scales ranging from 30 to 300 m, the diffuse wave formulation is a simplification of the more general Saint-Venant equations for shallow water. The two-dimensional continuity equation for a flood wave flowing around the land surface has the following form:

$$\frac{\partial h}{\partial t}+\frac{\partial q_l}{\partial l}=i_e,$$

where h is surface current depth; i_e is excess infiltration; q_l is unit flow in the direction of the steepest descent l, calculated using the Manning equation $q_l = \alpha_l h^{\beta}$, where $\beta = \frac{5}{3}$; $\alpha_l = \frac{S_{fl}^{1/2}}{n_{OV}}$; n_{OV} is surface roughness factor (adjustable parameter); S_{fl} is friction slope in the direction of l, calculated from the momentum equation for the direction l: $S_{fl} = S_{ol} - \frac{\partial h}{\partial l}$, where S_{ol} is the slope of the terrain in the direction l; $\partial h/\partial l$ is change in the depth of the water surface in the direction l.

Channel runoff

WRF-Hydro has additional modules for representing flow processes in river channels. The inflow into the river network is a unidirectional process, i.e. it is always positive with respect to the channel element. If the runoff layer in the grid cells labeled “channel” exceeds the local depth of retained waters, then excess runoff volume is transferred from the surface water model to the channel model.

As a rule, inflow into the channel is based on the calculation of the mass balance. Water is directed to the channel when the stored water depth of the channel grid cells exceeds the set retention depth. The depth of the water stored in any grid cell is a combination of local excess infiltration, the amount of water entering the grid cell from surface runoff, and exfiltration from groundwater. Each cell of the channel network is represented in the form of a trapezoid, as shown in Fig. 1.

The channel side slope (z), bottom width (B_w) and roughness (n) are currently set by default as functions of the Strahler flow order. Flow order is a positive integer used in geomorphology and hydrology to indicate the level of branching

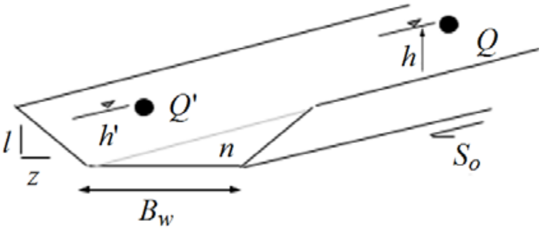

Fig. 1. Channel scheme. S_o – channel slope; z (m) – side slope; B_w (m) – bottom width

in a river system. Strahler's method sets the lowest order (number 1) starting from headwaters, which is the highest point. Each segment of a stream or a river is treated as a node in a tree. When two streams of the same order merge, they form a stream of the next order. When streams of lower order merge into a stream of higher order, the stream orders do not change. Note that the definition of channel runoff parameters as a function of flow order is correct for relatively small watersheds (as in our case), but not for large regions.

Channel cells receive horizontal inflow from surface runoff, which is effectively unidirectional. Thus, when a river overflows its banks, the flood areas are not explicitly reproduced in WRF-Hydro. To integrate the equations of the diffusion wave flow, the Newton-Raphson solution of the first order is used. Unlike land flood waves, channel flood waves have much greater flow depths and wave amplitudes, which can potentially lead to large momentum gradients and strong acceleration of the propagating wave. To correctly reproduce such flood waves, it is necessary to correctly set the time steps of the model in order to satisfy the Courant conditions. In WRF-Hydro, the diffuse wave module for channel runoff uses a variable time step: the initial value of the time step is set equal to the time step of the surface runoff model. This step is, in turn, a function of the grid step (in our case, 5 s). If during model integration the Newton-Raphson convergence criteria for upstream and downstream flow rates are not met, the time step of the channel model is halved and the scheme for solving the Newton-Raphson equation is repeated 2).

Results

Fig. 2, *a* shows the channel network of the WRF-Hydro model according to the data on a finite difference grid with a resolution of 90 m. The main attention is paid to the runoff of the Uchan-Su and Derekoika rivers, which flow into the Yalta Bay. Fig. 2, *b* shows the precipitation field for September 6, 2018, used as input. Most of the daily precipitation fell from 06:00 to 09:00 UTC. The maximum amount of precipitation was noted on the Ai-Petri plateau and the Yalta Yaila (about 100 mm). In the area of the Gurzuf Yaila, which belongs to the catchment

---

2) Gochis, D., Barlage, M., Cabell, R., Dugger, A., FitzGerald, K., McAllister, M., McCreight, J., RaieeiNasab, A., Read, L. et al., 2020. *The WRF-Hydro Modeling System. Technical Description*. Version 5.1.1. NCAR Technical Note. 107 p. Available at: https://ral.ucar.edu/sites/default/files/public/projects/wrf_hydro/technical-description-user-guide/wrf-hydro-v5.1.1-technical-description.pdf [Accessed: 10 September 2022].

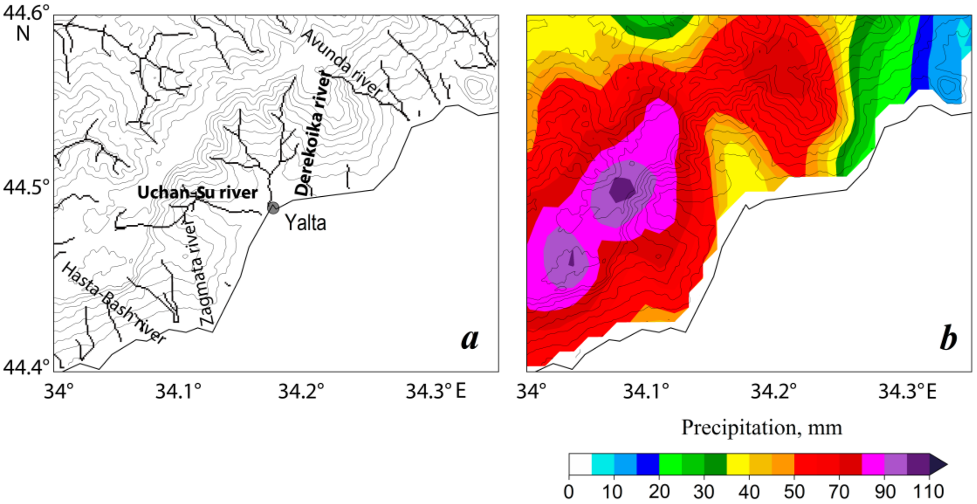

Fig. 2. Channel network of WRF-Hydro model (*a*) and precipitation amount for 6 September 2018 based on WRF model (*b*)

area of the Derekoika River, about 70 mm of precipitation fell. Precipitation estimates were obtained from the data of the WRF model and were verified using observational data at meteorological stations and radar measurements [3].

Fig. 3 shows that the main inflow into the rivers occurs in the upper reaches in the area of the Ai-Petri plateau and mountain slopes, where the total runoff for 12 hours exceeds 30 mm, or even 40 mm, and the surface water level is above 10 mm. In the lower reaches, the total runoff for 12 hours is less than 20 mm, and the level is less than 2 mm. The maximum values of the fields of total surface runoff correspond to the maximum values of precipitation at the Ai-Petri and Gurzuf Yaila. In the level fields, the maximum values are noted in the area of the Gurzuf Yaila, where precipitation fell somewhat later than on the Ai-Petri. Let us note that the proportion of moisture that enters the surface runoff and is transferred for calculation to the surface moisture distribution module is calculated using the NOAH land surface model and is determined by a number of tuning parameters depending on the properties and moisture content of the soil. In turn, the value of the surface moisture level on a finer 90-meter grid is calculated in the surface runoff module and is mainly determined by the relief.

Let us consider the total inflow into the channels calculated by the model and the values of the channel discharge. As well as surface runoff, the total inflow into the channels for 12 hours (Fig. 4, *a*) in the upper reaches of the rivers exceeds 30 mm, and in the lower reaches does not even reach 5 mm. According to the channel discharge modeling results at 09:00 on September 6, 2018 (Fig. 4, *b*), most of the moisture had almost reached the mouths of the rivers by that moment. As a result of the already noted earlier precipitation on the Ai-Petri, the maximum channel discharge for the Uchan-Su is also reproduced earlier than for the Derekoika. Significant (> 5 m^3/s) channel discharge is also reproduced for the Avunda River near Gurzuf.

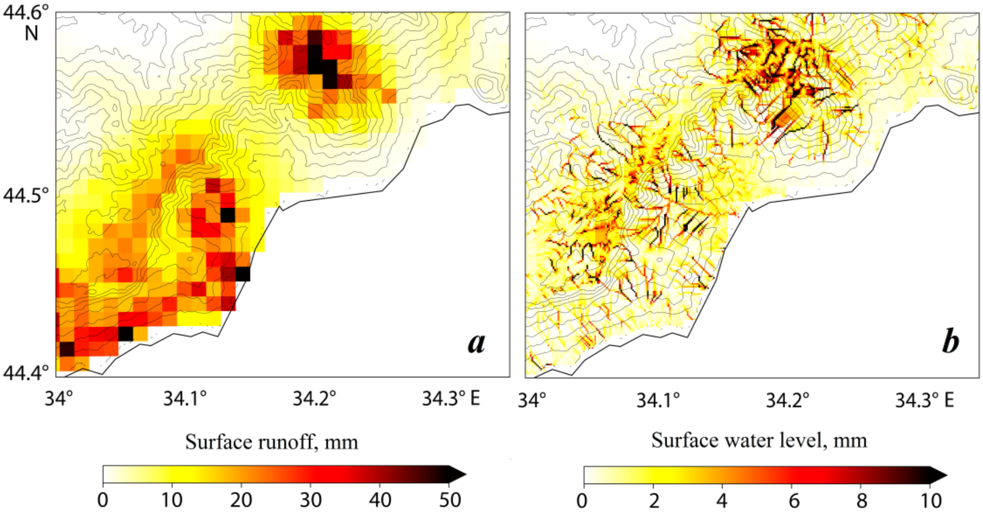

F i g . 3 . Total surface runoff for 12 h on 6 September 2018 (*a*) and the surface water level at 8:00 UTC (*b*)

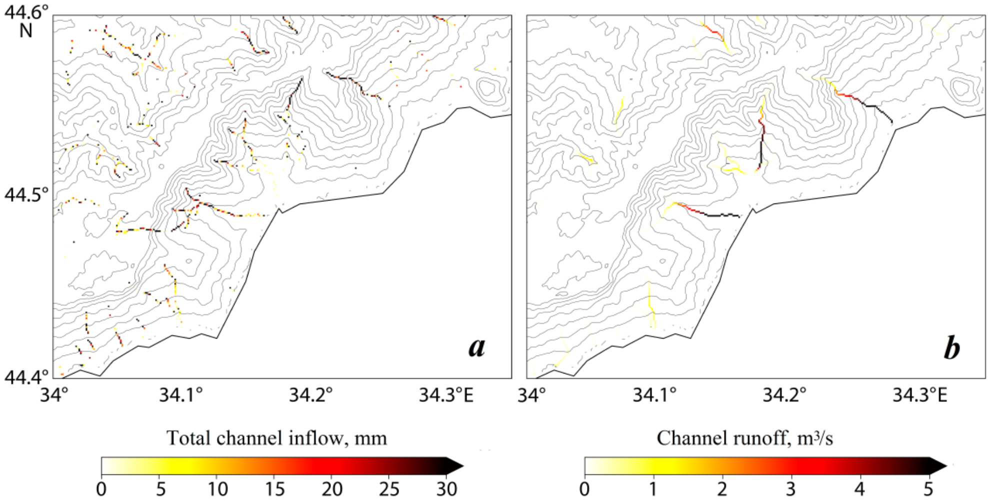

F i g . 4 . Total channel inflow for 12 h on 6 September 2018 (*a*) and channel runoff at 9:00 (*b*)

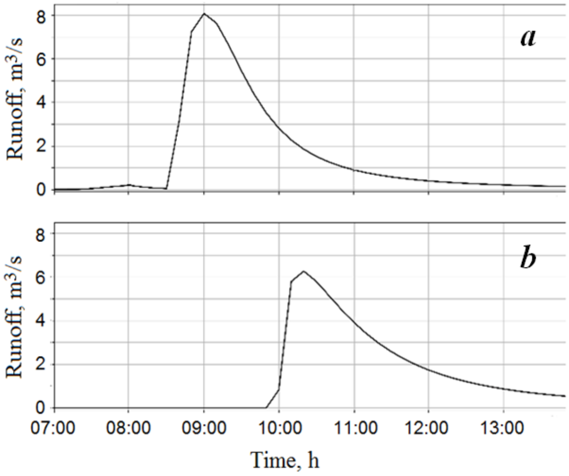

Fig. 5. Runoff at the mouths of the Derekoika (*a*) and Uchan-Su (*b*) Rivers for 6 September 2018

The maximum channel discharge of the Uchan-Su (8 m^3/s) and Derekoika (6 m^3/s) (Fig. 5) is less than the peak discharge values observed in the past, but it is in good agreement with typical estimates of discharge during flash floods during the warm season [11, 12]. Discharge is characterized by a sharp rise and a gradual decrease over time. The absence of discharge during the time preceding the onset of the flood is associated with a short "acceleration" model period. Let us note that our discharge estimates for the Derekoika River are slightly lower than those obtained in another work using the Hydrograph model, where the discharge estimate exceeded the maximum observed values (14.9 m^3/s) [13]. This result seems to be due to the lower total precipitation in the WRF-Hydro model input.

Conclusion

As a result of numerical modeling of the flash flood in Yalta on September 6, 2018, using WRF-Hydro, quantitative characteristics of surface runoff and channel discharge of mountain rivers on the Southern coast of Crimea were obtained. The flood occurred as a result of extreme rainfall on the Ai-Petri plateau. The WRF-Hydro model was adapted to the territory of the Southern Coast of Crimea and integrated with a spatial resolution of 90 m. The use of input data from the WRF atmospheric model with a convective-resolving spatial step made it possible to take into account the structure of precipitation and reproduce the main characteristics of the flood. As a result of the work, quantitative characteristics of surface runoff and channel discharge of mountain rivers were obtained. The maximum channel discharge of the Derekoika (6 m^3/s) and Uchan-Su (8 m^3/s) rivers is less than the peak discharge values observed in the past and obtained in other works, however, it is in good agreement with typical discharge estimates during flash floods in warm seasons.

REFERENCES

1. Kuksina, L.V., Golosov, V.N. and Kuznetsova, Yu.S., 2017. Cloudburst Floods in Mountains: State of Knowledge, Occurrence, Factors of Formation. *Geography and Natural Resources*, 38(1), pp. 20–29. doi:10.1134/S1875372817010036
2. Givati, A., Fredj, E. and Silver, M., 2016. Operational Flood Forecasting in Israel. In: T. E. Adams and T. C. Pagano, eds., 2016. *Flood Forecasting*. Academic Press. Chapter 6, pp. 153–167. https://doi.org/10.1016/B978-0-12-801884-2.00006-2
3. Anisimov, A., Efimov, V., Lvova, M., Mostamandy, S. and Stenchikov, G., 2022. Cloud-Resolving Modeling and Evaluation of Microphysical Schemes for Flash Flood-Producing Convection over Black Sea. *Journal of Hydrometeorology* (in Press).
4. Efimov, V.V., Anisimov, A.E. and Komarovskaya, O.I., 2021. Features of Summer and Winter Precipitation in the Northern Part of the Black Sea Region: Two Model Case Studies. *Physical Oceanography*, 28(6), pp. 677–690. doi:10.22449/1573-160X-2021-6-677-690
5. Lehner, B., Verdin, K. and Jarvis, A., 2008. New Global Hydrography Derived from Spaceborne Elevation Data. *Eos Transactions AGU*, 89(10), pp. 93–94. doi:10.1029/2008EO100001
6. Ivanov, V.A., Ovcharenko, I.A., Prusov, A.V. and Shokurov, M.V., 2012. Modeling of Extreme Flood Flows on the South Coast of the Crimea. *Reports of the National Academy of Sciences of Ukraine*, (8), pp. 79–84 (in Russian).
7. Miller, D.A. and White, R.A., 1998. A Conterminous United States Multilayer Soil Characteristics Dataset for Regional Climate and Hydrology Modeling. *Earth Interactions*, 2(2), pp. 1–26. https://doi.org/10.1175/1087-3562(1998)002<0001:ACUSMS>2.3.CO;2
8. Greenlee, D.D., 1987. Raster and Vector Processing for Scanned Linework. *Photogrammetric Engineering and Remote Sensing*, 53(10), pp. 1383–1387. Available at: https://www.asprs.org/wp-content/uploads/pers/1987journal/oct/1987_oct_1383-1387.pdf [Accessed: 10 July 2022].
9. Julien, P.Y., Saghafian, B. and Ogden, F.L., 1995. Raster-Based Hydrologic Modeling of Spatially-Varied Surface Runoff. *JAWRA Journal of the American Water Resources Association*, 31(3), pp. 523–536. https://doi.org/10.1111/j.1752-1688.1995.tb04039.x
10. Vieux, B.E., 2001. Distributed Hydrologic Modeling Using GIS. In: V. P. Singh, ed., 2001. *Distributed Hydrologic Modeling Using GIS*. Water Science and Technology Library, vol. 38. Dordrecht: Springer, pp. 1–17. https://doi.org/10.1007/978-94-015-9710-4_1
11. Ovcharuk, V.A., Prokofiev, O.M. and Todorova, E.I., 2015. Formation Features of Warm Period Floods on the Rivers of Mountain Crimea. *Visnyk of V.N. Kazarin Kharkiv National University, Series "Geology. Geography. Biology"*, 1157(42), pp. 99–106. https://doi.org/10.26565/2410-7360-2015-42-19 (in Russian).
12. Ivanov, V.A., Svishcheva, I.A., Prusov, A.V. and Shokurov, M.V., 2011. Prediction of Disastrous Flood Based on Regional Model of Atmospheric Circulation for the South Crimea Region. In: MHI, 2011. *Ekologicheskaya Bezopasnost' Pribrezhnykh i Shel'fovykh Zon i Kompleksnoe Ispol'zovanie Resursov Shel'fa* [Ecological Safety of Coastal and Shelf Zones and Comprehensive Use of Shelf Resources]. Sevastopol: ECOSI-Gidrofizika. Iss. 25, vol. 2, pp. 396–418 (in Russian).
13. Zemlyanskova, A.A., Makarieva, O.M., Nesterova, N.V. and Fedorova, A.D., 2020. Modeling of the Derekoyka River Runoff Formation in the Mountain Conditions of the Crimean Peninsula (Russia). In: O. M. Makarieva and A. A. Zemlianskova, eds., 2020. *Proceedings of International Scientific Conference in Memory of Outstanding Russian Scientist Yuri Vinogradov "IV Vinogradov Conference "Hydrology: From Learning to Worldview"*. St. Petersburg: Izdatelstvo VVM, pp. 78–83 (in Russian).

Submitted 5.04.2022; accepted after review 25.04.2022;
revised 08.07.2022; published 25.09.2022

About the authors:

Irina A. Svisheva, Junior Research Associate, Marine Hydrophysical Institute of RAS (2 Kapitanskaya St., Sevastopol, 299011, Russian Federation), **ORCID ID: 0000-0003-1501-3720, ResearcherID: M-4451-2018, Scopus Author ID: 57212347523,** *svishcheva.iryna@gmail.com*

Anatolii E. Anisimov, Senior Research Associate, Marine Hydrophysical Institute of RAS (2 Kapitanskaya St., Sevastopol, 299011, Russian Federation), Ph.D. (Phys.-Math.), **ORCID ID: 0000-0002-5530-5608, ResearcherID: ABA-1705-2020, Scopus Author ID: 42561044300**, *anatolii.anisimov@mhi-ras.ru*

Contribution of the authors:

Irina A. Svisheva – problem statement, qualitative and quantitative analysis of the results, model simulations, text and visualization preparation

Anatolii E. Anisimov – problem statement, model simulations, qualitative and quantitative analysis of the results, critical analysis and improvement of the text

All the authors have read and approved the final manuscript.

DOI: 10.22449/2413-5577-2022-3-54-70

Physical Modeling of the Effect of Tidal Sea Level Fluctuations on Wave-Absorbing Pebble Beaches

V. A. Petrov *, G. V. Tlyavlina, N. A. Yaroslavtsev

Research Center "Sea Coasts" (branch of JSC TsNIITS), Sochi, Russia
**e-mail: demmi8@mail.ru*

Abstract

Implementation of coastal protection measures on the coasts of the Arctic and Far Eastern seas with tidal phenomena determines increased requirements for the justification of design solutions when developing schemes for engineering protection of the shores. Wave-absorbing structures, including wave-absorbing beaches consisting of coarse-grained material, are the most effective ones for protecting coasts from the effects of waves. This is particularly true for northern seas, coasts of which are perpetually frozen. The calculation of such beaches should take into account the effect of periodical sea level fluctuations on the formed profile. Field studies of the effect of tidal sea level fluctuations on the profile of a wave-absorbing pebble beach are associated with certain difficulties. The most promising are experiments performed on hydraulic models in wave pools and flumes. The purpose of the work is to study in a wave flume the effect of tidal cycles on the profile of a wave-absorbing pebble beach. It was found that during high tide, when the initial backfill is exposed to waves, a beach profile is formed similar to the profile generated at a constant level corresponding to the maximum phase of the tide. At low tide, the pebble is displaced by waves seaward of the underwater border of the pebble beach formed at a constant water level. At high tide, the displaced pebble does not completely return to the upper part of the profile, which leads to a decrease in the width of the surface part of the beach and that in its wave damping efficiency. Based on studies performed in seas with a tide height of up to 3.6 m, when creating wave-absorbing pebble beaches, the volume of the initial backfill of beach-forming material must be increased by 5 % compared to the volume calculated for tidal seas.

Keywords: beach profile, high tide, hydraulic modeling, low tide, wave absorbing pebble beach

For citation: Petrov, V.A., Tlyavlina, N.A. and Yaroslavtsev, N.A., 2022. Physical Modeling of the Effect of Tidal Sea Level Fluctuations on Wave-Absorbing Pebble Beaches. *Ecological Safety of Coastal and Shelf Zones of Sea*, (3), pp. 54–70. doi:10.22449/2413- 5577-2022-3-54-70

Физическое моделирование влияния приливных колебаний уровня моря на волногасящие галечные пляжи

В. А. Петров *, Г. В. Тлявлина, Н. А. Ярославцев

Научно-исследовательский центр «Морские берега» (ОП АО ЦНИИТС), Сочи, Россия
**e-mail: demmi8@mail.ru*

Аннотация
Проведение берегозащитных мероприятий на побережье арктических и дальневосточных морей с приливо-отливными явлениями определяет повышенные требования к обоснованию проектных решений при разработке схем инженерной защиты берегов. Для защиты берегов от воздействия волн наиболее эффективными являются волногасящие сооружения, включая и волногасящие пляжи из крупнообломочного материала. Особенно это актуально для северных морей, на берегах которых распространена вечная мерзлота. При расчете таких пляжей необходимо учитывать влияние периодических колебаний уровня моря на формируемый профиль. Исследования влияния приливо-отливных колебаний уровня моря на профиль волногасящего галечного пляжа в природных условиях сопряжены с определенными сложностями. Наиболее перспективными являются эксперименты, выполняемые на гидравлических моделях в волновых бассейнах и лотках. Цель работы – исследование в волновом лотке влияния приливо-отливных циклов на профиль волногасящего галечного пляжа. Получено, что во время прилива при воздействии волн на исходную отсыпку формируется профиль пляжа, подобный профилю, вырабатываемому при постоянном уровне, соответствующем максимальной фазе прилива. При отливе галечный материал смещается под воздействием волн мористее подводной границы галечного пляжа, сформированного при постоянном уровне воды. Во время прилива смещенный галечный материал не полностью возвращается в верхнюю часть профиля, что приводит к уменьшению ширины надводной части пляжа и снижению его волногасящей эффективности. На основании выполненных исследований на морях с высотой прилива до 3.6 м объем исходной отсыпки пляжеобразующего материала при создании волногасящих галечных пляжей необходимо увеличить на 5 % по сравнению с объемом, рассчитанным для бесприливных морей.

Ключевые слова: волногасящий галечный пляж, гидравлическое моделирование, отлив, прилив, профиль пляжа

Для цитирования: *Петров В. А., Тлявлина Г. В., Ярославцев Н. А.* Физическое моделирование влияния приливных колебаний уровня моря на волногасящие галечные пляжи // Экологическая безопасность прибрежной и шельфовой зон моря. 2022. № 3. С. 54–70. doi:10.22449/2413-5577-2022-3-54-70

Introduction

The development of the northern seas resources is often associated with the implementation of coastal protection measures on their shores. Relatively low coastal areas composed mainly of easily eroded and perpetually frozen soils, and tidal phenomena determine the difficult natural conditions of the Arctic coasts. In this regard, increased requirements are imposed on the substantiation of design solutions in the development of engineering coastal protection schemes. The measures under development must totally meet environmental challenges and ecological requirements.

Under such unfavorable natural conditions, the most promising choice of coastal protection structures is the use of wave-absorbing permeable structures, such as berms made of stone or shaped solid monoliths, as well as the creation of wave-absorbing beaches filled with coarse-grained material, such as pebble or crushed stone. In this work, a wave-absorbing beach is a beach where the waves of the standard project storm are completely absorbed at a sea level of 1% probability.

The parameters of the profile of a wave-absorbing pebble beach formed under the influence of waves are basic for the calculation of the required volumes of dumped material. The method for determining the volumes of the initial dumping of the beach-forming material is based on the profile of relative dynamic equilibrium. This method is developed for tideless seas [1)] with negligible sea level fluctuations [1]. In tidal seas, sea level fluctuations of significant amplitude should affect the formed beach profile. Under natural conditions, field studies of the dynamics of profiles of a wave-absorbing pebble beach complicated by the influence of periodic tidal fluctuations in sea level present certain difficulties, which make it impossible to identify the features of such profiles and their differences from profiles formed at a constant sea level. One of the most promising methods for such studies is hydraulic modeling in wave basins and flumes.

The purpose of this work is to identify the differences between the profiles of a wave-absorbing pebble beach formed by waves under conditions of sea level tidal fluctuations, and the profiles formed at a constant water level.

Materials and methods of studies

Published sources do not contain any information about the stability of a wave-absorbing pebble beach created to protect an eroded coast from the effects of waves under tidal conditions, and about the profiles of such a beach formed from the material of the initial backfill of beach-forming material. In this regard, in the wave flume of the Research Center “Sea Coast” (Sochi), the formation of profiles of a wave-absorbing pebble beach during sea level tidal fluctuations was studied and compared with the beach profiles developed at a constant water level.

The effect of tidal phenomena on the formation of the profile of a wave-absorbing pebble beach was evaluated based on the results of laboratory experimental studies in comparison with the data obtained at a constant water level in the wave flume, which was taken as the water level in the high tide maximum phase. In addition, the initial conditions for the experiments and the wave parameters remained unchanged. Studies of the dynamics of the profile of a wave-absorbing pebble beach, filled in front of the coastal ledge to protect it from the effects of waves, were carried out at the maximum wave parameters that can occur at high tide sea level. At the beginning of each series of experiments, studies of the beach profile formed at the constant maximum water level were carried out. After that, experiments were carried out on the formation of profiles of a pebble

---

1) Smirnova, T.G., Pravdivets, Yu.P. and Smirnov, G.N., 2002. [*Coast Protection Structures*]. Moscow: Izd-vo Assotsiatsii stroitelnykh vuzov, 302 p. (in Russian).

beach during tidal cycles with different initial conditions for the impact of waves on the initial backfill of beach-forming material. Comparison of the results of experimental studies at constant and variable water levels made it possible to evaluate the effect of tidal phenomena on the formation of the profile of a wave-absorbing pebble beach.

The Froude number was used as the main criterion for the wind waves modeling [2]) [2]. According to this criterion, the dimensions of the structures on the model, the depths and elements of the waves are taken on a linear scale. The time of wave impact on the studied beach model is determined taking into account the time scale equal to the square root of the selected model scale. At the same time, the duration of high and low tide in kind was taken equal to 12 hours. On the approaches to the beach, regular waves were reproduced. The scale of the model of the underwater slope and hydraulic structures was chosen based on the size of the reproduced bottom and wave elements. The bottom of the model should be made rigid; when it is rough, at least five wavelengths should be placed on it.

The wave heights on the model were measured by capacitive wave recorders DUE-1 with the processing of the measurement results on a computer, and also controlled by a ruler (Fig. 1).

Preliminarily, the wave height sensors were calibrated during their stepwise immersion to a certain depth. The recording of the excitement in the basin was accompanied by photography and video recording. The wavelength was recorded by shooting near the wave recorders against the background of a grid applied to the side wall of the flume.

According to the theory of similarity, it is necessary to study the process of wave impact on structures on a hydraulic model while ensuring the geometric similarity of the model to a full-scale object, the similarity of the wave regime, the similarity of surface and volume forces, i.e. it is necessary to ensure the equality of all defining criteria. In the general case, it is almost impossible to fulfill all

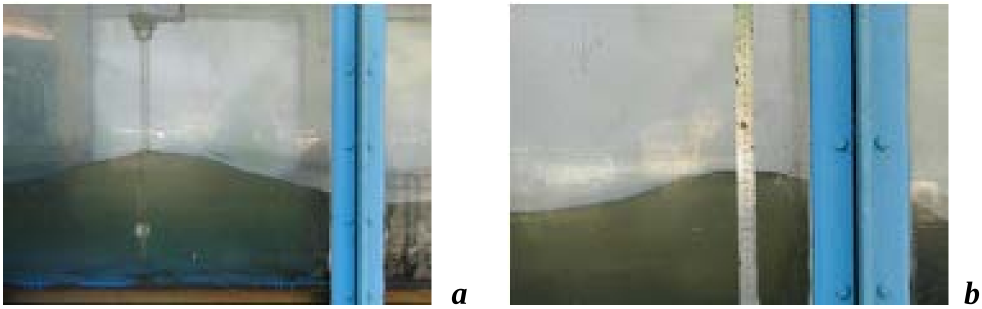

Fig. 1. Determination of wave heights on the model using capacitive wave recorders DUE (*a*) and a ruler (*b*)

---

[2]) Kirkegaard, J., Wolters, G., Sutherland, J., Soulsby, R., Frostick, L., McLelland, S., Mercer, T. and Gerritsen, H., 2011. *Users Guide to Physical Modelling and Experimentation: Experience of the HYDRALAB Network*. London: CRC Press, 272 p. https://doi.org/10.1201/b11335

these conditions. In particular, if the same liquid is used on the model as in natural conditions, then it is impossible to simultaneously provide similarity in Froude (Fr) and Reynolds (Re) numbers. However, for a number of problems of great practical importance, similarity in both parameters is not required [3].

Thus, with the only wave motion or the impact of non-breaking waves on hydraulic structures, when the viscosity influence is small, the dynamic similarity of model and natural processes is determined by the equality of the Froude numbers. When studying waves on the surface of incompressible fluid, the Froude criterion can be written as follows

$$\mathrm{Fr} = \frac{h}{gT^2}, \tag{1}$$

where h – height of waves; g – gravitational acceleration; T – period of waves.

Limitations on wave parameters are conditioned upon the need to eliminate the noticeable influence of molecular viscosity and capillary effects. Capillarity (or surface tension) can be ignored if the wavelength on the model λ_m is greater than 20 cm [4]

$$\lambda_m > 20 \text{ cm}. \tag{2}$$

To neglect the internal dissipation of wave energy due to viscosity, condition [5] should be satisfied

$$\lambda_m > 400\sqrt{\upsilon \cdot T}, \tag{3}$$

where υ – kinematic viscosity of the fluid.

Another class of problems on the motion of a fluid with free surface includes cases when the friction in the fluid is significant, but the influence of molecular viscosity can be neglected. Examples of this kind are flows with highly developed turbulence at high Reynolds numbers. Such problems include problems on the interaction of waves with immersed barriers or permeable structures. The question of modeling of resistance forces or forces of hydrodynamic action in these cases can be reduced to the question of modeling of shape and mass of structural elements of constructions. Of course, it should be borne in mind that there is a lower limit on the size of the model, which is determined from the following conditions: the flow on the model must be turbulent and self-similar in terms of the Reynolds number [3]. When flowing around the bodies of various shapes, these requirements will be met if

$$\mathrm{Re} = \frac{V_m \cdot L_m}{\upsilon} \geq 500 \div 1000, \tag{4}$$

where V_m – characteristic speed on the model; L_m – characteristic size of an immersed body.

When liquid flows through holes in permeable screens (jets), self-similarity in the Reynolds number will take place if

$$\mathrm{Re} = \frac{V_m \cdot \delta_m}{\upsilon} \geq 100, \tag{5}$$

where δ_m – characteristic hole size.

The interaction of waves with a permeable dump becomes independent of the Reynolds number at

$$\mathrm{Re} = \frac{V_m \cdot D_m}{\upsilon} \geq 1000, \qquad (6)$$

where D_m – dump element size.

Since the wave length is assumed to be more than 0.7 m in the hydraulic model in the wave basin, the influence of the surface tension and molecular viscosity of the liquid on the research results will be insignificant (see formulas (2)–(6)). Therefore, the conclusion is that the processes under study on the models will be dynamically similar to natural ones. To ensure the equality of the Froude numbers (1) on the model and in natural conditions, the scale of the wave period will be as follows

$$m_t = \frac{T_m}{T_n} = \sqrt{m_l},$$

where index m refers to the model, and index n refers to actual values.

The scale of the mass of structural elements of constructions is taken as follows

$$m_G = \frac{G_m}{G_n} = m_l^3.$$

When performing studies with pebble beaches, it was taken into account that the experiments should be carried out while observing the geometric similarity of the model and sediments to the natural part of the coast and the similarity of the model wave regime to the natural one. At the same time, the density of sediments of beach material on the model and in natural conditions should be the same, and the processes occurring in the inshore zone of pebble beaches are modeled reliably when using sediments with an average size of at least 0.5 mm in experiments [6].

Experimental studies were carried out in a wave flume with its length of 20 m, width of 0.6 m, and wall height of 1 m. Waves were generated by a shield wave generator installed in a pit near the end wall.

The experiments were carried out on a scale of 1:30. For the selected scale, a 7.3 m (219 m) plywood underwater coastal slope, simulating drying height in front of the coastal slope at low tide, was installed with a pitch of 0.005, which, under natural conditions, corresponded to the average value of the bottom slopes within the drying height area. Here and elsewhere in the text, the values corresponding to field data are given in brackets. The adjunction of the coastal slope test unit with the bottom of the flume is also made of plywood 2.44 m (73 m) long, installed with a pitch of 0.082 (Fig. 2). To maintain the roughness of the bottom, a layer of sand was applied to the plywood. The water depth in front of the beach scarp, equal to 12.0 cm (3.60 m), corresponded to the maximum sea level at high tide and remained unchanged in all experiments. With such a length of the shallow water area and depth near the beach scarp, the height of the waves acting on the beach made 5.3 cm (1.60 m). The average period for waves of this height made 1.1 s (6.0 s) [7]. Constant change in the water level in the flume, simulating the phases of high tide and low tide, taking into account the time of their action

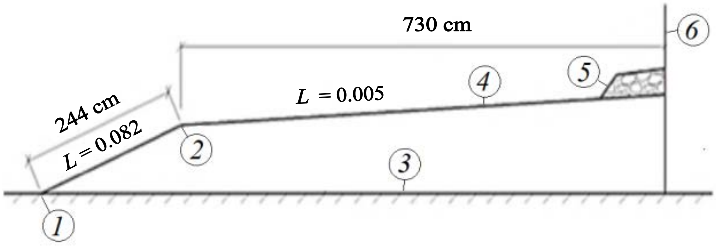

Fig. 2. Scheme of the model during wave flume studies of the profile dynamics of a pebble beach at tide: *1* – adjunction of the drying height with the test unit bottom; *2* – knee of the bottom profile; *3* – test unit bottom; *4* – drying height bottom; *5* – pebble beach under study; *6* – beach scarp

(according to the scale factor of time) and amplitude (tide height), was selected by opening and closing the water inlet and outlet valves.

Experiments were performed for two sizes of beach-forming material with median diameters $d_{50\%}$ = 0.74 mm (22.2 mm) and $d_{50\%}$ = 1.19 mm (35.7 mm). For these sediment sizes under the selected wave mode in natural conditions, profiles of relative dynamic equilibrium were calculated, according to which, taking into account the compaction of sediments during wave processing, the construction profiles of the initial backfill were determined (Fig. 3). Based on the geometric scale, the construction profile of the original backfill was reproduced on the model and remained unchanged for the corresponding size of the beach-forming material during the experiments (Fig. 4).

Results of studies and their discussion

In the first series of experiments, studies in a wave flume were carried out with a beach-forming material with a particle size of $d_{50\%}$ = 0.74 mm (22.2 mm). First, with the water level unchanged during the experiment and corresponding to its maximum mark during the high tide phase, the profile of a pebble beach was formed under the influence of waves on the initial backfill of beach-forming material near the beach scarp (Fig. 5, Profile *2*). The profiles formed during tidal cycles were compared with this profile in further studies.

In the course of the experiment, at a constant water level in the flume, under the influence of waves breaking on the initial backfill of the beach-forming material, a shift of sediments to the breakdown area was observed with the formation of a beach profile with a steep underwater part, which is typical for natural pebble beaches [8]. At the end of the experiment, the surface beach was 24.0 cm (7.2 m) wide, and there was no storm bar in its upper part.

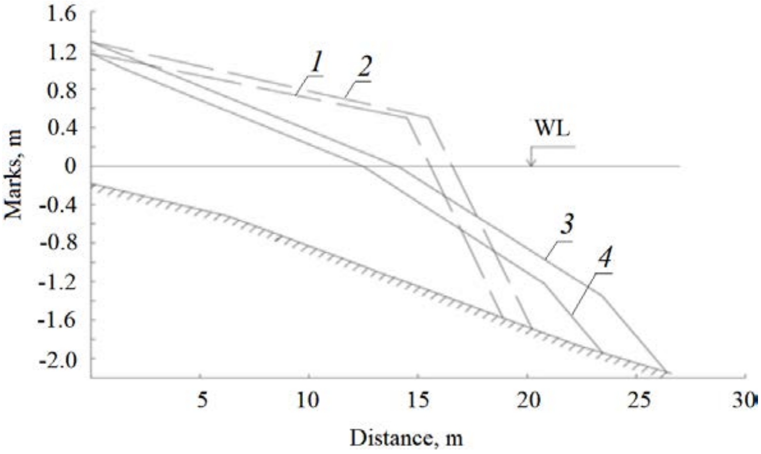

F i g . 3 . Calculated profiles of the relative dynamic equilibrium of wave-absorbing pebble beaches and construction profiles of the initial backfilling of beach-forming material: *1* – construction profile for $d_{50\%}$ = 0.022 м; *2* – construction profile for $d_{50\%}$ = 0.036 м; *3* – relative dynamic equilibrium profile for $d_{50\%}$ = 0.022 м; *4* – relative dynamic equilibrium profile for $d_{50\%}$ = 0.036 м. WL – water level

F i g . 4 . Model of the initial backfill of the beach-forming material. The horizontal line shows the water level at high tide

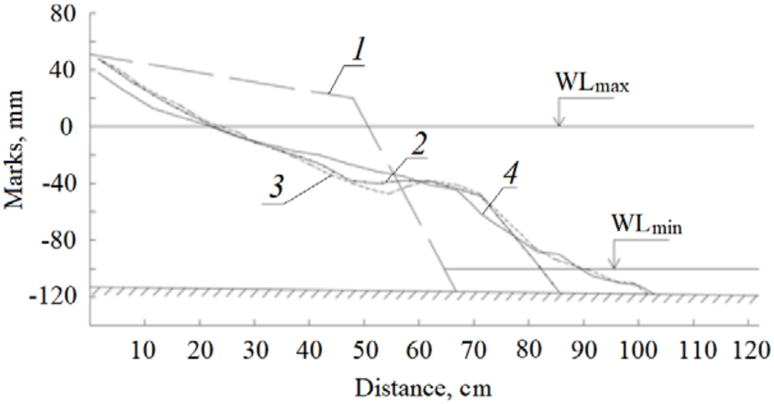

F i g . 5 . Deformation of the beach profile, composed of sediments with a size of $d_{50\%}$ = 0.74 mm, worked out at the constant maximum level during the tidal cycle; *1* – profile of the initial backfill; *2* – profile developed at the constant maximum water level; *3* – profile developed during the low tide phase; *4* – profile developed during the high tide phase

In the next experiment, with a continuous decrease in the water level in a flume simulating the low tide phase, under the influence of waves on the profile formed at the maximum water level, the beach material was displaced down the slope seaward of the bottom of the beach worked out at the maximum level. As a result of this displacement, a more gentle profile of the underwater part of the pebble beach was formed. At the same time, an insignificant part of the sediments was moved to the upper part of the profile, where an increase in the beach marks was recorded. The total protrusion of the underwater beach boundary relative to the profile developed at the constant maximum water level made 16.1 cm (4.83 m). In contrast to the previous experiment, when the water level decreased (low tide phase), swells were formed in the underwater part of the beach. With continuous decrease in the water level, the upper part of the profile developed at the constant maximum level changed little (Fig. 5, Profile *3*).

In the subsequent experiment reconstructing the conditions of the high tide, when the waves act on the profile worked out at low tide (Fig. 5, Profile *3*), no erosion of its underwater part protruded at low tide and displacement of the underwater boundary of the beach towards the shore were observed (Fig. 5, Profile *4*). Beach material that was pushed down at low tide was not placed back at high tide. During the experiment, under conditions of the increase of water levels, the formation of above-water swells at intermediate water levels was observed, which were washed away with further increase in the level. At the end of the experiment, with the increase in the water level (at high tide), an increase in the profile marks of the pebble beach was recorded seaward of the shore (Fig. 5, Profile *4*). At the same time, there was a decrease in the elevations of the surface part of the beach formed during the simulation of low tide, due to the displacement of sediments into the underwater part of the profile. The processes occurring on the pebble beach at high tide led to some smoothing of the beach profile.

During one tidal cycle, the width of the surface part of the beach, worked out at the constant maximum level, changed insignificantly: 22.4 cm (6.7 m) at the constant maximum level, 24.0 cm (7.2 m) at low tide, and 22.0 cm (6.6 m) at high tide. At low tide, the underwater boundary, compared to the pebble beach worked out at the maximum level unchanged during the experiment, moved out into the sea by 16.1 cm (4.83 m).

As follows from the experiments, the tidal factor affects the formation of the profile of a pebble beach, as a result of which it differs from the profile developed by waves in the initial backfill of beach-forming material at the constant maximum level. At low tide, the surface part of the beach is washed out and the beach material is displaced into its underwater part, which leads to the protrusion of the underwater beach boundary towards the sea. At high tide, material that was displaced at low tide does not return to the top of the profile. The underwater part of the beach profile formed during the tidal cycle turned out to be flatter than the profile at the constant maximum water level. The height of the upper surface part of the beach, developed at high tide, turned out to be less than on the profile at low tide.

In general, further experiments concerning the impact of waves directly on the initial backfill of beach-forming material with $d_{50\%}$ = 0.74 mm at different combinations of high and low tide phases proved the results obtained above on the description of their impact on the formation of a beach profile composed of large rock fragments.

Under the influence of waves on the initial backfill of the beach-forming material, in combination with a continuous water level rise (high tide), the beach material shifted towards the sea, as a result of which the underwater boundary of the formed beach moved forward compared to the position of the original backfill by 19.5 cm (5.85 m). The beach profile developed by the action of waves on the initial backfill of beach-forming material at high tide (Fig. 6, Profile *2*) differed little from the profile obtained at the constant maximum level (Fig. 5, Profile *2*).

Under the influence of waves at low tide on the profile of the beach formed from the material of the initial backfill at high tide (Fig. 6, Profile *2*), as in previous experiments, the bottom (underwater boundary) of the pebble beach moved forward by 12.0 cm (3.6 m) (Fig. 6, Profile *3*), while the width of the surface part of the beach decreased from 25.5 (7.65 m) to 24.0 cm (7.20 m). These results are close to the previously obtained data.

Fig. 7 shows the beach profiles formed as a result of repeated wave impact on the initial backfill of the beach-forming material. Figure 8 shows the averaged profiles

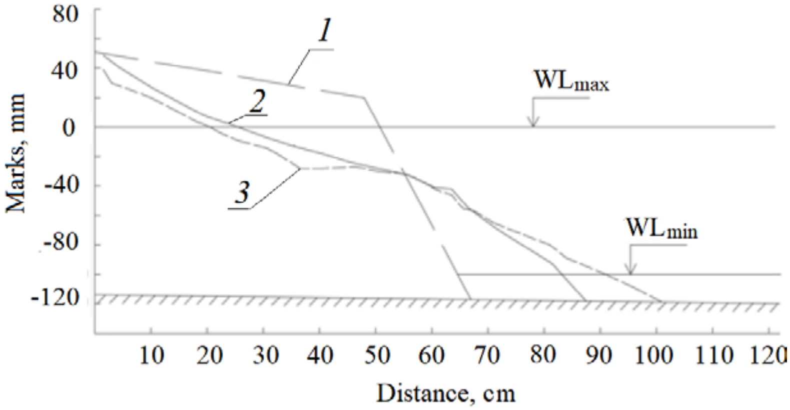

Fig. 6. Beach profiles formed during the high tide phase under the action of waves on the initial backfill of beach-forming material with a particle size of $d_{50\%}$ = 0.74 mm (22.2 mm): *1* – profile of the initial backfill; *2* – beach profile developed in the initial backfill of beach-forming material during the high tide phase; *3* – beach profile formed in the low tide phase under the influence of waves on the profile developed at high tide

generated by waves at low tide when they act on a profile formed from the material of the original backfill at high tide (Fig. 6, Profile *2*) and when they act on the original backfill (construction profile) (Fig. 7) of the beach-forming material with a particle size of $d_{50\%}$ = 0.74 mm (22.2 mm). As follows from the results obtained, the warping-off of large rock beach material under different initial conditions of the experiments took place to the same depth.

The second series of experiments were devoted to the influence of the tidal cycle on the formation of the profile of a wave-absorbing pebble beach composed of sediments with a particle size of $d_{50\%}$ = 1.19 mm (35.7 mm). The wave parameters remained the same as in the previous series of experiments with the beach-forming material with a particle size of $d_{50\%}$ = 0.74 mm (22.2 mm): wave height – 5.3 cm (1.60 m), period – 1.1 s (6.0 s). Beach profiles worked out by waves in combination with tidal level fluctuations were compared with the profile formed when waves acted on the initial backfill of beach-forming material with a particle size of $d_{50\%}$ = 1.19 mm (35.7 mm) (see Fig. 3) at the constant maximum water level in the high tide phase (Fig. 9). This profile is shown in Fig. 10 (Profile *2*).

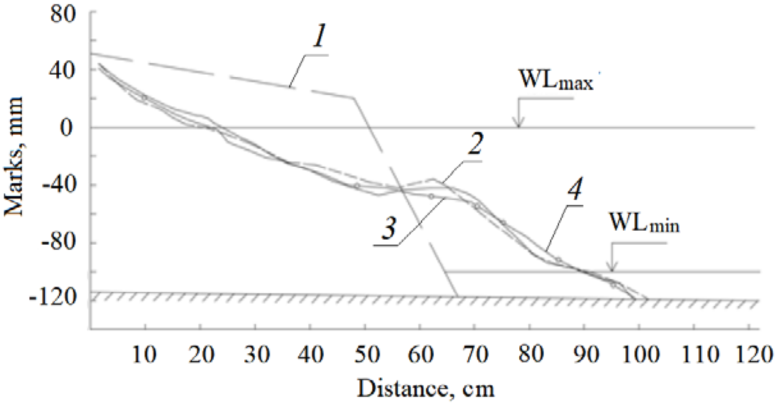

Fig. 7. Beach profiles formed in the low tide phase under the action of waves on the initial filling of material with a particle size of $d_{50\%}$ = 0.74 mm (22.2 mm): *1* – profile of the initial backfill; *2–4* – beach profiles formed in the low tide phase under the influence of waves on the initial backfill of material with a particle size of $d_{50\%}$ = 0.74 mm (22.2 mm)

With the water level in the flume unchanged during the experiment, under the influence of waves, the breakdown of which occurred on the underwater continuation of the initial backfill of the beach-forming material, the model showed a displacement of the beach material from its surface to the underwater part. In the zone of wave breaking, a beach profile with a steep slope was formed. In contrast to the beach, which was composed of finer material (see Fig. 5), its surface part ended in a storm bar. The bottom of the formed beach moved out into the sea by 11.7 cm (3.51 m) compared to the underwater boundary of the original backfill. In the previous series of experiments with finer beach-forming material, this protrusion made 16.1 cm (5.43 m). The width of the surface part of the beach, composed of coarser material, made 23.6 cm (7.05 m), which exceeded the similar width for sediments of smaller size (22.4 cm). This does not contradict the general ideas concerning the influence of beach material size on the formation of the profile of a pebble beach and indicates the correct reflection of the processes occurring in the coastal zone on the model.

Further experiments, as previous series, aimed at the study of reconfiguration of the beach profile composed of sediments with a particle size of $d_{50\%}$ = 1.19 mm (35.7 mm) and worked out by the initial wave at the constant water level with successive alteration of low tide and high tide phases.

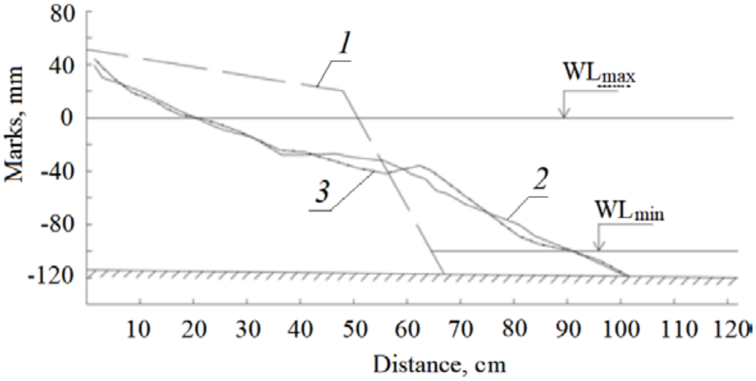

F i g . 8 . Beach profiles worked out in the low tide phase under the influence of waves on the profile formed at high tide and under their influence on the initial backfilling of the beach-forming material with a particle size of $d_{50\%}$ = 0.74 mm (22.2mm): *1* – profile of the initial backfill; *2* – profile developed at low tide when the waves act on the profile formed at high tide; *3* – profile formed at low tide under the influence of waves on the initial backfill of beach-forming material

At low tide, as in the case of finer beach material, there was a reconstruction of the profile formed at the constant maximum water level, and the warping-off of sediments to a depth. The bottom of the pebble beach at low tide under the influence of waves moved out into the sea by 13.5 cm (4.05 m) compared with the initial profile. At the same time, the width of the surface part of the beach increased by 6.0 cm (1.80 m) as a result of sediment movement not only downward, but also upward along the profile. An increase in the width of the surface part of the beach was noted with finer material also. As can be seen from Fig. 10 (Profile *3*), at low tide, a series of accumulation swells formed on the surface of the underwater part of the beach, but not as pronounced as with smaller sediments. The same swells, in contrast to the beach composed of smaller sediments, were also formed in the surface part of the beach.

In the next experiment, the conditions of the high tide are reconstructed, as a result of which, under the influence of waves on the profile developed at low tide, erosion of the surface part of the beach was observed with a decrease in its height and accumulation of sediments with the formation of an underwater swell in the wave breaking area. At the same time, as can be seen from Fig. 10 (Profile *4*), the position of the underwater boundary of the pebble beach, worked out by the waves at low tide, remained unchanged.

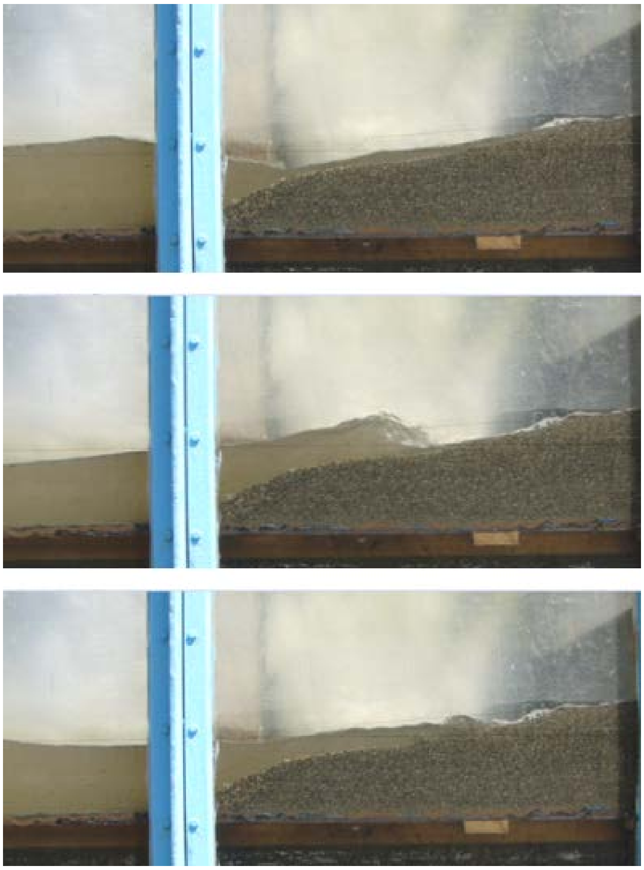

Fig. 9. Impact of waves on the initial backfill of beach-forming material with a size of $d_{50\%}$ = 1.19 mm (35.7 mm) at the constant maximum level

Comparison of data on the formation of profiles of pebble beaches, composed of sediments with a particle size of $d_{50\%}$ = 0.74 mm (22.2 mm) and $d_{50\%}$ = 1.19 mm (35.6 mm), indicates that at low tide the beach material, regardless of its size, shifts towards the sea compared to a profile generated at the constant maximum water level. For fine material, this displacement made 16.2 cm (4.86 m), and for coarse material, it was 14.3 cm (4.29 m), due to the greater mobility of fine material. Comparison of the beach profiles presented in Fig. 5 and Fig. 10 shows that with coarse beach material a steeper underwater part of the profile is formed at low tide. In the middle underwater part of the profile, with coarse material, in contrast to fine material, during high tide, due to erosion of the surface part of the beach, accumulation forms are formed, which leads to the formation of a profile of a complex shape at low tide. With fine material at high tide, beach profile smoothing is noted.

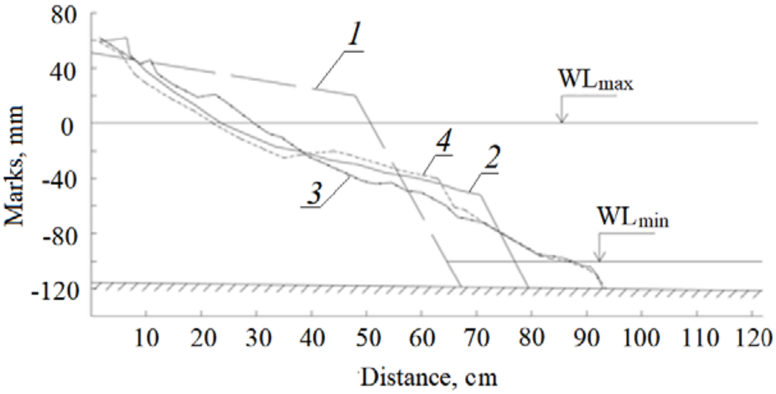

Fig. 10. Deformation of the beach profile composed of sediments with a size of $d_{50\%}$ = 1.19 mm (35.7 mm), worked out at the constant maximum level during the tidal cycle. *1* – profile of the initial backfill; *2* – profile developed at the constant maximum water level; *3* – profile developed during the ebb phase when waves act on the profile formed at the constant maximum water level; *4* – profile developed during the high tide phase, when the waves act on the profile formed at low tide

Apparently, this is explained by the coarseness of the beach-forming material, when, under the same wave conditions, the moving effect for large sediments decreases compared with small ones.

In further experiments, as with finer material, beach profiles were formed with waves acting directly on the initial backfill of beach-forming material with $d_{50\%}$ = 1.19 mm (35.7 mm), with different combinations of high and low tide phases. The experiments carried out confirmed the data obtained earlier with fine material on the influence of the alternation of tidal phases on the formation of the profile of a wave-absorbing pebble beach composed of large rock fragments.

Conclusion

On the basis of experiments performed in a wave tray, a difference was revealed in the profiles of pebble beaches formed on tideless and tidal seas under the influence of waves. On tidal seas, in comparison with tideless seas, during the formation of the profile of a wave-absorbing pebble beach at low tide, the beach-forming material is pulled to depths greater than in tideless ones. At high tide, this material does not fully return to the upper part of the profile of the wave-absorbing pebble beach. The irretrievable displacement during low tide of a part of the volume of the beach-forming material beyond the calculated profile of relative dynamic equilibrium, calculated for the conditions of tideless seas, leads to a decrease in the width of the wave-absorbing pebble beach and a decrease in its wave-damping properties. When creating wave-absorbing pebble beaches on tidal seas and calculating the initial backfill of beach-forming material, it is necessary to take into account the volume of irretrievable displacement of large rock sediments to the lower part of the formed profile during low tide.

According to the studies, the volume of beach-forming material that is displaced at low tide to a depth and not returned back at high tide makes about 5 %.

REFERENCES

1. Drobotko, S.Yu. and Petrov, V.A., 2011. To the Calculation of Artificial Wave-Absorbing Pebble Beach. *European Researcher*, (5-1), pp. 601–604 (in Russian).
2. Levi, I.I., 1967. [*Modelling of Hydraulic Phenomena*]. Leningrad: Energiya, 236 p. (in Russian).
3. Daily, J.W. and Harleman, D.R.F., 1966. *Fluid Dynamics*. Addison-Wesley Publishing Company, 454 p.
4. Kononkova, G.E. and Pokazeev, K.V., 1985. [*Dynamics of Sea Waves*]. Moscow: Izd-vo MGU, 298 p. (in Russian).
5. Lighthill, J., 1981. *Waves in Fluids*. Cambrige: Cambrige University Press, 504 p.
6. Petrov, V.A. and Shakhin, V.M., 1990. [Hydraulic Modelling of Pebble Beach Dynamics]. In: TSNIIS, 1990. [*Improvement of Coastal Protection Methods*]. Moscow: TSNIIS, pp. 49–58 (in Russian).
7. Lappo, D.D., Strekalov, S.S. and Zavialov, V.K., 1990. [*Loads and Effect of Wind Waves on Hydrotechnical Structures*]. Leningrad: VNIIG im. B.E. Vedeneeva, 432 p. (in Russian).
8. Peshkov, V.M., 2005. [*Pebble Beaches of Tideless Seas. Main Problems of Theory and Practice*]. Krasnodar, 444 p. (in Russian).

Submitted 5.04.2022; accepted after review 26.04.2022;
revised 6.07.2022; published 26.09.2022

About the authors:

Viktor A. Petrov, Senior Research Associate, Branch of JSC TsNIITS “Research Center “Sea Coasts” (1 Iana Fabritsiusa St., Sochi, 1354002, Russian Federation), Ph.D. (Geogr.), **Author ID 71251**, *demmi8@mail.ru*

Galina V. Tlyavlina, Head of the Laboratory of Modeling, Calculations and Rationing in Hydraulic Engineering, Branch of JSC TsNIITS “Research Center “Sea Coasts” (1 Iana Fabritsiusa St., Sochi, 1354002, Russian Federation), **ORCID ID: 0000-0003-4083-9014**, **Author ID: 604630**, **SPIN-code: 5516-9241**, *TlyavlinaGV@Tsniis.com*

Nestifor A. Yaroslavtsev, Leading Research Associate, Branch of JSC TsNIITS “Research Center “Sea Coasts” (1 Iana Fabritsiusa St., Sochi, 1354002, Russian Federation), Ph.D. (Tech.)

Contribution of the authors:

Viktor A. Petrov – preparation of data for modeling, conducting experiments in a wave flume, processing and analysis of the results, preparation of the text of the article

Galina V. Tlyavlina – development of a modeling technique in a wave flume, analysis of the results obtained, preparation of graphic materials

Nestifor A. Yaroslavtsev – development of the modeling technique, conducting experiments in a wave flume, analysis of the results obtained, preparation of the text of the article and list of references

All the authors have read and approved the final manuscript.

DOI: 10.22449/2413-5577-2022-3-71-92

Comparative Analysis of Nitrogen and Phosphorus Assimilation Rates by Macroalgae and Seagrasses according to Simulation Data

E. F. Vasechkina *, I. P. Naumenko, T. A. Filippova

Marine Hydrophysical Institute of RAS, Sevastopol, Russia
vasechkina.elena@gmail.com

Abstract

The paper considers assimilation and release of nitrogen and phosphorus compounds by sea macroalgae and grasses during primary production synthesis in a coastal euphotic zone. To reproduce the processes of aquatic plant functioning under competition for resources among themselves and phytoplankton, a mixed type benthic phytocenosis simulation model was used. The object-oriented concept of the model allows reproducing random spatial distribution of plant species in the computational domain. Plant biomass dynamics is calculated using an individual-based approach. The rates of physiological processes depend on temperature, light, nutrient concentrations in water and soil as well as the content of these elements in plant tissues. The empirical coefficients of the model are based on published data from laboratory experiments. Quantitative estimates of the efficiency of nutrient accumulation in the tissues of various plant groups were obtained. It is shown that brown and red macroalgae having coarser thallus structure as well as sea grasses have the highest bioremediation potential. For the coastal zone of Crimea these are species of cystoseira, phyllophora and seagrass zostera. Benthic phytocenoses, where these species predominate, support the health of coastal marine ecosystems under increased anthropogenic pressure.

Keywords: benthic phytocenosis, phytocenosis, bioremediation, object-oriented modelling, primary production

Acknowledgements: the work was performed under state assignment of FSBSI FRC MHI on topic no. 0555-2021-0005 “Complex interdisciplinary research of oceanologic processes, which determine functioning and evolution of the Black and Azov Sea coastal ecosystems”.

For citation: Vasechkina, E.F., Naumenko, I.P. and Filippova, T.A., 2022. Comparative Analysis of Nitrogen and Phosphorus Assimilation Rates by Macroalgae and Seagrasses according to Simulation Data. *Ecological Safety of Coastal and Shelf Zones of Sea*, (3), pp. 71–92. doi:10.22449/2413-5577-2022-3-71-92

Сравнительный анализ скоростей ассимиляции азота и фосфора макроводорослями и морскими травами по данным имитационного моделирования

Е. Ф. Васечкина *, И. П. Науменко, Т. А. Филиппова

Морской гидрофизический институт РАН, Севастополь, Россия
**e-mail: vasechkina.elena@gmail.com*

Аннотация

Рассматриваются ассимиляция и выделение соединений азота и фосфора морскими макроводорослями и травами в процессе синтеза первичной продукции в прибрежной эвфотической зоне. Имитационная модель донного фитоценоза смешанного типа использована для воспроизведения процессов функционирования водных растений в условиях конкуренции за ресурсы между ними и с фитопланктоном. Объектно-ориентированная концепция модели позволяет воспроизвести в расчетной области произвольное пространственное распределение видов растений. Динамика биомассы растений рассчитывается с использованием индивидуум-ориентированного подхода. Скорости протекания физиологических процессов зависят от температуры, освещенности, концентрации биогенных элементов в воде и грунте, а также уровня накопления этих элементов в тканях растения. Эмпирические коэффициенты модели базируются на опубликованных данных лабораторных экспериментов. Получены количественные оценки эффективности накопления биогенных элементов в тканях различных групп растений. Показано, что наибольшим потенциалом биоремедиации обладают бурые и красные макроводоросли, имеющие более грубое строение талломов, а также морские травы. Для прибрежной зоны Крыма это виды цистозиры, филлофоры и морская трава зостера. Донные фитоценозы, в которых эти виды доминируют, поддерживают здоровье морских экосистем прибрежной зоны в условиях повышенной антропогенной нагрузки.

Ключевые слова: донный фитоценоз, фитоценоз, биоремедиация, объектно-ориентированное моделирование, первичная продукция

Благодарности: работа выполнена в рамках госзадания ФГБУН ФИЦ МГИ по теме № 0555-2021-0005 «Комплексные междисциплинарные исследования океанологических процессов, определяющих функционирование и эволюцию экосистем прибрежных зон Черного и Азовского морей».

Для цитирования: *Васечкина Е. Ф., Науменко И. П., Филиппова Т. А.* Сравнительный анализ скоростей ассимиляции азота и фосфора макроводорослями и морскими травами по данным имитационного моделирования // Экологическая безопасность прибрежной и шельфовой зон моря. 2022. № 3. С. 71–92. doi:10.22449/2413-5577-2022-3-71-92

Introduction

Macrophytobenthos has a decisive influence on the biochemical state of coastal waters. Benthic macroalgae and seagrasses compete with phytoplankton for inorganic resources, being a significantly better reservoir for the accumulation of carbon and other biogenic elements [1]. Phytobenthos, in contrast to phytoplankton, is characterized by high levels of biomass and a turnover time of about a year, comparable to terrestrial photosynthetic systems. For phytoplankton, the turnover time is of about a week. Thus, estuaries, bays, shallow coastal areas of the seas play an important role in the processes of the global carbon cycle.

According to the authors of [2], in the 1990s the net primary production of macroalgae and seagrasses growing in the shallow euphotic zone was approximately $3 \cdot 10^9$ t·year^{-1}, at least 10 % of all primary production produced in the World Ocean. The area of the coastal zone under consideration, corresponding to the width of the algae growth band down to depths of 50 m, was estimated at 1.9 % of the area of the World Ocean [2]. In relation to the annual volumes of carbon emissions into the atmosphere as a result of fuel combustion (~ $5.4 \cdot 10^9$ tC·year^{-1} in 1990), the primary production of macroalgae and seagrasses was 55 %. In specific terms, the primary production of macrophytobenthos in the coastal zone exceeded the production of phytoplankton by an order of magnitude, varying within 500–2000 gC·m^{-2}·year^{-1} against 50–300 gC·m^{-2}·year^{-1}.

As is known, in recent decades, the coastal areas of the seas have experienced an unprecedented anthropogenic impact, which often results in their eutrophication with the development of negative phenomena, one of which is degradation of benthic phytocenoses. The main reasons are: a decrease in water transparency, as a result of which the width of the band of benthic vegetation decreases; and wastewater emissions with a high content of nutrients, leading to structural changes in the phytocenosis. Degradation and reduction of areas occupied by benthic vegetation is an extremely negative phenomenon, since it is benthic plants that prevent the development of hypoxia and deaths in shallow water during periods of summer stagnation. A number of studies record these negative phenomena in different areas of the World Ocean and the Black Sea in particular [3, 4].

According to modern estimates [5, 6], the average net primary production of macroalgae has noticeably decreased and varies within 91–738 gC·m^{-2}·year^{-1}. The growth band width of macroalgae and seagrasses has decreased as a result of raising the lower boundary of benthic vegetation distribution. For a rough estimate, it can be taken as no more than 1 % of the width of the shelf of the World Ocean, which corresponds to the thickness of the photosynthesis zone near the coast (25–30 m). Accordingly, the net primary production of macroalgae and seagrasses can be estimated at $1.5 \cdot 10^9$ tC·year^{-1}, which amounts to 18 % of the total carbon emissions into the atmosphere in 2020 (against 55 % in 1990).

In the Black Sea, a noticeable decrease in the photosynthesis zone has been recorded in recent decades. The lower boundary of macroalgae distribution on the North Caucasian and Crimean coasts runs at a depth of 10–15 m, in rare cases up to 20 m. According to the authors of the work 1), over the past 30 years, macrophyte biomass has decreased almost tenfold on the coast of the North Caucasus.

---

1) Oguz, T., ed., 2008. *State of the Environment of the Black Sea (2001-2006/7)*. Istanbul, Turkey : BSC, 448 p. Available at: http://blacksea-commission.org/Downloads/SOE27032009-1_compressed.pdf [Accessed: 04 September 2022].

The width of the *Cystoseira* growth belt decreased from 1.5 km to 300–500 m. The structure of benthic phytocenoses changed significantly. The biomass of *Cystoseira* and *Phyllophora* (dominants of the corresponding benthic phytocenoses) noticeably decreased, while the biomass of associated algae and epiphytes increased, among which green algae predominate. Such changes are characteristic of a situation of excessive anthropogenic load, when native vegetation is replaced by associations of unproductive species, representatives of the genera *Ulva*, *Cladophora*, *Polysiphonia*, and others, and spatial and hierarchical structure of the community is simplified [7]. Regular blooms of seawater, caused by massive development of green algae, on the beaches of Anapa is a natural consequence of such changes [8].

It was shown in [9] that the diversity of green algae is currently increasing in the coastal zone of the Black Sea. At the same time, it is typical that "mesosaprobic communities of macroalgae displace oligosaprobic ones and become dominant almost throughout the entire length of the Russian coast, including open areas" [9, p. 29].

Restoration of destroyed benthic phytocenoses is a complex task that requires a long time and significant financial costs. The following are the known methods of such reconstruction:

- use of aquaculture of macroalgae and molluscs to reduce the concentration of biogenic elements in water, to reduce the concentration of suspended organic matter and, accordingly, to increase water transparency [10, 11];
- creation of artificial reefs inhabited by filter-feeding mollusks and macroalgae to improve water quality in the near bottom layer [12–14];
- reconstruction of seagrass fields by implanting rather large areas of benthic vegetation with its subsequent rooting (for an analysis of modern methods of such reconstruction, see 2)).

In this regard, modeling studies of the dynamics of processes occurring in benthic phytocenoses, studying the response of the macroalgae and seagrass community to abrupt changes in environmental conditions, and elucidating specific reactions of various components of phytocenoses to these changes are relevant. In a practical sense, it is useful to assess the potential efficiency of the use of various macroalgae for the purpose of biological treatment of coastal waters with an excess supply of biogenic elements with wastewater.

In [15], using a two-layer model of the ecosystem of a semi-enclosed reservoir, the dynamics of dissolved oxygen concentration in the upper mixed and near-bottom layers was analyzed as a response to the release of wastewater with a high concentration of biogenic compounds; the contribution of individual genera of micro- and macroalgae to the process of self-purification of the reservoir was evaluated. This work is a continuation and development of this study, in which we are going to consider the processes of self-purification of a reservoir by analyzing the rates

---

2) Clark, D. and Berthelsen, A., 2021. *Review of the Potential for Low Impact Seagrass Restoration in Aotearoa New Zealand*. Nelson, New Zealand, 55 p. Available at: https://envirolink.govt.nz/assets/2146-NLCC119-Review-of-the-potential-for-low-impact-seagrass-restoration-in-Aotearoa-New-Zealand.pdf [Accessed: 04 September 2022].

of accumulation of nitrogen and phosphorus compounds in plant tissues. The paper uses an extended version of the model, which includes a procedure for calculating the dynamics of seagrass biomass. A semi-enclosed reservoir is considered, the bottom of which is composed of stony-sandy soils. For rocky soil, we are going to consider the *Cystoseira* phytocenosis as the main component in terms of biomass, for sandy soils – the *Zostera* phytocenosis.

Materials and methods

The object-oriented model of the ecosystem of a semi-enclosed reservoir, including phytoplankton and phytobenthos, is described in detail in [15, 16], therefore, we are not going to dwell on this model in detail here. An addition to it is a block describing the dynamics of seagrass biomass. In the coastal zone of Crimea, areas with rocky and sandy bottoms alternate, so a complete ecological model must include blocks for both types of benthic phytocenosis. The object-oriented approach to building the model makes it possible to use different blocks in different parts of the computational domain and to flexibly switch the model from one mode to another. To do this, it is only necessary to have data on the nature of phytocenosis in a particular section of the bottom, which must be specified in the model as control variables. For shallow-water areas of the coast, it is possible to remotely determine the type of dominant species in a particular area of the bottom and an approximate determination of the composition of associated algae and epiphytes characteristic of this phytocenosis. The mapping of benthic vegetation of the Kruglaya Bay was carried out, for example, in [17]. Using these data, it is possible to set the spatial distribution of model objects corresponding to the main species growing on each particular section of the bottom.

The main differences between the two types of benthic phytocenoses are that seagrasses grow on the sandy bottom, while macroalgae phytocenosis is characteristic of the rocky bottom. The associated seagrass species may be algae, so the model must be flexible enough to reflect the observed vegetation biodiversity in the coastal zone. Such flexibility is provided in the model by specifying the field of benthic vegetation in the form of a set of objects with different characteristics and describing the growth of different types of algae and seagrasses. As an example, let us present the composition of benthic vegetation of the Kruglaya Bay, according to [17], where the following plant complexes were recorded:

- Cystoseira species (*C. crinita* and *C. barbata*) on block-boulder substrate and bedrock exposures;
- *Phylophora cripsa* on gravel-sand deposits with broken shells;
- community of seagrasses: *Zostera noltei*, *Stuckenia pectinata*, and *Ruppia* species on silt-sand deposits;

– community of seagrasses and green algae, represented mainly by *Cladophora* species on muddy sediments.

For the modeler, the main difference between algae and grasses is that grasses have roots that provide additional nutrients to their tissues, unlike algae, which extract the necessary nutrients directly from sea water. This entails the need for a mathematical description of this additional flow with the corresponding characteristics of the consumption rate and its dependence on the internal state of the tissues and concentration of nutrients in the soil. Accordingly, it is required to introduce two new classes into the previously developed object-oriented model – "Seagrasses" and "Seagrass species". Fig. 1 shows a block diagram of the biological block of the ecosystem model, which includes classes of both macroalgae and seagrasses.

The components of the bottom phytocenosis compete for light and mineral resources. Nitrogen and phosphorus circulate in the system, passing through the turnover from inorganic forms through plant tissues (phytoplankton, macroalgae, seagrasses), particulate (POM) and dissolved (DOM) organic matter and returning to the inorganic form. Hydrodynamic factors also have a significant effect

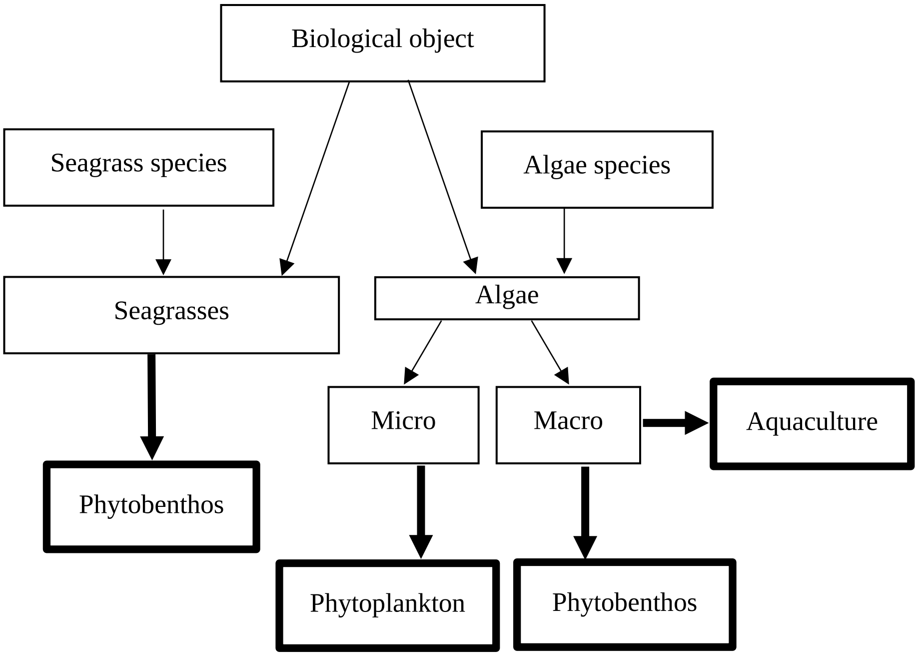

Fig. 1. Diagram of classes and relationships between them in the biological block of the object-oriented simulation model for describing the mixed macroalgae and seagrasses phytocenosis dynamics

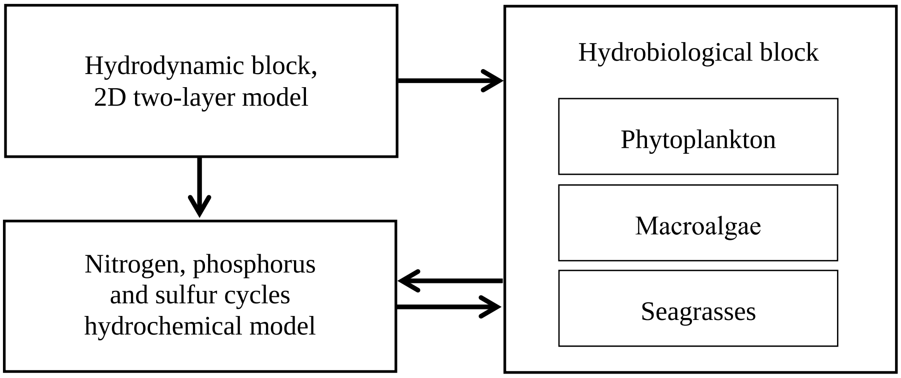

Fig. 2. Block diagram of the object-oriented model of a mixed-type benthic phytocenosis

on the rate of circulation of matter in the system. To account for all these processes, the biological model is coupled with hydrochemical and hydrodynamic blocks, as shown in Fig. 2.

Additional parameters in the class "Seagrass species" are the coefficients in the Michaelis-Menten formulas for calculating the rate of removal of inorganic forms of nitrogen and phosphorus from the soil. The main method of the new "Seagrasses" class is a seagrass growth model, which is largely similar to the previously developed algae growth model, but also contains significant differences. When developing it, the works [18, 19] have been used, which provide the necessary parametrizations based on the data of laboratory experiments.

Let us move on to the consideration of the developed mathematical model of seagrass growth. The extraction of mineral resources necessary for plant growth is carried out both through the roots and through the leaves directly from seawater. These fluxes can provide the plant with necessary substances in approximately equal proportions [20, 21]. The rhizosphere of a plant is usually characterized by reducing conditions, but the roots of the plant require oxygen, which the plant generates during photosynthesis and delivers to the roots. In the absence of light, the roots cannot absorb nutrients from the soil. Thus, the local illumination of the bottom area has a noticeable effect on the supply of plants with nitrogen and phosphorus.

As follows from the analysis of the energy balance of a plant cell and the equations of the growth model based on it, the rate of biogenic element uptake depends on the internal state of the tissues (intracellular reserves of the corresponding element), concentration of biogenic elements in water and soil, water temperature, and irradiance. In the process of vital activity, plant cells release DOM. The release rate in the model is proportional to the gross production in the process of photosynthesis in the light and the respiration rate in the dark, and the proportionality coefficient depends on the taxonomy of the plant. The model equations are based on these postulates and have the following form:

$$\frac{dB}{dt} = (\mu - E - m)B, \tag{1}$$

$$P_p = \left\{ P_{\max} \tanh\left(\alpha \frac{1}{P_{\max}} \right) - R_d \right\} f(T), \; I = I_0 e^{-\varepsilon h}, \tag{2}$$

$$\mu = P_p \min\left(f(Q_\mathrm{N}), f(Q_\mathrm{P}) \right), \tag{3}$$

$$f(Q_\mathrm{P}) = \frac{Q_\mathrm{P} - Q_\mathrm{P}^{\min}}{Q_\mathrm{P}^{\max} - Q_\mathrm{P}^{\min}}, \qquad f(Q_\mathrm{N}) = \frac{Q_\mathrm{N} - Q_\mathrm{N}^{\min}}{Q_\mathrm{N}^{\max} - Q_\mathrm{N}^{\min}}, \tag{4}$$

$$\begin{gathered} \frac{dQ_\mathrm{N}}{dt} = V_{\mathrm{NH}_4} \frac{[\mathrm{NH}_{4w}]}{K_{\mathrm{NH}_4} + [\mathrm{NH}_{4w}]} + V_{\mathrm{NO}_3} \frac{[\mathrm{NO}_{3w}]}{K_{\mathrm{NO}_3} + [\mathrm{NO}_{3w}]} + \\ + V_{r\mathrm{NH}_4} \frac{[\mathrm{NH}_{4b}]}{K_{r\mathrm{NH}_4} + [\mathrm{NH}_{4b}]} - \mu Q_\mathrm{N}, \end{gathered} \tag{5}$$

$$\frac{dQ_\mathrm{P}}{dt} = V_\mathrm{P} \frac{[\mathrm{P}]}{K_\mathrm{P} + [\mathrm{P}]} + V_{r\mathrm{PO}_4} \frac{[\mathrm{PO}_{4b}]}{K_{r\mathrm{PO}_4} + [\mathrm{PO}_{4b}]} - \mu Q_\mathrm{P}, \tag{6}$$

$$\begin{gathered} V_{\mathrm{NO}_3} = V_{\mathrm{NO}_3}^{\max}\left(1 - f(Q_\mathrm{N})\right), \qquad V_{\mathrm{NH}_4} = V_{\mathrm{NH}_4}^{\max}\left(1 - f(Q_\mathrm{N})\right), \\ V_\mathrm{P} = V_\mathrm{P}^{\max}\left(1 - f(Q_\mathrm{P})\right), \\ V_{r\mathrm{NH}_4} = V_{r\mathrm{NH}_4}^{\max}\left(1 - f(Q_\mathrm{N})\right), \qquad V_{r\mathrm{PO}_4} = V_{r\mathrm{PO}_4}^{\max}\left(1 - f(Q_\mathrm{P})\right). \end{gathered} \tag{7}$$

Here B is biomass of the object in units of dry weight, consisting of biomass of roots and leaves, g/m^3; μ is specific plant growth rate, 1/h; E is specific release rate of dissolved organic matter during the life of a plant, proportional to gross production, 1/h; m is mortality rate, 1/h; I is photosynthetically active radiation, μmol photons/(m^2·s); P_p is photosynthesis rate, mgO$_2$·g^{-1} DW·h^{-1}; $P_{\max}$ is maximum photosynthesis rate, mgO$_2$·g^{-1} DW·h^{-1}; α is slope of PI curve at low light outputs; R_d is respiration rate in the dark, mgO$_2$·g^{-1} DW·h^{-1}; ε is extinction coefficient depending on the concentration of phytoplankton and POM in the water; I_0 is irradiance on the water surface, depending on the time of day and season of the year; Q_P and Q_N are phosphorus and nitrogen concentrations in plant tissues, μmol·g^{-1}; $Q_\mathrm{P}^{\min}$, $Q_\mathrm{N}^{\min}$, $Q_\mathrm{P}^{\max}$ and $Q_\mathrm{N}^{\max}$ are minimum and maximum concentrations of phosphorus and nitrogen in plant tissues, μmol·g^{-1}; T is water temperature, ºC; $V_{\mathrm{NO}_3}^{\max}$, $V_{\mathrm{NH}_4}^{\max}$, $V_\mathrm{P}^{\max}$ are maximum possible uptake rates of nitrogen and phosphorus compounds at a sufficiently high concentration of biogenic element in water, μmol·g^{-1} DW·h^{-1}; K_P, K_{NO_3}, K_{NH_4} are half-saturation constants in the Michaelis-Menten ratios for describing the processes of assimilation of nitrogen and phosphorus compounds from seawater, μmol·l^{-1}; $V_{r\mathrm{NH}_4}^{\max}$, $V_{r\mathrm{PO}_4}^{\max}$ are maximum rates of ammonium and phosphate assimilation by plant roots; $K_{r\mathrm{NH}_4}$, $K_{r\mathrm{PO}_4}$ are half-saturation constants for this process; letter "w" denotes concentration of the corresponding compound in water, letter "b" – in soil.

It should be noted that all the "constants" of the model (maximum rates of physiological processes, half-saturation constants, etc.) are variables that depend on water temperature and irradiance. In the first approximation, they can be set as constant values based on the published data of laboratory experiments, however, for more accurate calculation results, additional studies are needed to find these dependences and formalize them for inclusion in the model.

Numerical experiments, results and discussion

The ecosystem model was used to study the processes of assimilation of nitrogen and phosphorus compounds by various species of macroalgae and seagrasses that are part of benthic phytocenosis. The task of planning and analyzing the results of simulation experiments was to establish differences in the efficiency of water purification from excess nutrients by different types of macroalgae and seagrasses. At the same time, all objects of benthic vegetation had to function in conditions of competition for resources, the main of which in this case is light.

The model also included three main groups of microalgae for the Black Sea: Diatoms, Dinoflagellates, and Coccolithophores, represented by species that have maximum abundance in the coastal waters of Crimea. Thus, phytobenthos and phytoplankton competed for mineral resources (nitrogen and phosphorus), in addition, phytoplankton, multiplying, increased water turbidity, which led to a decrease in illumination at the lower boundary of computational area, where phytobenthic objects were located.

Consuming inorganic components of nitrogen and phosphorus from seawater and accumulating them in their tissues, macrophytes purify seawater from excess nutrients, thereby slowing down the growth of phytoplankton and preventing formation of an excessively large amount of rapidly dying organic matter. However, situations are well known when eutrophication of a water body leads to rapid development of macroalgae rather than phytoplankton [8, 22]. More often these are green macroalgae (*Cladophora*, *Ulva*, *Enteromorpha*, etc.). Repeated mass development of macroalgae can lead to a change in the species composition of benthic phytocenosis. As a result of eutrophication, the dominant species of benthic vegetation is replaced: rapidly growing green macroalgae replaced the seagrasses. With a further increase in the volumes of biogenic substances entering the reservoir under the influence of other factors aggravating the situation, it is possible for macroalgae to be replaced by phytoplankton [23].

In the process of life, plant cells release DOM. According to estimates [24–27], from 50 to 70 % of the gross primary production is released into the environment in the form of DOM. Dissolved organics, the source of which is phytobenthos, can amount to 20 % of the total DOM in coastal areas and estuaries [28]. The mechanisms of DOM release for macroalgae and seagrasses are much less studied than for phytoplankton. It is believed that marine algae release DOM using the same mechanisms as microalgae, plus an additional significant amount of DOM is released through leakage during tissue fragmentation caused by dynamic processes [27]. There are active (exudation) and passive (diffusion) mechanisms of DOM release. The chemical composition of the released organic matter is important for assessing the amount of biogenic substances that enter the environment during macroalgae growth in the form of organic compounds. According to estimates [29], up to half of all particulate organic matter can be polysaccharides. In [26], based on the data of laboratory experiments, the elemental composition of DOM and POM released by different types of macroalgae is considered in detail. 11 species of macroalgae were studied: 4 red, 6 brown and 1 species of green algae, which stood out significantly from the group in terms of growth rate and other indicators. The average ratio C:N for DOM and POM was 4.46 ± 2.43 and 5.44 ± 0.75 respectively; ratio N:P for DOM and POM was recorded within 24.29 ± 18.00 and 20.00 ± 7.84 respectively. The experiments confirmed dependence of the DOM release rate on the growth rate, however, quantitative characteristics of such a dependence for different groups of algae were not given due to the small sample size.

When developing the model, we relied on the data of works by K. M. Khailov et al. [7, 24], who studied the intensity of organic matter release by algae growing in the coastal regions of the Crimea. Thus, according to the results of laboratory experiments, green algae have, on average, a lower percentage of lifetime release of dissolved organic matter – 23 % of gross production versus 38 % for red and 39 % for brown algae. The release of DOM by seagrasses, according to [25], was estimated as 10–15 % of the gross production. These estimates were used in the model to select the empirical parameters that govern the DOM release process.

POM during the growing season is usually released in a much smaller amount, but this is unfair for fast growing green algae with a fine structure [26]. Dead or defragmented algae tissues in the process of decomposition partially pass into DOM and POM. The destruction of thalli and their death in the model is parameterized using mortality rate, which is applied to the biomass of the algae. Since there are no subsequent links in the trophic chain in the model, this coefficient also takes into account the consumption of algae by marine hydrobionts. For fast growing green algae, it is about 0.002 (1/day), for slow growing brown and red algae it is 0.0001 (1/day). Model variables DOM, POM are taken into account in units of nitrogen (μmol N).

The growth dynamics is also significantly affected by the ability of algae to accumulate reserves of biogenic elements in order to maintain viability in conditions of deficiency of nutrients necessary for growth. This ability is numerically characterized by the possible maximum and minimum values of the intracellular content of the corresponding element. Having analyzed a number of works [30, 31], the intervals of variability of the intracellular content of nitrogen and phosphorus for red, brown and green macroalgae were established, and they are given in Table 1.

Table 1. Minimum ($Q_{\min}$) and maximum ($Q_{\max}$) nitrogen (N) and phosphorus (P) tissue content of different macroalgae groups (µmol·g^{-1} DW)

Macrophyte group	$Q^{\mathrm{N}}_{\min}$	$Q^{\mathrm{N}}_{\max}$	$Q^{\mathrm{P}}_{\min}$	$Q^{\mathrm{P}}_{\max}$
Macroalgae:				
brown	457	3711	15	113
red	853	3453	14	80
green	552	3789	15	96
Seagrasses	755	4507	30	119

To conduct research by analyzing the results of simulation experiments to assess the effectiveness of the nitrogen and phosphorus uptake from seawater, eight species of macroalgae growing on the rocky soil of the coastal zone of Crimea (*Cystoseira barbata, Ulva lactuca, Ceramium tenuicorne, Cladophora glomerata, Polysiphonia nigrescens, Gracilaria gracilis, Phyllophora truncata, Enteromorpha prolifera*), and two seagrass species dominating on sandy areas (*Zostera marina*, *Ruppia maritima*) were selected. The phytoplankton community included three groups of the most abundant microalgae in the area under consideration. The initial average concentrations of chemical and biological components of the ecosystem model, simulating conditions for the water outlet with high concentration of nitrogen compounds into the reservoir, are presented in Table 2. Fluctuations of concentrations in the computational grid nodes were set using a random number generator with a given dispersion and a mean. Irradiance changed during the model day along a sinusoid with zeroing of negative values corresponding to the night time. The light regime was 15 hours of light time and 9 hours of dark time.

At the initial moment, the nitrogen content in the algae tissues was 1000 µmol·g^{-1} DW, phosphorus – 40 µmol·g^{-1} DW. The simulation experiment lasted for one month of model time; during this period, the initially high concentration of biogenic elements significantly decreased due to their assimilation by aquatic plants (Fig. 3, *b*). Fluctuations in the concentration of nitrates and ammonium in the lower layer are associated with fluctuations in the thickness of the upper mixed layer (UML) caused by wind variability (Fig. 3, *a*). The rates of nitrogen and phosphorus assimilation, which were high at the beginning of the calculation, decreased as tissues became saturated, and the rates of photosynthesis and DOM release behaved accordingly (Fig. 4).

The average specific rates of physiological processes in the light and dark for the period of the most intensive growth of algae (the first 15 days of model time) were compared. Averaging was performed over the objects of each species of benthic algae and seagrasses separately. Daily average net production

Table 2. Initial mean values of the ecosystem model components in the experiments of the evaluation of nitrogen and phosphorus uptake efficiency

Model component	Unit of measurement	Initial value	
		upper layer	lower layer
[O_2]	mg/L	7	6
[DOM]	μmolN/L	1	1
[POM]	μmolN/L	1	1
[NO_3]	μmolN/L	50	50
[NH_4]	μmolN/L	10	10
[NO_2]	μmolN/L	1	1
[PO_4]	μmolP/L	2	2
Water temperature	°C	22	15
Mixed layer thickness	m	10	
Illumination at water surface	μmol photon/($m^2 \cdot s$)	0–800	
Testing area average plankton biomass	mg DW/m^3	110	
Testing area average phytobenthos biomass	g DW/m^2	360	

in oxygen units (*NetP*), respiration rate (*R*), specific rates of nitrogen (*N_up*) and phosphorus uptake (*P_up*), release of dissolved (DOM) and particulate (POM) organic matter, measured in units of nitrogen, were analyzed (Table 3).

The maximum specific rates of all physiological processes were observed for green algae (*Ulva, Enteromorpha*), the minimum ones were observed for *Phyllophora.* Several dependencies with significant coefficients of determination were found for the averaged rates. Linear dependences of nitrogen and phosphorus uptake rates on net production (*NetP*) were revealed, and the ratios differed

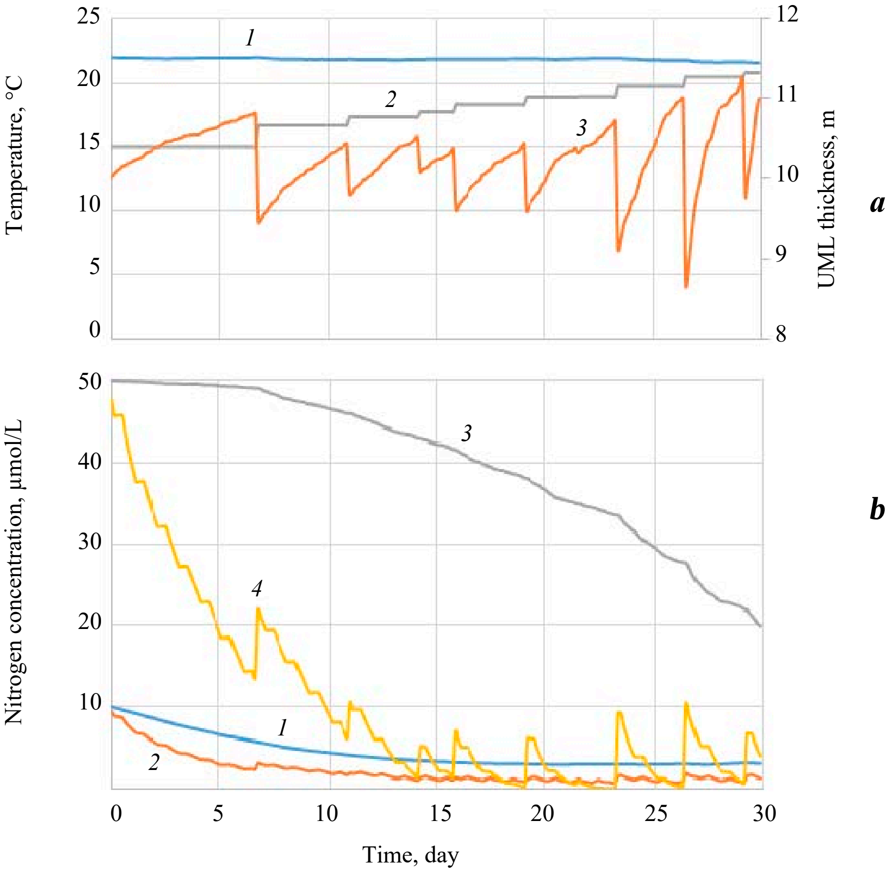

F i g . 3 . Model conditions for the phytocenosis functioning: *a* – water temperature of the upper (*1*) and lower (*2*) layers, upper mixed layer (UML) thickness (*3*); *b* – concentration of ammonium (*1*, *2*) and nitrates (*3*, *4*) in the upper (*1*, *3*) and lower (*2*, *4*) layers of the computational domain

significantly for macroalgae and grasses. Fig. 5 shows the found dependencies.

The flows of the main biogenic elements at the boundary between a biological object and the environment are interconnected with each other. A plant cell consumes inorganic and releases organic compounds containing carbon, nitrogen and phosphorus. Clear relationships are observed between the averaged specific rates of uptake and release (Fig. 6), established as a result of simulation experiments with different initial conditions. Thus, a significant dependence of the DOM release rate on the respiration of macroalgae and seagrasses was revealed (Fig. 6, *a*). The release rates of DOM and POM are related to the photosynthesis process intensity, which is confirmed by the dependence of these values on the rate of nitrogen assimilation (Fig. 6, *b*).

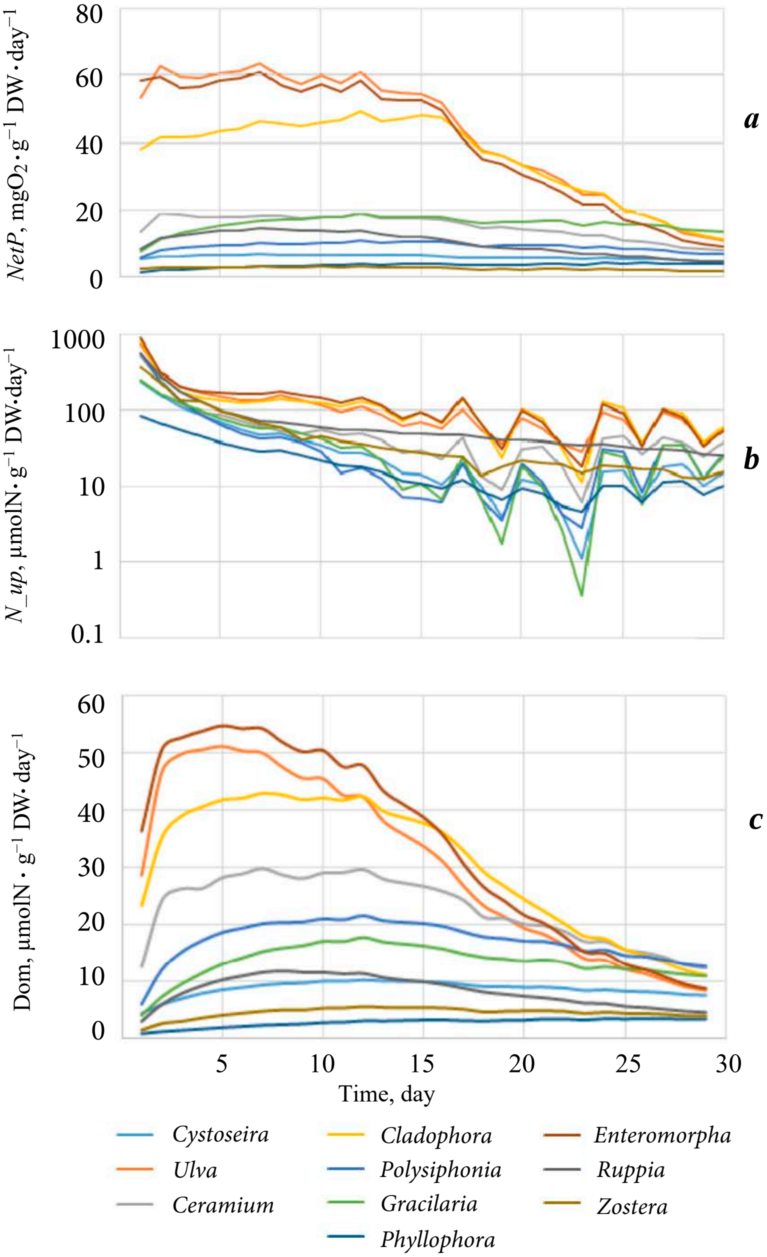

Fig. 4. Specific rates of the macroalgae and sea grasses physiological processes according to the model experiment data: primary production (*a*); nitrogen compounds assimilation (*b*); dissolved organic matter release (*c*)

Table 3. Averaged net production in the units of oxygen *NetP* (mg $O_2 \cdot g^{-1}$ $DW \cdot day^{-1}$), specific respiration rate *R* (mg $O_2 \cdot g^{-1}$ $DW \cdot day^{-1}$), nitrogen assimilation *N_up*, dissolved (Dom) and particulate (Pom) organic matter release rates (μmolN$\cdot g^{-1}$ $DW \cdot day^{-1}$), phosphorus assimilation (μmol P$\cdot g^{-1}$ $DW \cdot day^{-1}$) rate, relative characteristics of the efficiency of nutrients removal from the environment

Species	*NetP*	*R*	*N_up*	*P_up*	Dom	Pom	$\frac{N\_up}{Dom + Pom}$	$\frac{P\_up}{Dom + Pom}$
Cystoseira	3.89	0.86	40.24	1.29	5.28	1.44	6.00	0.19
Ulva	35.23	3.33	109.05	2.88	26.37	7.15	3.25	0.09
Ceramium	10.69	1.88	63.52	1.46	16.14	1.43	3.61	0.08
Cladophora	26.82	2.29	111.19	2.77	23.72	11.44	3.16	0.08
Polysiphonia	5.74	1.33	54.72	1.59	11.00	4.30	3.58	0.10
Gracilaria	9.53	0.62	44.16	1.36	8.37	1.43	4.50	0.14
Phyllophora	1.85	0.22	20.16	0.68	1.39	1.44	7.14	0.24
Enteromorpha	34.00	2.82	127.35	2.83	29.14	11.43	3.14	0.07
Ruppia	7.82	0.94	75.60	2.37	5.91	2.86	8.62	0.27
Zostera	1.78	0.83	57.76	1.60	2.66	2.87	10.46	0.29

Macroalgae and seagrasses cleanse the environment of excess nutrients by accumulating them in their tissues. At the same time, in the process of photosynthesis and production of organic matter, part of the assimilated compounds is released into the environment through various mechanisms (diffusion, exudation). The ratios of the rates of assimilation and release of nitrogen and phosphorus in the composition of organic matter (the last two columns of Table 3) can be considered as an assessment of the efficiency of removing excess nutrients during self-purification of a reservoir (bioremediation). It has been found that these indicators depend on the morphometric characteristics of macroalgae.

The fastest growing green algae with a fine structure are characterized by a significantly lower ability to remove nutrients from seawater than red and brown algae, which have a coarser structure. By introducing the specific surface index, which is often used in biology and defined as the ratio of the surface area of an alga to its volume *SA/V* (cm^{-1}), one can quantify this dependence. Fig. 7, *a* shows graphs illustrating the revealed dependence of the efficiency indicator of the use of macroalgae for the purpose of bioremediation on its morphometric characteristic *SA/V*. This dependence is stable, obtained in many numerical experiments with different initial conditions and mass ratios between the biological components of the marine ecosystem. Maximum performance indicators were

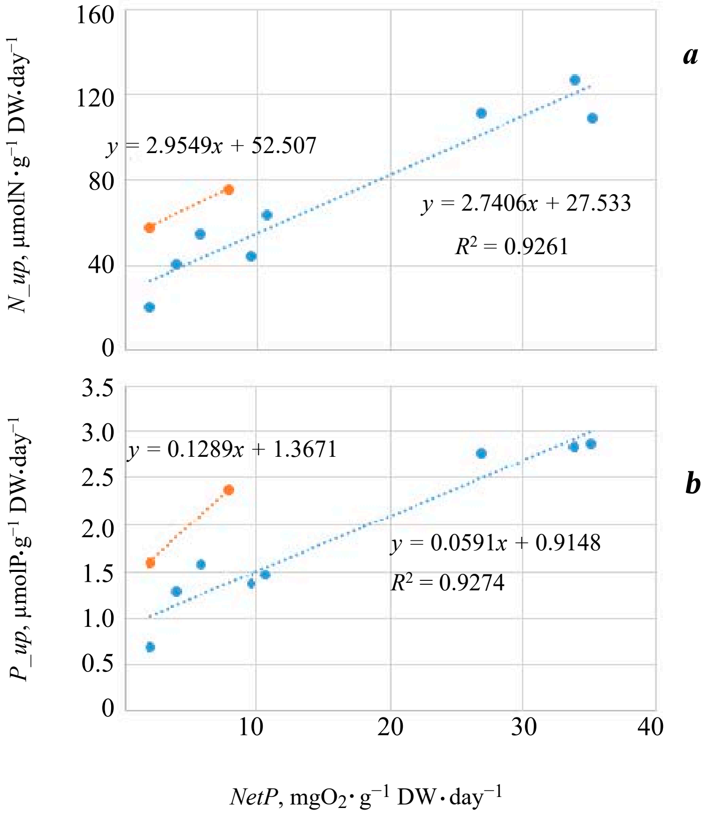

Fig. 5. Linear relationships between nitrogen (*a*) and phosphorus (*b*) assimilation rates and net plant production expressed in the units of oxygen for macroalgae (blue); seagrasses (orange)

obtained for the brown alga Cystoseira and red Phyllophora. Both species are dominant in the structure of benthic phytocenoses growing on rocky soils in the coastal zone of Crimea.

Unfortunately, reliable estimates of *SA/V* for seagrasses in the literature were not be found, so the function in Fig. 7, *a* was built only for macroalgae. The normalized values of the efficiency indicator for all model marine plant species are shown in Fig. 7, *b*. *Phyllophora* and *Cystoseira* have the highest potential for bioremediation among the considered macroalgae. Seagrasses have comparatively better properties than macroalgae phytocenosis in general.

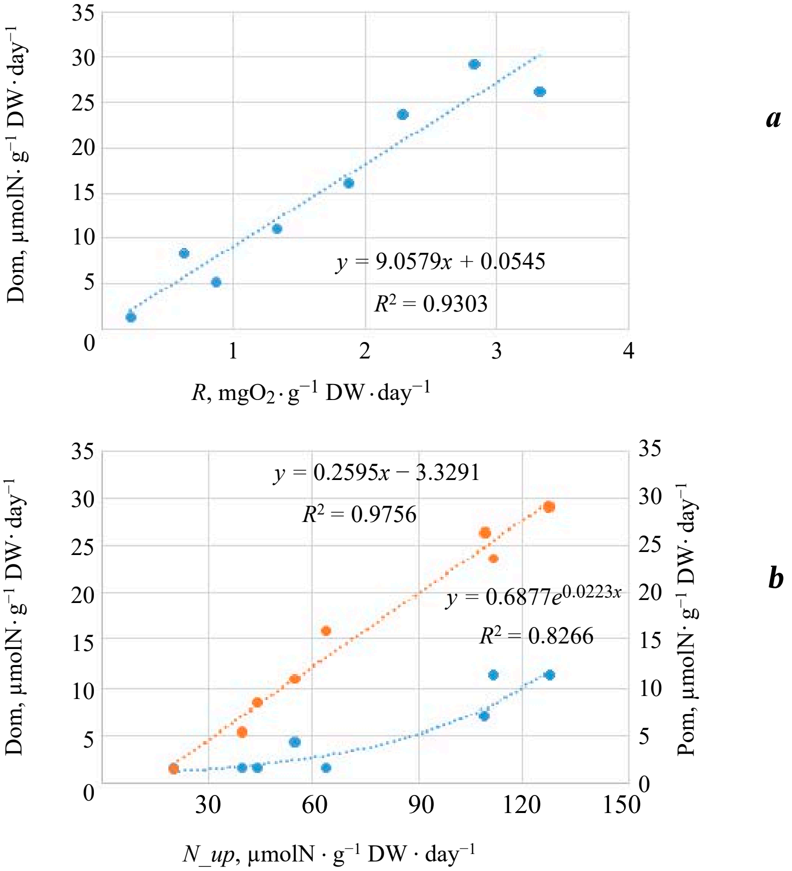

Fig. 6. Identified relationships between uptake and release rates during macroalgae functioning: release of dissolved organic matter as a function of a respiratation rate (*a*); release of particulate (blue) and dissolved (orange) organic matter as a function of nitrogen assimilation rate (*b*)

The leader is *Zostera marina*, which is also the dominant species of benthic phytocenoses on sandy soils in the coastal zone of Crimea. It is noteworthy that the efficiency of nitrogen and phosphorus assimilation by plants differs.

The efficiency indicator of the uptake of nutrients from the environment characterizes the response of the system to a sharp impact in the form of a discharge of polluted waters with a high concentration of nitrogen and phosphorus.

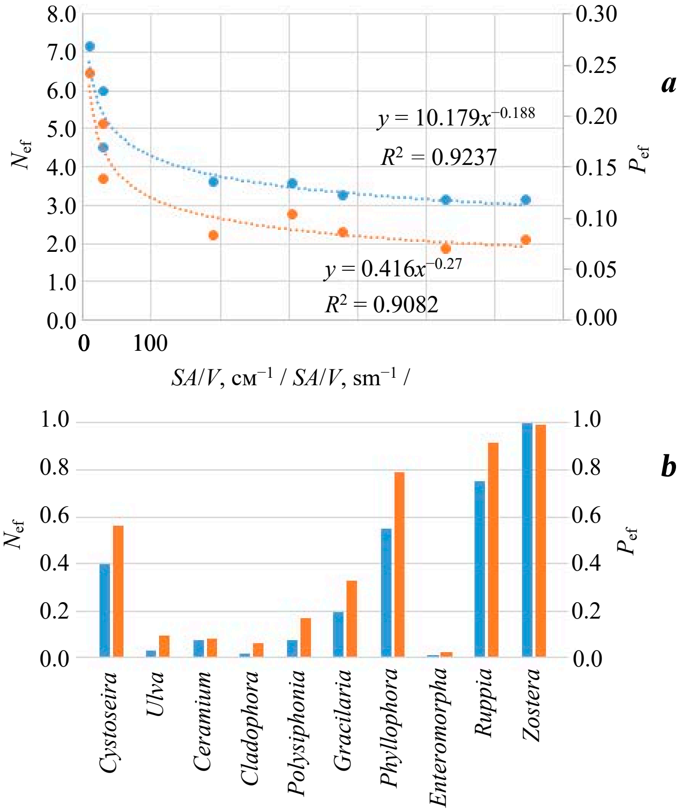

F i g . 7 . Nitrogen $N_{ef} = N\_up/(\mathrm{Dom} + \mathrm{Pom})$ (blue) and phosphorus $P_{ef} = P\_up/(\mathrm{Dom} + \mathrm{Pom})$ (orange) assimilation efficiency indicators as a function of morphometric characteristic of macroalgae *SA/V* (*a*); normalized efficiency indicators for macroalgae and sea grasses (*b*)

During the first day, there is an active consumption and accumulation of biogenic elements in algae tissues, after which their concentration in water decreases and the system stabilizes. In a stable state, the efficiency indicators for various algae converge, although they do not level out. Clear dependences on the morphometric characteristics of *SA*/*V* manifest themselves precisely in the process of rapid growth of the alga under conditions of an increased concentration of biogenic substances, accompanied by their intensive removal and synthesis of primary production.

Conclusion

In recent decades, in the coastal zone of the Black Sea (as well as in many other areas of the World Ocean), there has been a restructuring of benthic phytocenoses with significant changes in their structure. With a decrease in the dominant species biomass and an increase in the proportion of fine-structured green algae species (which have the ability to grow rapidly at elevated nitrogen concentrations in water), the bioremediation potential of bottom phytocenoses sharply decreases, and, accordingly, the possibilities of self-purification of the reservoir decrease. The growth of anthropogenic pressure on the coastal area in the form of growing volumes of nutrient discharges leads to the gradual replacement of seagrasses as the dominant producer of organic carbon by macroalgae by rapidly growing green algae that have competitive advantages compared to brown and red algae species with coarser thalli structure. Further degradation of phytocenoses could lead to the development of stagnant phenomena in the water basin with transition to the mass phytoplankton development and displacement of macroalgae.

The simulation experiments performed under the conditions of competitive relationships between phytoplankton, macroalgae, and seagrasses made it possible to obtain visual confirmation of the well-known statements about the importance of preserving the structure of benthic phytocenoses, typical for the era of low anthropogenic loads, and restoring this structure to maintain a healthy state of the coastal zone ecosystems. A comparative analysis of the efficiency of nutrients accumulation in the tissues of marine plants clearly showed the advantages of seagrasses, brown and red macroalgae with a relatively coarse thalli structure in the process of self-purification of a water basin under stress loads.

REFERENCES

1. Smith, S.V., 1981. Marine Macrophytes as a Global Carbon Sink. *Science*, 211(4484), pp. 838–840. https://doi.org/10.1126/science.211.4484.838
2. Charpy-Roubaud, C. and Sournia, A., 1990. The Comparative Estimation of Phytoplanktonic, Microphytobenthic and Macrophytobenthic Primary Production in the Oceans. *Marine Microbial Food Webs*, 4(1), pp. 31–57. Available at: https://www.researchgate.net/publication/32980521_The_comparative_estimation_of_phytoplanktonic_and_microphytobenthic_production_in_the_oceans [Accessed: 04 September 2022].
3. Friedrich, J., Janssen, F., Aleynik, D., Bange, H.W., Boltacheva, N., Çagatay, M.N., Dale, A.W., Etiope, G., Erdem, Z. [et al.], 2014. Investigating Hypoxia in Aquatic Environments: Diverse Approaches to Addressing a Complex Phenomenon. *Biogeosciences*, 11(4), pp. 1215–1259. https://doi.org/10.5194/bg-11-1215-2014
4. Orekhova, N.A. and Konovalov, S.K., 2019. Biogeochemistry of Oxygen Deficiency in Nearshore Black Sea Regions of Crimea. In: MEDCOAST, 2019. *Proceedings of the Fourteenth International MEDCOAST Congress on Coastal and Marine Sciences, Engineering, Management and Conservation*. Ortaca, Mugla, Turkey: Mediterranean Coastal Foundation. Vol. 1, pp. 297–306.
5. Duarte, C., Losada, I., Hendriks, I., Mazarrasa, I. and Marbà, N., 2013. The Role of Coastal Plant Communities for Climate Change Mitigation and Adaptation. *Nature Climate Change*, 3(11), pp. 961–968. https://doi.org/10.1038/nclimate1970

6. Smale, D.A., Pessarrodona, A., King, N., Burrows, M.T., Yunnie, A., Vance, T. and Moore, P., 2020. Environmental Factors Influencing Primary Productivity of the Forest-Forming Kelp Laminaria Hyperborea in the Northeast Atlantic. *Scientific Reports*, 10(1), 12161. https://doi.org/10.1038/s41598-020-69238-x
7. Hajlov, K.M., Prazukin, A.V., Kovardakov, S.A. and Rygalov, V.E., 1992. *Functional Morphology of Marine Multicellular Algae*. Kiev: Naukova Dumka, 280 p. (in Russian).
8. Blinova, E.I. and Saburin, M.Yu. Phytobenthos Underwater Congregations and Storm Casts of Macrophytes, and Impact thereof on the Ecology of the Anapa Bay (Black Sea). In: M. V. Pereladov, ed., 2005. *Coastal Hydrobiological Investigations: VNIRO Proceedings*. Moscow: VNIRO Publishing. Vol. 144, pp. 286–293 (in Russian).
9. Stepanyan, O.V., 2020. Macrophytobenthos of the Black and Azov Seas: Floristic and Ecological Aspects (Overview). *Nauka Yuga Rossii* [Science in the South Russia], 16(4), pp. 26–38. https://doi.org/10.7868/S25000640200404 (in Russian).
10. Kim, J.K., Kraemer, G.P. and Yarish, C., 2014. Field Scale Evaluation of Seaweed Aquaculture as a Nutrient Bioextraction Strategy in Long Island Sound and the Bronx River Estuary. *Aquaculture*, 433, pp. 148–156. https://doi.org/10.1016/j.aquaculture.2014.05.034
11. Kim, J.K., Yarish, C., Hwang, E.K., Park, M. and Kim, Y., 2017. Seaweed Aquaculture: Cultivation Technologies, Challenges and Its Ecosystem Services. *Algae*, 32(1), pp. 1–13. https://doi.org/10.4490/algae.2017.32.3.3
12. Antsulevich, A.E., 1994. Artificial Reefs Project for Improvement of Water Quality and Environmental Enhancement of Neva Bay (St.-Petersburg County Region). *Bulletin of Marine Science*, 55(2–3), pp. 1189–1192. Available at: https://www.ingentaconnect.com/contentone/umrsmas/bullmar/1994/00000055/f0020002/art00074 [Accessed: 04 September 2022].
13. Kapkov, V.I., Saburin, M.Yu., Belenikina, O.A. and Blinova, E.I., 2005. Phytocenosis Recovery of Cystoseira Crinita (Phaeophyta) and Seaweeds Growth Dynamics at the Artificial Reefs. *Herald of Moscow University. Series 16. Biology*, (2), pp. 30–34 (in Russian).
14. Vivier, B., Dauvin, J.-C., Navon, M., Rusig, A.-M., Mussio, I., Orvain, F., Boutouil, M. and Claquin, P., 2021. Marine Artificial Reefs, a Meta-Analysis of Their Design, Objectives and Effectiveness. *Global Ecology and Conservation*, 27, e01538. https://doi.org/10.1016/j.gecco.2021.e01538
15. Vasechkina, E., 2020. Object-Based Modeling of Marine Phytoplankton and Seaweeds. *Journal of Marine Science and Engineering*, 8(9), 685. https://doi.org/10.3390/jmse8090685
16. Vasechkina, E.F. and Filippova, T.A., 2019. Modeling of the Biochemical Processes in the Benthic Phytocenosis of the Coastal Zone. *Physical Oceanography*, 26(1), pp. 47–62. doi:10.22449/1573-160X-2019-1-47-62
17. Pankeeva, T.V., Mironova, N.V. and Novikov, B.A., 2019. Mapping of Bottom Vegetation of Kruglaya Bay (the Black Sea, Sevastopol). *Ecological Safety of Coastal and Shelf Zones of Sea*, (3), pp. 61–71. https://doi.org/10.22449/2413-5577-2019-3-61-71
18. Zimmerman, R.C., Smith, R.D. and Alberte, R.S., 1987. Is Growth of Eelgrass Nitrogen Limited? A Numerical Simulation of the Effects of Light and Nitrogen on the Growth Dynamics of *Zostera Marina*. *Marine Ecology Progress Series*, 41(2), pp. 167–176. https://doi.org/10.3354/meps041167

19. Aveytua-Alcázar, L., Camacho-Ibar, V.F., Souza, A.J., Allen, J.I. and Torres, R., 2008. Modelling *Zostera Marina* and *Ulva* spp. in a coastal lagoon. *Ecological Modelling*, 218(3–4), pp. 354–366. https://doi.org/10.1016/j.ecolmodel.2008.07.019

20. Nayar, S., Loo, M.G.K., Tanner, J.E., Longmore, A.R. and Jenkins, G.P., 2018. Nitrogen Acquisition and Resource Allocation Strategies in Temperate Seagrass *Zostera Nigricaulis*: Uptake, Assimilation and Translocation Processes. *Scientific Reports*, 8(1), 17151. https://doi.org/10.1038/s41598-018-35549-3

21. Brix, H. and Lyngby, J.E., 1985. Uptake and Translocation of Phosphorus in Eelgrass (*Zostera Marina*). *Marine Biology*, 90(1), pp. 111–116. https://doi.org/10.1007/BF00428221

22. Afanasyev, D.F., 2008. Stocks of Some Macrophyte Species on the Black Sea Shell of Russia. In: TINRO, 2008. *Izvestiya TINRO*. Vladivostok: TINRO. Vol. 155, pp. 161–168 (in Russian).

23. Valiela, I., McClelland, J., Hauxwell, J., Behr, P.J., Hersh, D. and Foreman, K., 1997. Macroalgal Blooms in Shallow Estuaries: Controls and Ecophysiological and Ecosystem Consequences. *Limnology and Oceanography*, 42(5, p. 2), pp. 1105–1118. https://doi.org/10.4319/lo.1997.42.5_part_2.1105

24. Khailov, K.M. and Burlakova, Z.P., 1969. Release of Dissolved Organic Matter by Marine Seaweeds and Distribution of Their Total Organic Production to Inshore Communities. *Limnology and Oceanography*, 14(4), pp. 521–527. https://doi.org/10.4319/lo.1969.14.4.0521

25. Barrón, C., Apostolaki, E.T. and Duarte, C.M., 2012. Dissolved Organic Carbon Release by Marine Macrophytes. *Biogeosciences Discussion*, 9, pp. 1529–1555. https://doi.org/10.5194/bgd-9-1529-2012

26. Chen, S., Xu, K., Ji, D., Wang, W., Xu, Y., Chen, C. and Xie, C., 2020. Release of Dissolved and Particulate Organic Matter by Marine Macroalgae and its Biogeochemical Implications. *Algal Research*, 52, 102096. https://doi.org/10.1016/j.algal.2020.102096

27. Paine, E.R., Schmid, M., Boyd, P.W., Diaz-Pulido, G. and Hurd, C.L., 2021. Rate and Fate of Dissolved Organic Carbon Release by Seaweeds: A Missing Link in the Coastal Ocean Carbon Cycle. *Journal of Phycology*, 57(5), pp. 1375–1391. https://doi.org/10.1111/jpy.13198

28. Wada, S. and Hama, T., 2013. The Contribution of Macroalgae to the Coastal Dissolved Organic Matter Pool. *Estuarine, Coastal and Shelf Science*, 129, pp. 77–85. https://doi.org/10.1016/j.ecss.2013.06.007

29. Benner, R., Pakulski, J.D., Mccarthy, M., Hedges, J.I. and Hatcher, P.G., 1992. Bulk Chemical Characteristics of Dissolved Organic Matter in the Ocean. *Science*, 255(5051), pp. 1561–1564. https://doi.org/10.1126/science.255.5051.1561

30. Rao, C.K. and Indusekhar, V.K., 1987. Carbon, Nitrogen and Phosphorus Ratios in Seawater and Seaweeds of Saurashtra, North West Coast of India. *Indian Journal of Marine Sciences*, 16(2), pp. 117–121. Available at: http://nopr.niscair.res.in/bitstream/123456789/38489/1/IJMS%2016(2)%20117-121.pdf [Accessed: 04 September 2022].

31. Atkinson, M.J. and Smith, S.V., 1983. C:N:P Ratios of Benthic Marine Plants. *Limnology and Oceanography*, 28(3), pp. 568–574. https://doi.org/10.4319/lo.1983.28.3.0568

Submitted 20.03.2022; accepted after review 30.04.2022;
revised 08.07.2022; published 26.09.2022

About the authors:

Elena F. Vasechkina, Deputy Director for Research, Methodology and Education, Head of Laboratory of Simulation Modeling of Coastal Marine Ecosystem Dynamics of Department of Computational Technologies and Mathematical Modeling, Marine Hydrophysical Institute of RAS (2 Kapitanskaya St., Sevastopol, 299011, Russian Federation), Dr.Sci. (Geogr.), **ORCID ID**: **0000-0001-7007-9496**, **Scopus Author ID: 6507481336**, **ResearcherID: P-2178-2017**, *vasechkina.elena@gmail.com*

Inga P. Naumenko, Research Associate, Marine Hydrophysical Institute of RAS (2 Kapitanskaya St., Sevastopol, 299011, Russian Federation), Ph.D. (Phys.-Math.), **ResearcherID**: **U-1807-2018**, *lazarchuk.syst.analysis@mhi-ras.ru*

Tatiana A. Filippova, Junior Research Associate, Marine Hydrophysical Institute of RAS (2 Kapitanskaya St., Sevastopol, 299011, Russian Federation), **ORCID ID**: **0000-0001-5762-5894**, **Scopus Author ID: 56190548500**, **ResearcherID: AAO-5512-2020**, *deryabina1993@yandex.ru*

Contribution of the authors:

Elena F. Vasechkina – study task statement, development of the model and modeling approach, computational experiment planning, result analysis, article text preparation

Inga P. Naumenko – preparation of literature data, result analysis, article text preparation

Tatiana A. Filippova – computational experiment running, result analysis, article text preparation

All the authors have read and approved the final manuscript.

DOI: 10.22449/2413-5577-2022-3-93-103

Identification of the Species Composition of Tree and Shrub Vegetation according to Airborne Laser Scanning Data of the Anapa Bay-Bar (Black Sea)

A. V. Karagyan *, S. V. Krylenko

Shirshov Institute of Oceanology RAS, Gelendzhik, Russia
**e-mail: karagyan.arsen@yandex.ru*

Abstract
The article aims at testing a method for automatic identification of vegetation by species composition according to airborne laser scanning data with automatic determination of geometric attribute data. The article discusses the relationship between the geometric parameters of tree and shrub vegetation and its species composition. Accurate identification of the correlation of parameters allows automating the selection of species composition. This simplifies the process of inventorying vegetation by species composition on the territory. The work was based on the method of automatic identification of vegetation according to airborne laser scanning data with automatic determination of geometric attribute data. An area located on the Anapa Bay-Bar was chosen as a testing ground for the method of automatic identification of vegetation by species composition. During the work, field measurements and field interpretation of aerial photography data were carried out. The data from machine processing and field measurements were compared, the correlation indicators between the species composition and the geometric attribute data of vegetation were calculated. Based on the correlation values, verifying coefficients of the species are proposed. In addition, during the work, the error that occurs during automatic processing of airborne laser scanning data was calculated, quantitative indicators of vegetation by species composition were calculated, and average values of vegetation heights by species on the territory of the Anapa Bay-Bar were determined.

Keywords: laser scanning, Anapa Bay-Bar, automation, vegetation

Acknowledgements: this work was funded by the Russian Science Foundation under project no. 20-17-00060 “The modern stage of the evolution of sandy accumulative forms of the Azov-Black Sea coast of Russia”.

For citation: Karagyan, A.V. and Krylenko, S.V., 2022. Identification of the Species Composition of Tree and Shrub Vegetation according to Airborne Laser Scanning Data of the Anapa Bay-Bar (Black Sea). *Ecological Safety of Coastal and Shelf Zones of Sea,* (3), pp. 93–103. doi:10.22449/2413-5577-2022-3-93-103

Выделение породного состава древесно-кустарниковой растительности по данным воздушного лазерного сканирования на примере Анапской пересыпи (Черное море)

А. В. Карагян *, С. В. Крыленко

Институт океанологии им. П. П. Ширшова РАН, Геленджик, Россия
**e-mail: karagyan.arsen@yandex.ru*

Аннотация

Цель работы – тестирование методики выделения растительности по породному составу по данным воздушного лазерного сканирования с автоматическим определением геометрических атрибутивных данных. В статье рассматривается взаимосвязь между геометрическими параметрами древесно-кустарниковой растительности и ее породным составом. Точность идентификации корреляции параметров позволяет автоматизировать выделение породного состава. Тем самым упрощается процесс инвентаризации растительности по породному составу на территории. В качестве полигона для отработки методики выбрана территория, расположенная на Анапской пересыпи. В процессе работы были проведены натурные измерения и полевая дешифровка данных аэрофотосъемки. Были сопоставлены данные машинной обработки и полевых измерений, рассчитаны показатели корреляции между породным составом и геометрическими атрибутивными данными растительности. На основе значений корреляции предложены удостоверяющие коэффициенты породы. Помимо этого, в процессе работы была рассчитана ошибка, возникающая при автоматической обработке данных воздушного лазерного сканирования, определены количественные показатели растительности по породному составу, определены средние значения высот растительности по породам на территории Анапской пересыпи.

Ключевые слова: лазерное сканирование, Анапская пересыпь, автоматизация, растительность

Благодарности: работа выполнена при финансовой поддержке РНФ в рамках проекта № 20-17-00060 «Современный этап эволюции песчаных аккумулятивных форм Азово-Черноморского побережья России».

Для цитирования: *Карагян А. В., Крыленко С. В.* Выделение породного состава древесно-кустарниковой растительности по данным воздушного лазерного сканирования на примере Анапской пересыпи (Черное море) // Экологическая безопасность прибрежной и шельфовой зон моря. 2022. № 3. С. 93–103. doi:10.22449/2413-5577-2022-3-93-103

Introduction

Within the framework of complex studies of the Anapa Bay-Bar geosystem, it became necessary to develop a method for modeling the vegetation of the area under examination.

At the present stage of science and forestry development, laser scanning is widely used to determine various parameters of forest areas. Laser scanning makes it possible to determine the relief of the subsoil, the height and quality of the forest stand. Such methods will acquire great practical importance in the future.

However, these methods have been mainly developed for compact forest areas with the same-type forest stand. They are with little to no affiliation with the studies of sparse vegetation, especially maritime one.

The relevance of this work is due to the poor adaptation of laser scanning methods for automatic determination of the species in sparse non-uniform areas specific to the Black Sea coast [1].

The vegetation model of the Anapa Bay-Bar was formed on the basis of airborne laser scanning data, while it was not limited to a three-dimensional scene or a flat map [2]. The model included the localization of vegetation with the necessary attribute data. In the course of the study, an inventory map of the vegetation of the Anapa Bay-Bar was compiled, but it is not informative from the point of view of establishing the species of a shrub or a tree. For our purpose, vegetation was identified according to the height. Plants that did not exceed 1.5 m were classified as shrubs and those exceeded were classified as trees [3]. Further studies have shown that such identification results in an error [4]. This error does not play a major role, but it affects the accuracy of the received maps and data. Using the method of automatic vegetation identification [5] according to laser scanning data, it is possible to receive rather accurate attribute data consisting of the parameters of the height and radius of the crown projective cover. Having such data and knowing the relationship among them, it is possible to determine the species composition automatically, backing it up with mathematical justification and field observations. In this regard, the purpose of this work is to test the method for the automatic identification of the type of vegetation based on laser scanning data.

Materials and methods

Airborne laser scanning of the territory of the Anapa Bay-Bar was carried out in 2013–2015. To test the method for the automatic identification of the species of tree vegetation, the most typical area for the Anapa Bay-Bar was chosen, which was dominated by such species of tree vegetation as *Elaeagnus angustifolia L.* and *Tamarix ramosissima* Ledeb. [6]. Based on the allometric correlation between the parameters and the species of vegetation, with the exact identification of a tree and a shrub, it is possible to trace the relationship between their location and various geological processes directly in the vegetation area.

Field data included the results of field measurements of parameters and identification of vegetation species in the study area, which is located in the central part of the Vityazevskaya Bay-Bar to the east of the coastal buildings of the stanitsa of Blagoveshchenskaya (Fig. 1). The area of the territory where field work was carried out made more than 1 km^2. With the help of a caliper and a tape-line, the values of the trunk circumference were determined for further comparison within the sample.

The identification of vegetation was carried out in the *ENVI LiDAR* software environment via the built-in algorithm for automatic vegetation detection. The algorithm selects those points from the point cloud that correspond to the established sample and to the height parameter specified by the user [7]. Height parameters used to determine the vegetation are as follows:

- from 1.5 to 8 m for *Elaeagnus angustifolia L.*;
- from 0.5 to 3 m for *Tamarix ramosissima* Ledeb.

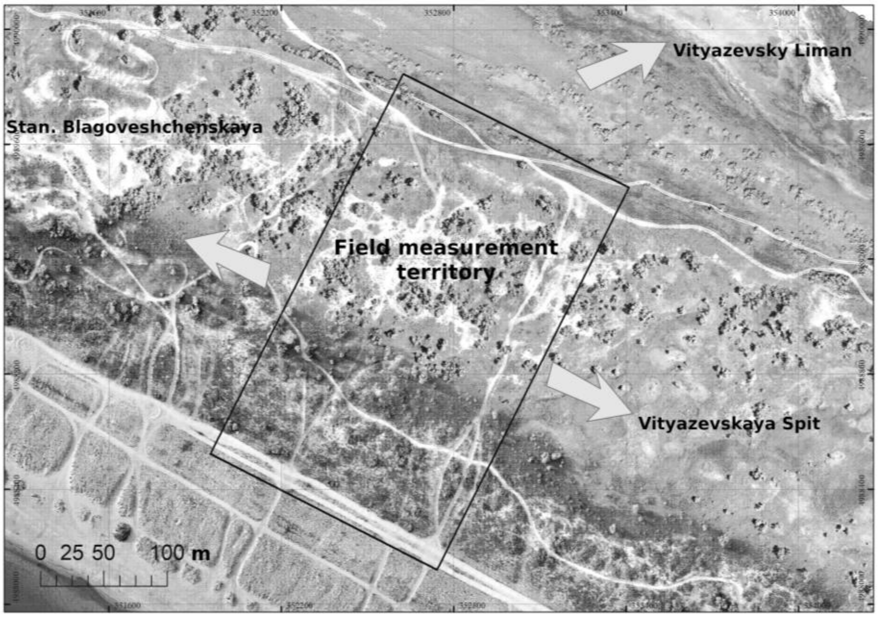

F i g . 1 . Territory of field measurements and observations

It should be noted that [8] gives the description of the vegetation growing on the territory of the Anapa Bay-Bar, which shows that the maximum height of *Elaeagnus angustifolia L.* makes 3–4 m. However, the field studies showed different result for this area with the average tree height of 5 m.

As a result of machine analysis of laser scanning points and field measurements of vegetation in the pattern, the material was collected to compare and evaluate parameters the relationship between vegetation species. The value of the trunk circumference became the key parameter, on the basis of which the species coefficient was calculated.

While establishing the most influential relationships, the correlation was calculated using the Spearman formula [9]:

$$\rho = 1 - \frac{6}{n(n-1)(n+1)} \sum_{i=1}^{n} \left(R_i - S_i \right)^2, \tag{1}$$

where R_i – rank of observation x_i in row x; S_i – rank of observation y_i in row y.

The coefficient takes values between –1 and 1. Equation $\rho = 1$ indicates strict direct linear relationship, $\rho = -1$ indicates inverse relationship [9].

Attribute data resulting from automatic vegetation identification were exported in a tabulated form. It is important to note that the results of field measurements are also included in the attribute table. Thus, a statistical series of data with a representative sample was obtained. The sample consisted of 65 units of vegetation with measured trunk circumference, and the total amount of trees and shrubs made 225 units, including the sample.

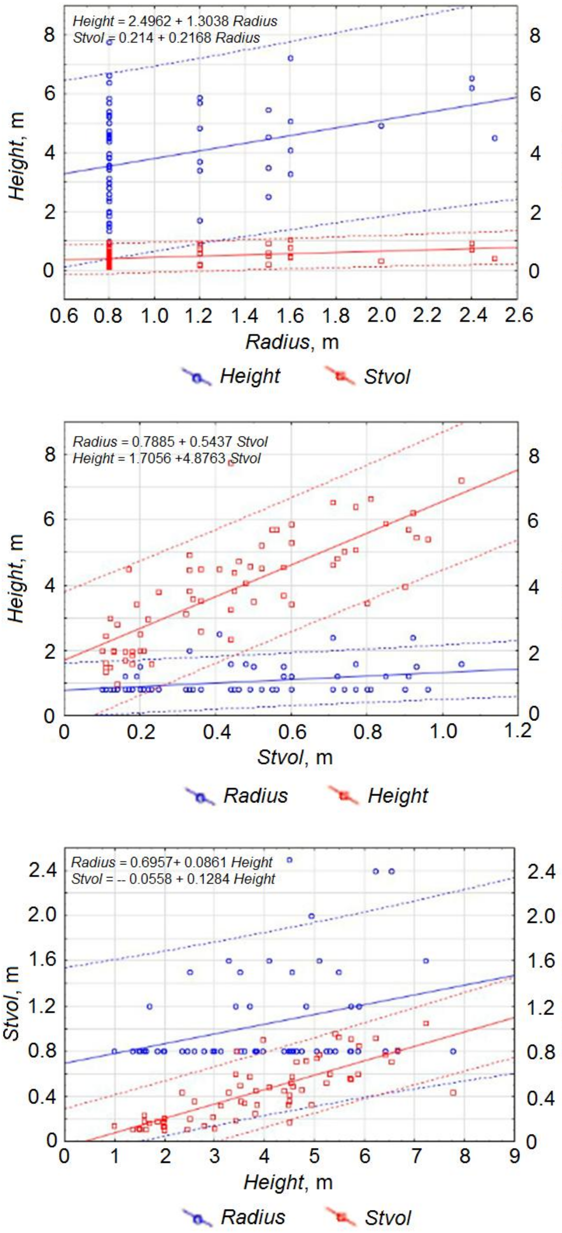

Fig. 2. Graphs of the correlation of vegetation parameters

Attribute data were processed using the *Statistic* 10.8 software. As a result, a clear picture of the relationship of vegetation allometric parameters was obtained. The correlation was calculated for the parameters of vegetation morphometry, namely: trunk circumference, projective cover radius, and vegetation height (on the graphs *Stvol*, *Radius*, *Height* respectively) (Fig. 2).

The graphs in Fig. 2 show the relationship between plant height and trunk circumference. Fig. 3 shows the initial parameters of vegetation in the form of a table of correlation indicators.

Analysis of the data in the table presented in Fig. 3 showed that there was a high correlation coefficient (0.82) between trunk circumference and height. This suggests that there is a direct relationship between these parameters. Based on this, an effort was made to calculate the individual coefficient of the plant.

The calculation was carried out empirically, as a result of which the following formula turned out to be the most accurate: $(h \cdot l_{\text{trunk}})/r$, where h – height, l – trunk circumference, r – radius of crown projective cover. The coefficients varied significantly. Thus, the average coefficient of *Elaeagnus angustifolia L.* species made 2.62, and that of *Tamarix ramosissima* Ledeb. made 0.34.

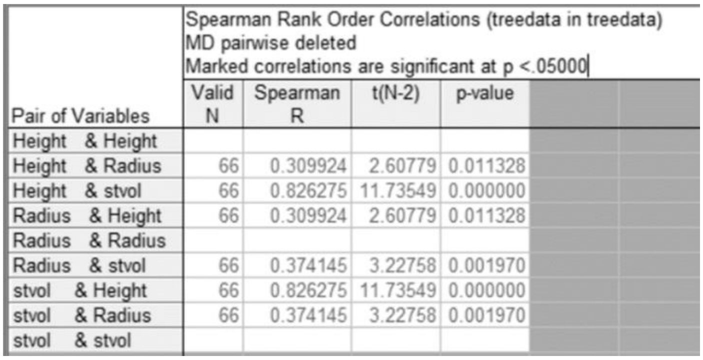

Spearman Rank Order Correlations (treedata in treedata)
MD pairwise deleted
Marked correlations are significant at p <.05000

Pair of Variables	Valid N	Spearman R	t(N-2)	p-value
Height & Height				
Height & Radius	66	0.309924	2.60779	0.011328
Height & stvol	66	0.826275	11.73549	0.000000
Radius & Height	66	0.309924	2.60779	0.011328
Radius & Radius				
Radius & stvol	66	0.374145	3.22758	0.001970
stvol & Height	66	0.826275	11.73549	0.000000
stvol & Radius	66	0.374145	3.22758	0.001970
stvol & stvol				

Fig. 3. Example of presentation of correlation parameters in *Statistic* 10.8 software

However, a problem arose during the modeling. If in the standard classification shrubs were conventionally distinguished exclusively by height, in this case field studies showed that the height of an individual shrub could be higher than assumed 1.5 m, but could not reach 3 m. This difficulty was overcome by distributing the species according to the values of the trunk circumference, in addition to the coefficient. Field studies showed that even at the maximum height of *Tamarix ramosissima* Ledeb. its trunk circumference was no more than 0.2 m. This helped resolve the problem of two species falling into the same category [10].

The next step was laboratory interpretation [11]. To calculate the error, it is necessary to accurately represent how many units of vegetation are determined incorrectly. Error calculation was performed manually [12]. The analysis showed that during the automatic identification of species, out of 2,559 vegetation units, 230 units were erroneously attributed, which made approximately 9 %. Therefore, it can be argued that this method makes it possible to automatically identify the species composition of tree and shrub vegetation with an accuracy of 91 %.

In addition, an analysis was made concerning the correspondence of the obtained *shape*-file with the vegetation index in order to eliminate the initial error in the model formation [13]. No inconsistencies were identified. Thus, the error values were established.

Results

Based on the proposed method of automatic identification of vegetation by species composition according to laser scanning data, a map of the study testing area was plotted. Areas with tree and shrub vegetation, with herbaceous vegetation and areas without vegetation were identified.

Fig. 4 shows a fragment of the study testing area. The identified areas are shown on the map. The territory without vegetation mainly includes soils or sands that cover the bay-bar.

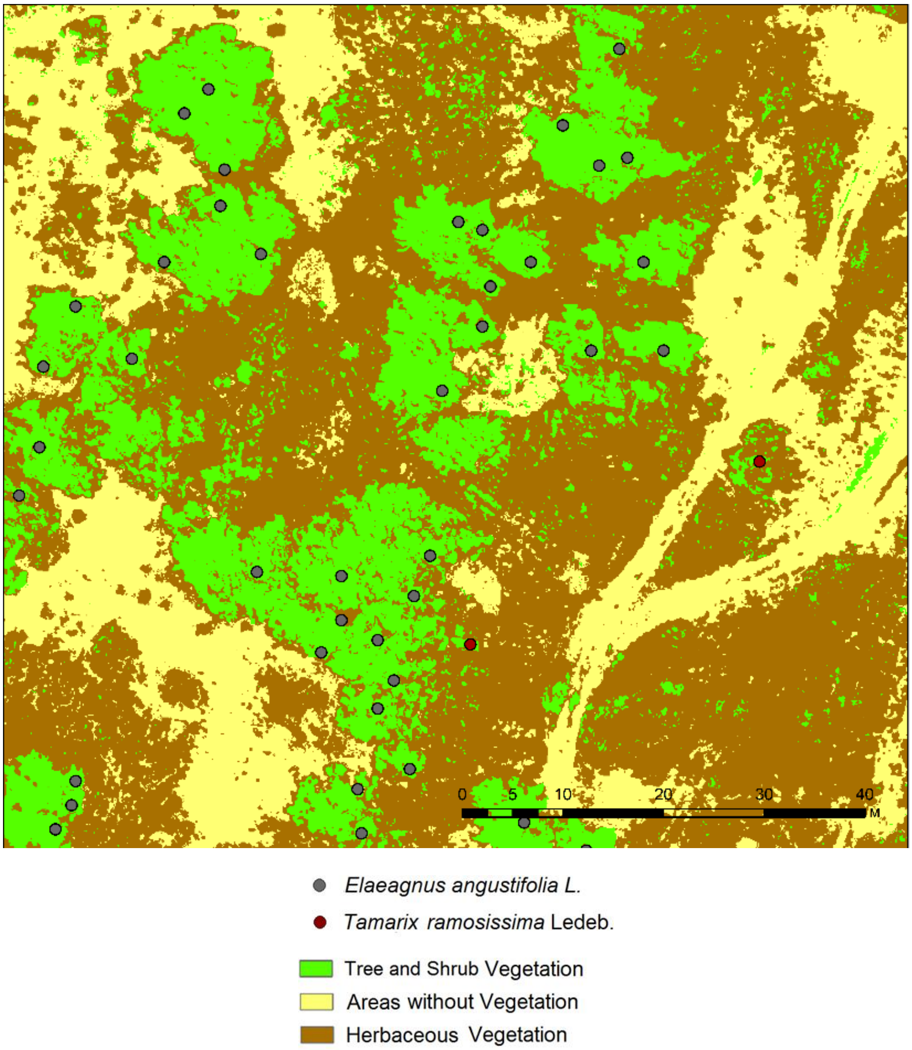

Fig. 4. Vegetation and areas of the study testing area

Fig. 5 shows the location of the points that display the geodetic center of the projection of vegetation according to the species composition of tree and shrub vegetation, which is determined by the method of correlation coefficients obtained as a result of this work [1)].

Based on the results of the image interpretation, it was found that the developed algorithm, built into *ENVI LiDAR*, determined 2,239 units of vegetation, of which 95 % were identified by the program as *Elaeagnus angustifolia L*. The remaining 5 % were identified as *Tamarix ramosissima* Ledeb. However, it should be noted that the data require additional verification [14].

[1)] Berlyant, A.M., 2002. [*Cartography. College textbook*]. Moscow: Aspekt Press, 336 p. (in Russian).

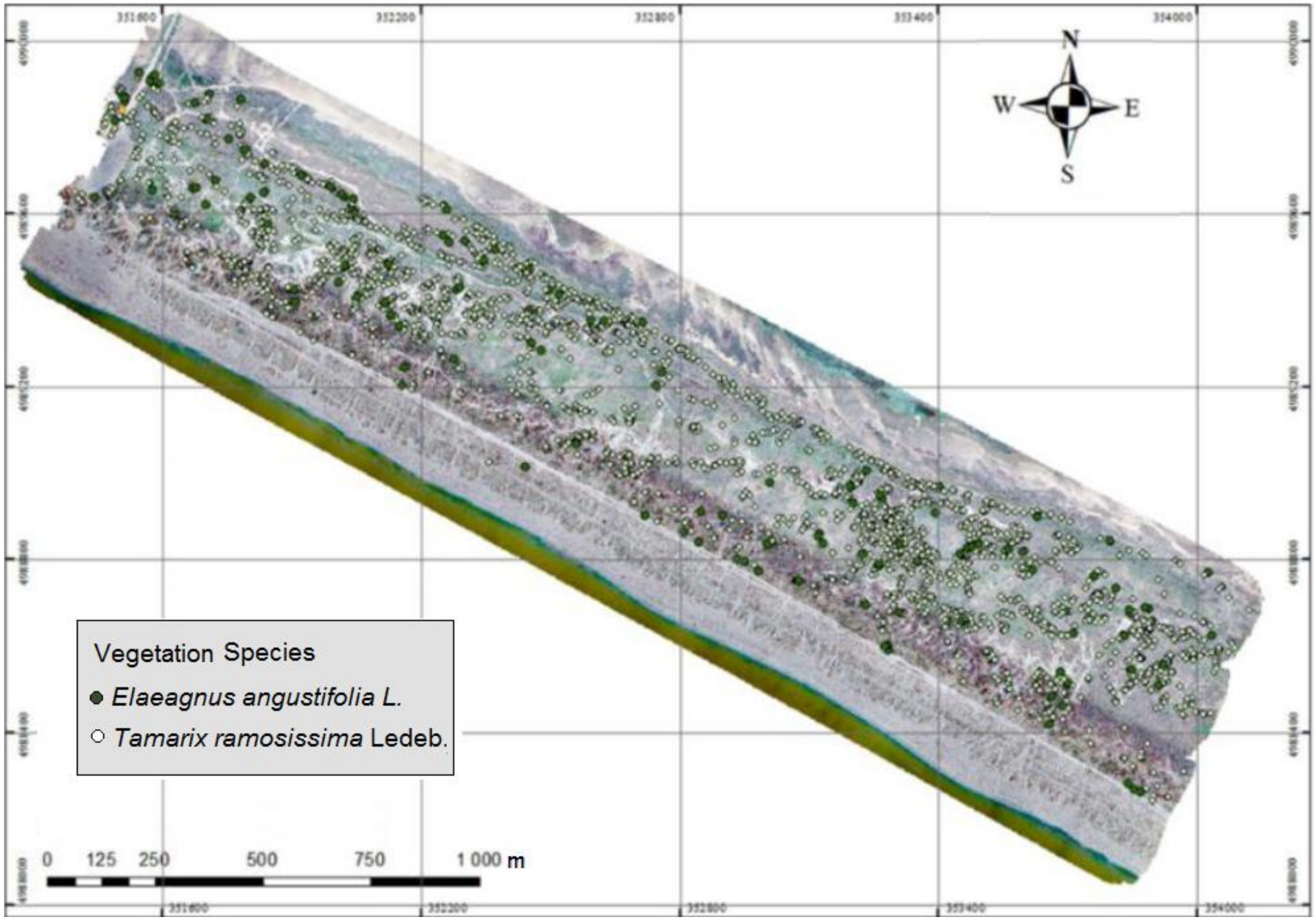

Fig. 5. Map of the study area with vegetation points

In the work, the average values of vegetation parameters were reliably determined for the study area. It was established that the average height of *Tamarix ramosissima* Ledeb. made 1.75 m, and that of *Elaeagnus angustifolia L.* made exactly 5 m. The total vegetation coverage space in the study area makes 20,351 m^2 with the space of the study testing area of 2.17 km^2 (2,170,000 m^2). This suggests that the territory covered with tree and shrub vegetation occupies only 1 % of the total study area, where *Elaeagnus angustifolia L.* prevails.

The Anapa Bay-Bar is a unique geosystem protected by the state, in the formation of which the local vegetation plays an important role. It is an indicator of various geological, soil and biological processes. The use of the method of automatic vegetation and species identification by key parameters showed that it was possible to identify vegetation with the attribute data acquisition. However, it is not known how the sample size and differentiation of the species composition will affect the algorithm. With small sample sizes, this method is useful, but with large amounts of data, accuracy can be lost.

Conclusion

1. A method to identify vegetation by species composition with its automatic determination from airborne laser scanning data was tested.
2. The individual coefficients of vegetation species were determined.
3. Maps of vegetation species and vegetation index correspondence were plotted.
4. It was established that *Elaeagnus angustifolia L.* prevailed on the territory.
5. It was established that the territory occupied by tree and shrub vegetation made 1 % of the total area.

The advantage of the method of automatic identification of the species composition of vegetation according to laser scanning data is in the speed and accuracy of such work. Owing to the automatic method of vegetation identification, it becomes possible to use attribute static data to obtain a correlation between parameters. As a result, the tasks set were solved and the necessary indicators were obtained for the automatic identification of vegetation by species composition.

Thus, it may be concluded that laser scanning as a method for obtaining spatial information is useful not only for building digital terrain models, but also in such specific areas as geomatics, dendrology, biology, and botany.

REFERENCES

1. Boyko, E., Krylenko, V. and Krylenko, M., 2015. LIDAR and Airphoto Technology in the Study of the Black Sea Accumulative Coasts. In: D. G. Hadjimitsis, K. Themistocleous, S. Michaelides and G. Papadavid, eds., 2015. *Proceedings of SPIE. Third International Conference on Remote Sensing and Geoinformation of the Environment, 16–19 March 2015, Paphos.* Paphos. Vol. 9535, 95351Q. doi:10.1117/12.2192577
2. Tkacheva, A.A. and Favorskaya, M.N., 2015. Modeling of 3D Forest Scenes by Laser Scanning and Air Photo Data. *Information and Control Systems*, (6), pp. 40–49. https://doi.org/10.15217/issn1684-8853.2015.6.40 (in Russian).
3. Boyko, E.S. and Karagyan, A.V., 2021. Digital Modeling of Tree and Shrub Vegetation of Accumulative Seashore Based on Air Laser Scanning Data. *Vestnik of SSUGT*, 26(2), pp. 103–114. https://doi.org/10.33764/2411-1759-2021-26-2-103-114 (in Russian).
4. Danilin, I.M. and Favorskaya, M.N., 2013. Description of the Software Modules for the Use of Laser Locarion and Digital Aerial Photography Data of Forest Territories. *Issledovaniye Zemli iz Kosmosa*, (2), pp. 62–73. https://doi.org/10.7868/S0205961413020024 (in Russian).
5. Melnik, I.V. and Drozdova, A.E., 2018. Loch Silver as an Environment Quality Indicator. In: A. N. Barmin and T. V. Dymova, eds., 2018. [*Environmental Problems of Natural and Urbanized Territories. Proceedings of the Ninth International Scientific and Practical Conference, Astrakhan, 24–25 May 2018*]. Astrakhan: Astrakhan State University, pp. 38–42 (in Russian).
6. Kosyan, R.D., Krylenko, V.V. and Krylenko, M.V., 2021. *Geosystem of the Anapa Bay-Bar*. Moscow: Nauchny Mir, 264 p. (in Russian).
7. Popov, R.A. and Altyntsev, M.A., 2013. The Effects of Sampling Density in Airborne Laser Scanning to Extract Individual Trees. In: I. G. Zhurkin, A. V. Komissarov, T. A. Shirokova and A. S. Gordienko, eds., 2013. [*Interexpo GEO-Siberia 2013. Proceedings of the International Exhibition and Scientific Congress. Novosibirsk, 15–26 April, 2013. Vol. 1*]. Novosibirsk: SGGA, pp. 83–87 (in Russian).
8. Nylén, T., Kasvi, E., Salmela, J., Kaartinen, H., Kukko, A., Jaakkola, A., Hyyppä, J. and Alho, P., 2019. Improving Distribution Models of Riparian Vegetation with Mobile Laser Scanning and Hydraulic Modelling. *PLOS ONE*, 14(12), e0225936. https://doi.org/10.1371/journal.pone.0225936
9. Danilin, I.M., Medvedev, E.M., Kapralova, E.N. and Pestov, K.A., 2008. Using of Contemporary Aerial Survey Technologies in Forestry. In: SSUGT, 2008. [*GEO-Siberia-2008. Proceedings of the Fourth International Scientific Congress. Novosibirsk, 22–24 April 2008. Vol. 2, Part 1*]. Novosibirsk: SGGA, pp. 209–213 (in Russian).
10. Kravtsova, V.I., Falaleeva, A.A. and Chalova, E.R., 2014. The Morphologically Contrasting Regions Mapping of Blagovestchensk Section of Anapa Sent Area Using Space Images of High Resolution. *Geodesy and Cartography*, (10), pp. 25–36. doi:10.22389/0016-7126-2014-892-10-25-36 (in Russian).
11. Rylskiy, I.A., 2018. Approaches to the Determination of Taxation Indicators of Forests Using Aerospace Images and Lidar Data. *Proceedings of the International conference “InterCarto. InterGIS”*, 24(2), pp. 216–240. http://doi.org/10.24057/2414-9179-2018-2-24-216-240 (in Russian).

12. Novakovskiy, B.A., Kovach, N.S. and Antin, A.L., 2014. Geoinformation Technologies to Use Air Laser Scanning to Solve Geographic and Cartographic Tusks. *Geodesy and Cartography = Geodezia i Kartografia* (7), pp. 44–48. doi:10.22389/0016-7126-2014-889-7-44-48 (in Russian).
13. Starikov, A.V. and Baturin, K., 2015. The Use of Laser Scanning Technology of Accounting for Wood. *Forestry Engineering Journal*, 5(4), pp. 114–122. https://doi.org/10.12737/17409 (in Russian).
14. Myagkov, V.F., 2008. [On Geostatistics in Geometrization of Deposits]. *News of the Higher Institutions. Mining Journal*, (1), pp. 54–65 (in Russian).

Submitted 20.12.2021; accepted after review 28.05.2022;
revised 6.07.2022; published 26.09.2022

About the authors:

Arsen V. Karagyan, Engineer, Shirshov Institute of Oceanology RAS (1G Prostornaya St., Gelendzhik, 353467, Russian Federation), **ORCID ID: 0000-0001-9673-9114**, **ResearcherID: ABG-5516-2020**, *karagyan.arsen@yandex.ru*

Sergey V. Krylenko, Engineer, Shirshov Institute of Oceanology RAS (1G Prostornaya St., Gelendzhik, 353467, Russian Federation), **ORCID ID: 0000-0003-0411-8455**, **ResearcherID: ABG-5398-2020**, *krylenkoserg@mail.ru*

Contribution of the authors:

Arsen V. Karagyan – task statement, data processing, coefficient calculation, model development, field observations and measurements

Sergey V. Krylenko – field observations and measurements, field interpretation of tree species, parameter description for model development

All the authors have read and approved the final manuscript.

DOI: 10.22449/2413-5577-2022-3-104-116

Assessment of Pollution of the Yalta Bay Ecosystem Components with Organochlorine Xenobiotics

L. V. Malakhova *, V. V. Lobko

A.O. Kovalevsky Institute of Biology of the Southern Seas of RAS, Sevastopol, Russia
**e-mail: malakh2003@list.ru*

Abstract

Assessment of pollution of water, brown algae of the genus *Cystoseira* sp., and bottom sediments of Yalta Bay with organochlorine xenobiotics, which include DDT and polychlorinated biphenyls (PCBs), was conducted according to 2017–2020 data. The concentration of these organochlorine compounds was compared with the recommended standards for their content in the marine environment: threshold limit value in water as well as international threshold levels of threshold effect concentration (TEC) and probable effect concentrations (PEC) in sediments. In spring 2017, the average concentration of PCBs in water exceeded 1.2 times the threshold limit value for seawater, which is 10 ng/L. In *Cystoseira* sp., organochlorine compounds accumulated with high accumulation coefficients varying for DDT and its metabolites DDE and DDD and six indicator congeners of PCBs in the range from $1 \cdot 10^3$ to $2 \cdot 10^4$, which indicated high bioavailability of the studied substances. Extremely high concentrations of DDT were detected in the surface layers of bottom sediments, exceeding by a factor of 46 the recommended TEC threshold levels, equal to 5.3 ng/g dry weight for the sum of concentrations of DDT and its metabolites (∑DDT). The distribution profiles of ∑DDT in soil cores at the two stations show a general tendency for their content to decrease with depth increasing. In the cores, the sum of six PCB indicator congeners concentrations (∑6PCB) did not exceed the TEC for PCBs, equal to 60 ng/g dry weight. The source of pollution of Yalta Bay with organochlorine compounds was the Vodopadnaya River runoff, due to which ∑DDT intake was 1.5 g/year and that of ∑6PCB was 5.2 g/year.

Keywords: DDT, PCB, water, sediments, *Cystoseira* sp., Vodopadnaya River, Yalta Bay

Acknowledgments: the work was carried under state assignment of IBSS “Molismological and biogeochemical foundations of the marine ecosystems homeostasis” (121031500515-8).

For citation: Malakhova, L.V., Lobko, V.V., 2022. Assessment of Pollution of the Yalta Bay Ecosystem Components with Organochlorine Xenobiotics. *Ecological Safety of Coastal and Shelf Zones of Sea*, (3), pp. 104–116. doi:10.22449/2413-5577-2022-3-104-116

Оценка загрязненности хлорорганическими ксенобиотиками компонентов экосистемы Ялтинского залива

Л. В. Малахова *, В. В. Лобко

ФГБУН ФИЦ «Институт биологии южных морей имени А. О. Ковалевского РАН», Севастополь, Россия
**e-mail: malakh2003@list.ru*

Аннотация
По данным 2017–2020 гг. проведена оценка загрязненности хлорорганическими ксенобиотиками, к которым относятся ДДТ и полихлорбифенилы (ПХБ), воды, бурых водорослей рода *Cystoseira* sp. и донных отложений Ялтинского залива. Сравнивали концентрации данных хлорорганических соединений с рекомендованными нормами их содержания в морской среде: ПДК в воде, международными пороговыми уровнями *TEC* (*Threshold Effect Concentration*) и *PEC* (*Probable Effect Concentrations*) – в донных отложениях. В весенний сезон 2017 г. средняя концентрация ПХБ в воде превышала в 1.2 раза ПДК в морской воде, составляющую 10 нг/л. В цистозире определены высокие коэффициенты накопления хлорорганических соединений, изменяющиеся для ДДТ, его метаболитов ДДЭ и ДДД и шести индикаторных конгенеров ПХБ в интервале от $1\cdot10^3$ до $2\cdot10^4$, что свидетельствует о высокой биодоступности исследуемых веществ. В поверхностных слоях донных отложений обнаружены экстремально высокие концентрации ДДТ, превышающие в 46 раз *TEC*, равный 5.3 нг/г сухой массы для суммы концентраций ДДТ и его метаболитов (∑ДДТ). На профилях распределения ∑ДДТ в керне грунтов на двух станциях проявляется общая тенденция к уменьшению содержания пестицидов группы ДДТ с увеличением глубины. Сумма концентраций шести индикаторных конгенеров ПХБ (∑6ПХБ) в кернах не превышала *TEC* для ПХБ, равного 60 нг/г сухой массы. Источником загрязнения Ялтинского залива хлорорганическими соединениями являлся сток р. Водопадной, с которым поступление ∑ДДТ составляло 1.5 г/год, а ∑6ПХБ – 5.2 г/год.

Ключевые слова: ДДТ, ПХБ, вода, донные отложения, *Cystoseira* sp., река Водопадная, Ялтинский залив

Благодарности: работа выполнена в рамках темы государственного задания ФИЦ ИнБЮМ «Молисмологические и биогеохимические основы гомеостаза морских экосистем» (№ 121031500515-8).

Для цитирования: *Малахова Л. В., Лобко В. В.* Оценка загрязненности хлорорганическими ксенобиотиками компонентов экосистемы Ялтинского залива // Экологическая безопасность прибрежной и шельфовой зон моря. 2022. № 3. С. 104–116. doi:10.22449/2413-5577-2022-3-104-116

Introduction

The entry into the marine environment of a large volume of technogenic pollutants has led to the formation of the so-called critical zones in certain areas of the Black Sea, where natural biogeochemical processes do not provide self-purification of the ecosystem from incoming pollutant flows, including organochlorine compounds (OCs) [1]. When studying the self-purification mechanisms of such areas on the example of Sevastopol Bay, it was determined that in the 21st century the priority organic pollutants of technogenic origin are OCs, which include polychlorinated biphenyls (PCBs) and compounds of the p,p'-dichlorodiphenyltrichloroethane (DDT) group [2]. OCs are persistent organic pollutants that degrade extremely slowly under environmental conditions and can accumulate in hydrobionts and bottom sediments. High concentrations of OCs have an acute toxic effect on living organisms, while low concentrations have a chronic effect, which over time causes malignant tumors [3], decrease in reproductive function, and other homeostasis disorders [4]. DDT and PCBs enter the Black Sea environment mainly with river, industrial, agricultural, domestic effluents, atmospheric fallout, and discharges in dumping areas.

Yalta Bay is one of the most important recreational areas of Crimea. Yalta is located at its top. It is known that since the 1970s sewage runoff from Yalta goes through the system of deep-water discharge of domestic and waste water, the commissioning of which has led to a decrease in pollution of the coastal zone of Yalta, a decrease in the eutrophication of Yalta Bay and an improvement in its ecological state as a whole [5]. Currently, the sources of pollution of Yalta Bay in the Yalta region are economic activities of the seaport, the flow of the Vodopadnaya and Derekoika Rivers, storm surface runoff and melting snow cover. In the data yearbooks on the seawater quality of the FSE SOI named after N.N. Zubov there is information about high water pollution of Yalta Bay with organochlorine pesticides (OCPs) in the 1980s, when the DDT concentration in the port water reached 26, and lindane – 100 ng/L, and about the decrease of their content in 2008–2013 to concentrations below the threshold limit value for seawater, which is 10 ng/L 1). In recent years, it has been shown that in the spring season, the content of OCs in the water near the mouth of the Vodopadnaya River can exceed the threshold limit value in seawater [6, 7].

OCs entering marine areas are included in the cycle of substances in ecosystems, and due to their physicochemical properties, they are adsorbed on suspended mineral and organic particles, accumulate in hydrobionts and eventually enter bottom sediments, where OCs concentrations can reach extremely high values and remain unchanged for a long period of time [8].

To date, no comprehensive studies of the content of OCs in water, hydrobionts and bottom sediments of Yalta Bay have been carried out. In this regard, the purpose of the work is to assess the contamination of the biotope and biocenosis components of Yalta Bay ecosystem with organochlorine xenobiotics.

Materials and methods

The study area is located in Yalta Bay, which juts out into the southern coast of Crimea for 3 km. The sampling of water, *Cystoseira* and bottom sediments (BS) was carried out in the mouth area of the Vodopadnaya River, flowing into the water area of Yalta Bay within the boundaries of Yalta; and in the open area of the bay from 2017 to 2020 at the stations, the diagram of which is shown in Fig. 1. The coordinates and station depths are presented in Table. 1.

---

1) Order no. 552 of Ministry of Agriculture of the Russian Federation as of 13 December 2016. Available at: http://docs.cntd.ru/document/420389120 [Accessed: 13 September 2022]. (in Russian).

Fig. 1. Scheme of the water, *Cystoseira* and sediments sampling area in Yalta Bay: 1–5 – water sampling stations; 4 – *Cystoseira* sampling station near the Vodopadnaya River outlet; 1, 5 – sediment core sampling stations (https://yandex.ru/maps/11470/yalta/?ll=34.200931%2C44.472756&z=13.08).

The samples of river and seawater from the surface layer were taken into glass containers with screw caps and stored in a refrigerator at 4°C until analysis. The sample volume was 5 litres. *Cystoseira* samples were taken at station 4 (Fig. 1) in the coastal area, subject to the influence of the Vodopadnaya River runoff. At stations 1 and 5 with a gravity-type tubular sampler, the bottom sediment cores were sampled without disturbing the sediment stratification. After sampling with a piston extruder, the bottom sediment columns were divided into layers 1 cm thick, which were weighed, dried to constant weight to determine the amount of natural moisture, carbonate content, and OCs content in them.

OCs in water were determined by gas chromatography method in accordance with the guidelines of federal environmental regulations 14.1:2:3:4.204-04 (2014). The extraction of OCs from unfiltered samples was carried out with hexane (*Cryochrome*, Russia) no later than 24 h after sampling. If necessary, the extracts were purified with concentrated sulfuric acid (high purity grade).

To assess the content of OCs in hydrobionts, the perennial brown alga *Cystoseira* sp., which is very sensitive to pollution of the marine environment, was chosen [9]. Before analysis, the algae were purified from epiphytes, washed with distilled water, dried to constant weight, and thoroughly ground. OCs were extracted three times from an aliquot (5 g) of the sample with a mixture of hexane and acetone in an ultrasonic bath at 30 °C, the extracts were combined, and concentrated on a rotary evaporator. The concentrated extract was purified through a column with florisil. OCs were eluted with hexane.

Table 1. Coordinates of sampling stations in Yalta Bay

Station number	Lat, N	Lon, E	Depth, m
1	44° 29.2234′	34° 10.9130′	29.4
2	44° 29.1806′	34° 10.9530′	31.0
3	44° 28.6701′	34° 10.3051′	33.9
4	44° 29.3294′	34° 09.8040′	1.0
5	44° 28.4208′	34° 10.0072′	34.0

Preparation of bottom sediment samples and analysis of OCs in them was carried out in accordance with GOST R 53217–2008. OCs were extracted twice from 5 g of dried and homogenized bottom sediments with a mixture of n-hexane and acetone (*EKOS-1*, Russia) in a ratio of 3:1. The combined extract was concentrated to 1 ml on a rotary evaporator and then the extract was purified by column chromatography method with 2 g of florisil (*Merk*, Germany). Sulfur was removed from the bottom sediment extracts using activated metallic copper (*Komponent-Reaktiv*, Russia).

Determination of OCs in the prepared extracts of water, *Cystoseira* and bottom sediments was carried out at the Spectrometry and Chromatography Research Center of the Institute of Biology of the Southern Seas on a Kristall 5000 gas chromatograph (*Khromatek*, Russia) with an electron capture microdetector (ECD) and a 30-meter capillary CR-5 stationary phase column. Separation in the presence of OCs was provided by the following conditions of the chromatographic system: evaporator temperature – 280 °C; initial column temperature – 150 °C (0 min); further heating at a rate of 5 °C/min to 220 °C (2 min), then 2 °C/min to 240 °C (2 min) and 5 °C/min to 290 °C (10 min), ECD temperature – 300 °C, carrier gas – nitrogen, flow divider – 1:20.

The concentrations of DDT and its metabolites p,p'-DDE and p,p'-DDD (hereinafter DDE and DDD), as well as six PCB indicator congeners (numbers are given according to the IUPAC nomenclature) were measured in the samples: 28, 52, 101, 138, 153 and 180. Quantitative calculations were carried out by the absolute calibration method. OCs standards were purchased from *Sigma-Aldrich*. The error in the determination of OCs did not exceed 30 % at their content up to 1, 20 % – from 1 to 10, 15 % – over 10 ng/l in water or ng/g dry weight in bottom sediments and *Cystoseira*.

In bottom sediment samples, the natural moisture content was determined by the gravimetric method, and the carbonate content (in calcite equivalent) was determined by the fast gasometric method after decomposition of carbonates with hydrochloric acid [10].

To assess the intensity of OCs influx from water into *Cystoseira* and bottom sediments, the accumulation coefficients AC were calculated according to the formula

$$\mathrm{AC} = C\mathrm{o} \cdot 1000 / C\mathrm{w}, \qquad (1)$$

where Co – concentrations of OCs in the object of study: *Cystoseira* or bottom sediments, ng/g dry weight; Cw – concentration of OCs in water, ng/l.

Estimation of the average annual removal of OCs R_{ocs} (g) was calculated according to the formula [2)]

$$R_{\mathrm{ocs}} = C_{\mathrm{ocs}} \cdot W,$$

where C_{ocs} is average concentration of OCs in water in the mouth area of the river, g/m^3; W is average annual runoff of the Vodopadnaya River, m^3.

The ecotoxicological assessment of sediment pollution was analyzed by comparing the measured concentrations with the threshold effect level

---

[2)] Hydrochemical Institute, 1983. [*Temporal Recommended Practice for Calculation of Organic Substances, Nutrients, Pesticides and Trace Elements Removal with River Runoff*]. Moscow: Gidrometeoizdat, 32 p. (in Russian).

in bottom sediments, below which side effects were not expected (TEC, Threshold Effect Concentration), and with the probable effect level (PEC, Probable Effect Concentrations), above which adverse effects would be observed. According to the 2003 recommendations[3)] for precipitation quality, TEC for ∑DDT is 5.3, and for ∑PCB it is 60 µg/kg dry weight, PEC is 572 and 670 µg/kg dry weight, respectively.

Results and discussion

Table 2 shows the average annual concentrations of DDT, its metabolites and six PCB indicator congeners in the surface water layer in the Yalta sea area and in the water of the Vodopadnaya River.

From 2017 to 2020, the sum of concentrations of DDT and its metabolites DDE and DDD (∑DDT) in the surface water layer of the Yalta sea area varied from 3.8 to 40.0 % (average 14.2 %) of the threshold limit value in seawater, the sum of six PCB indicator congeners (∑6PCB) – from 22.3 to 127.5 % (average 68 %) of the threshold limit value, which is 10 ng/l for OCs in seawater. In the summer seasons, relatively low concentrations of OCs were observed in the water of Yalta Bay, the maximum values of which did not exceed the threshold limit value. An excess of the threshold limit value was observed for PCBs in the spring season of 2017, which may be due to the intake of PCBs with terrigenous runoff during floods. In 2020, the concentration of ∑6PCB in the Vodopadnaya River turned out to be on average twice lower than in the adjacent Yalta sea area. DDT with metabolites at the sampling point in the bay was not found, while DDT and DDE were determined in the river water, and their concentration did not exceed 2.5 % of the threshold limit value.

To assess the removal of OCs with the runoff of the Vodopadnaya River in the Yalta sea area, the mean long-term annual flow of river water in its mouth area was taken, which was 0.151 m^3/s [11]. About 0.005 km^3 of water enters the water area of Yalta Bay with the river runoff per year. Calculations of OCs

Table 2. Average concentration of OCs (ng/L) in the water of the surface layer of the Yalta sea area and the Vodopadnaya River

Region	Year	p,p' DDE	p,p' DDD	p,p' DDT	PCB congeners					
					28	52	101	153	138	180
Yalta sea area	2017	0.40	N/D	0.45	N/D	3.00	1.85	1.18	3.32	1.56
	2019	1.17	0.69	0.77	0.63	0.11	1.68	0.53	1.22	2.58
	2020	N/D	N/D	N/D	N/D	1.63	0.21	N/D	0.22	N/D
Vodopadnaya River	2020–2021	0.25	N/D	0.14	N/D	0.66	0.37	0.19	0.23	0.15

Note: N/D – not detected.

[3)] Contaminated sediment standing team, 2003. *Consensus-Based Sediment Quality Guidelines. Recommendations for Use and Application*. Wisconsin, 2003. 35 p. Available at: https://dnr.wi.gov/doclink/rr/RR088.pdf [Accessed: 12 September 2022].

removal using formula (1) based on the average concentration of ∑DDT and ∑6PCB in the mouth area of the Vodopadnaya River, which was 0.32 and 1.09 ng/l, respectively, and the annual water runoff showed that the intake of ∑DDT was 1.50 g/year. The intake of ∑6PCB turned out to be 3.4 times higher than that of ∑DDT and amounted to 5.19 g/year.

A comparison was made of the obtained OCs fluxes in the sea with the runoff of the Vodopadnaya River and the results obtained in 2020 of the OCs removal from the Chernaya River into Sevastopol Bay. With an average annual concentration of ∑DDT and ∑6PCB in the mouth area of the Chernaya River equal to 0.57 and 3.45 ng/l, the discharge into the bay with the river runoff was 21 and 126 g/year, respectively [8]. The obtained values showed that with a difference in the average concentration in water of ∑DDT by 1.7 and ∑6PCB by 3.2 times, the contribution of the Vodopadnaya River in the OCs pollution of the sea area was lower than the contribution of the Chernaya River, an average of 22 times, which is associated with a lower annual runoff of the Vodopadnaya River. The same results were previously obtained when considering the pollution of the Sea of Azov with pesticides coming from small rivers, the contribution of which was proportional to their runoff [12].

As an alternative to the assessment of OCs pollution in the water area by water analysis, the determination of pollutants in marine macroalgae is used [13]. The data on macroalgae contamination was first published in the early 1950s and is still widely used to assess the ecological state of marine ecosystems. However, most studies (97 %) dealt with inorganic pollutants, and only 3 % of them were devoted to organic pollution [14].

At present, the state of macrophytes of Yalta Bay has hardly been studied. According to the oral testimonies of the staff of the NBG-NSC, the *Cystoseira* phytocenosis of the coastal region of Yalta is in a depressed state and occurs in the form of fouling on artificial substrates: moorings, breakwaters, etc. In April and June 2017, OCs contamination of the brown alga *Cystoseira* sp. was studied for the first time in the Yalta sea area. Despite more than a 50-year ban on the use of DDT and a 30-year ban on PCBs, *Cystoseira* samples contained both the parent pesticide and its metabolites DDE and DDD and all six PCB indicator congeners, the highest of which was the concentration of low-chlorinated congener 28 (Table 3).

The accumulation coefficients for individual OCs in *Cystoseira* varied from $1 \cdot 10^3$ to $2 \cdot 10^4$, which indicates a significant bioavailability of OCs.

Table 3. OCs concentration (ng/g dry weight) in algae *Cystoseira* sp. in the coastal area of Yalta Bay

Date	DDE	DDD	DDT	PCB congeners					
				28	52	101	153	138	180
19.04.2017	0.65	0.44	0.63	2.16	1.11	0.56	0.90	1.19	0.52
28.06.2017	0.75	0.37	0.42	2.48	0.96	0.85	1.28	1.57	0.43

There is some published data on OCs contamination of marine brown algae, which indicates that the maximum OCs contamination of the algae *Cystoseira* sp. was observed in the 1980s (Table 4), when OCs were widely used in industry and agriculture in many countries [15]. OCs in brown algae were found not only in the coastal areas of inland seas, but also in the southern latitudes of the Antarctic region [16, 17].

Comparison of the obtained results with the published data (Table 4) showed that the concentrations of PCBs in Yalta Bay *Cystoseir*a exceeded those in the Cape Martyan marine area by more than twice, and the DDT content, taking into account the determination error of 20 %, was approximately equal [18].

Fig. 2 shows the results of layer-by-layer measurements of the initial moisture content and carbonate content of bottom sediments at stations 1 and 5. The moisture content of bottom sediments characterizes their porosity associated with granulometric composition [19]. Precipitation with low humidity values (30–40 % or less) is characteristic of bottom sediments formed by lithogenic material entering water bodies as a result of abrasion of the coastal zone and with slope water runoff. The values of carbonate content obtained in this work, which at station 1 changed

Table 4. Mean OCs concentration (ng/g dry weight ± SD) in *Cystoseira* sp. and other brown algae in different areas of the World Ocean

Region	Years	Name	∑DDT	∑PCB	Reference
East coast of Sicily, Italy	1979	*Cystoseira stricta*	20.1	84.2	[14]
		Cystoseira fimbriata	3.2	66.4	
Coastal areas of the Southern coast of Crimea	1982–1993	*Cystoseira* sp.	ND	556–724	[15]
The Gulf of Venice	1999	*Cystoseira barbata*	ND	2.5±1.6	[17]
		Fucus virsoide		3.0±1.7	
Admiralty Bay, the Antarctic	1993–1994	*Desmarestia* sp.	ND	0.46–3.86	[16]
Cape Martyan marine area	2017–2020	*Cystoseira* sp.	2.39	2.87	[18]
Yalta Bay	2017	*Cystoseira* sp.	1.63	7.01	this paper

Note: ND – no data.

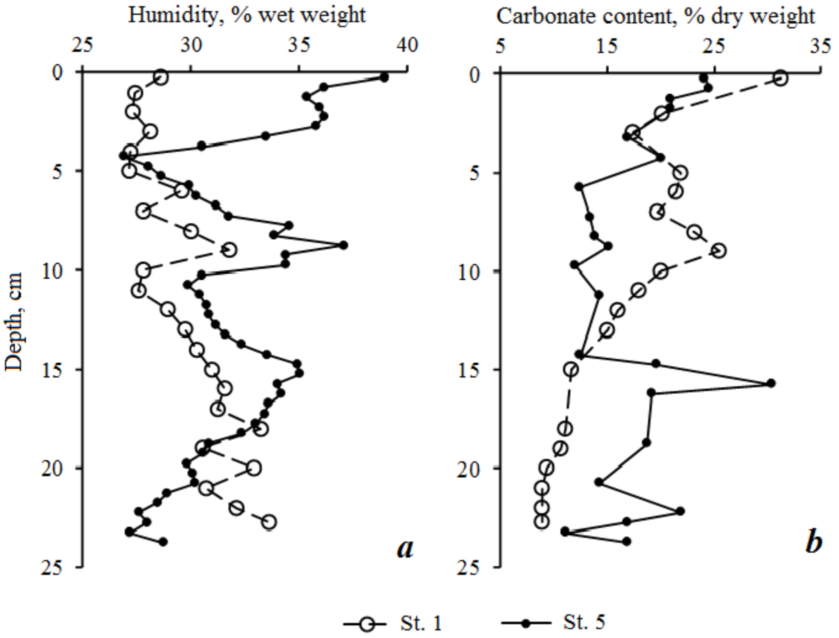

Fig. 2. Distribution of natural moisture (*a*) and carbonate content (*b*) in sediment at St. 1 and 5

from 8.9 to 31.3 %, and at station 5 changed from 12.5 to 24.6 % wet weight (Fig. 2, *b*), and bottom sediment humidity (from < 40 % in the uppermost layer to 27 % in the lower layers (Fig. 2, *a*)) indicate the predominance of lithogenic suspension in them. Porosity and carbonate content of the sediment at station 5 decreased exponentially down the core ($R^2 = 0.28$ and $R^2 = 0.34$, respectively), at station 1, porosity increased linearly ($R^2 = 0.67$), while carbonate content decreased with depth ($R^2 = 0.79$) (Fig. 2). The uneven distribution of moisture and carbonate content in sediments is probably determined by the temporal variability of the composition of sedimented suspensions in the area of coastal stations.

ΣDDT concentration in bottom sediment cores at stations 1 and 5 varied in the range from 0.1 to 387.2 ng/g dry weight, Σ6PCB varied in a narrower range from 3.4 to 17.5 ng/g dry weight (Fig. 3). At station 1, in the surface layer of the bottom sediment from 0 to 1 cm, an extremely high concentration of ∑DDT was found, which averaged 230 ng/g, while in deeper layers from 2.5 to 23 cm, the average concentration of DDT was 1.53 ng/g (Fig. 3, *a*). The sampling area of the core at station 1 falls under the influence of the Vodopadnaya River runoff, with which ∑DDT could enter the water area of the bay and fall out with suspension in the bottom sediment.

At station 1, the vertical distribution profiles of ∑6PCB and ∑DDT were significantly different. The average concentration of ∑6PCB (10.21 ng/g) in the upper centimeter layer was 20 times lower than that of DDT, while in the lower layers, on the contrary, it was an order of magnitude higher on average (Fig. 3, *a*).

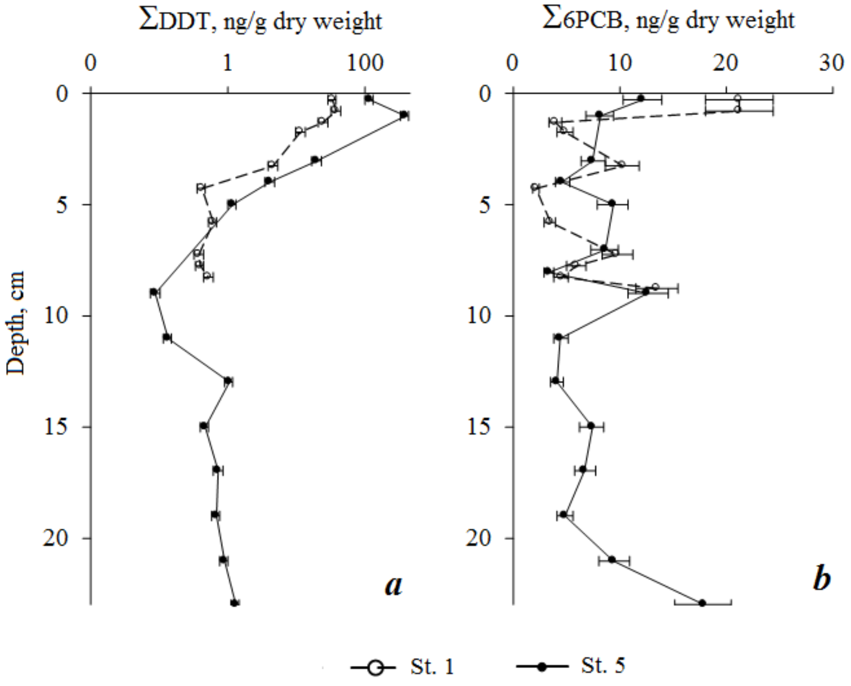

F i g . 3 . Vertical distribution of ∑DDT (a) and ∑6PCB (b) in bottom sediments at St. 1 and 5

At station 5 in the upper bottom sediment layer, the concentration of ∑DDT was six times lower (36 ng/g) than at station 1, but the same as at station 1 was significantly higher than in the underlying layers, where it averaged 1.06 ng/g. Thus, on the distribution profiles of ∑DDT in the soil core at station 5, a tendency to decrease the content of pesticides with increasing depth appeared in common with station 1.

In the surface layers of both cores, the sum of concentrations of DDT and metabolites was dominated by the initial pesticide DDT (78 and 74 %), with the depth of sediments this ratio decreased to 34 and 22 % at stations 1 and 5, respectively. This indicates new DDT intakes into the water area of the bay in recent years.

The vertical profiles of OCs in the sediment core in Yalta Bay were compared with those in Sevastopol Bays, where the maximum ∑PCB contamination, reaching 400 ng/g, was observed in Sevastopol Bay at a depth of 15–20 cm, and in Streletskaya Bay, at a depth of 10–15 cm. Bottom sediments at these depths were accumulated taking into account the sedimentation rates in the 1970s–1980s. In the surface layers of Streletskaya and Sevastopol Bays, the concentration of OCs was significantly lower than at the indicated depths. In Balaklava Bay, as well as in Yalta Bay, the highest concentration of PCBs was found in the surface layers [6].

Based on the OCs concentration data in the water and surface layer of bottom sediments, using formula (1), the accumulation coefficients (AC) of OCs in the bottom sediments of Yalta Bay were calculated, and varied for individual OCs in a wide range from $0.6 \cdot 10^3$ to $4 \cdot 10^4$. The minimum AC were determined for heptachlorobiphenyl (IUPAC number 180), the highest were determined for DDT and tetrachlorobiphenyl (52).

The level of OCs contamination was compared with the TEC threshold values in bottom sediments. At stations 1 and 5, the PCB concentration did not reach TEC, and ∑DDT in the surface layers exceeded TEC, but did not reach the lower threshold level PEC.

Conclusion

For the first time, a comprehensive assessment of the ecological state of Yalta Bay in relation to OCs pollution was carried out. The studies showed that the levels of PCBs in water during the spring season exceeded the threshold limit value. The sources of OCs in Yalta Bay include the Vodopadnaya River. The high OCs accumulation coefficients in *Cystoseira* and bottom sediments indicate bioavailability of OCs and the ongoing process of OCs removal from the marine environment by macrophytes and soils. On the vertical distribution profiles of DDT concentration in the surface layers, the values were found that exceeded the recommended international standards by a maximum of 46 times. This registered fact indicates that in recent years the Yalta sea area received a significant amount of DDT, which managed to accumulate in the upper layers of bottom sediments. It should be noted that such high concentrations of DDT in recent years have not been recorded in the bottom sediments of Sevastopol bays and in the areas of the southern coast of Crimea, which indicates a local source of DDT entry into the water area of Yalta Bay. It remains unclear whether the high concentration of DDT pesticide in the surface layers in the sediment cores of Yalta Bay is the result of its entry into the water area with terrigenous runoff, atmospheric precipitation, river runoff, or from other sources. Further studies of both the spatial distribution of DDT and the vertical profiles in the bottom sediments of Yalta Bay are needed to determine the extent of their contamination.

REFERENCES

1. Egorov, V.N., Gulin, S.B., Popovichev, V.N., Mirzoyeva, N.Yu., Tereshenko, N.N., Lazorenko, G.E., Malakhova, L.V., Plotitsina, O.V., Malakhova, T.V. et al., 2013. Biogeochemical Mechanisms of Formation of Critical Zones Concerning to Pollutants in the Black Sea. *Marine Ekological Journal = Morskoj Ehkologicheskij Zhurnal*, 12(4), pp. 5–26 (in Russian).
2. Egorov, V.N., Gulin, S.B., Malakhova, L.V., Mirzoyeva, N.Yu., Popovichev, V.N., Tereshchenko, N.N., Lazorenko, G.E., Plotitsyna, O.V., Malakhova, T.V. et al., 2018. Biogeochemical Characteristics of the Sevastopol Bay Sedimentation Self-Purification from Radionuclides, Mercury and Chlorogenic Contaminants. *Marine Biological Journal*, 3(2), pp. 40–52. https://doi.org/10.21072/mbj.2018.03.2.03 (in Russian).
3. Cogliano, V.J., 1998. Assessing the Cancer Risk from Environmental PCBs. *Environmental Health Perspectives*, 106(6), pp. 317–323. doi:10.1289/ehp.98106317
4. Olufsen, M. and Arukwe, A., 2011. Developmental Effects Related to Angiogenesis and Osteogenic Differentiation in Salmon Larvae Continuously Exposed to Dioxin-

Like 3,3′,4,4′-Tetrachlorobiphenyl (Congener 77). *Aquatic Toxicology*, 105(3–4), pp. 669–680. doi:10.1016/j.aquatox.2011.09.005

5. Zats, V.I., Nemirovskiy, M.S., Andryushchenko, B.F., Kandybko, V.V., Stepanov, V.N., Agarkov, A.K., Shulgina, E.F., Kiseleva, M.I., Senichkina, L.G. and Fedorenko, L.V., 1973. [*Experience of Theoretical and Experimental Study of the Issue of Deep Water Waste Water Discharge: the Case of Yalta Area*]. Kiev: Naukova Dumka, 274 p. (in Russian).
6. Malakhova, L.V., Egorov, V.N. and Malakhova, T.V., 2019. Organochlorine Compounds in Components of Sevastopol Bays, Cape Martyan Nature Reserve Marine Area and Yalta Port Ecosystems. *Water: Chemistry and Ecology*, (1–2), pp. 57–62 (in Russian).
7. Ryabinin, A.I., Klimenko, N.P. and Bobrova, S.A., 2015. Organochlorine Pesticides in Northern Coastal Waters of the Black Sea. In: V. M. Gruzinov, ed., 2015. *Proceedings of N.N. Zubov State Oceanographic Institute*. Moscow: SOI. Iss. 216, pp. 288–306 (in Russian).
8. Malakhova, L.V., Lobko, V.V., Malakhova, T.V. and Murashova, A.I., 2022. Comparative Assessment of Organochlorine Pollution of Bottom Sediments in Different Types of Water Bodies in the Sevastopol Region (Crimea). *Chemistry for Sustainable Development*, 30(2), pp. 169–181. doi:10.15372/CSD2022371
9. Zaitsev, Yu., 2008. *An Introduction to the Black Sea Ecology*. Odessa: Smil Edition and Publishing Agency ltd, 228 p.
10. Sokolov, V.S. and Sokolova, E.G., 1980. [Simple Gasometric Method of $CaCO_3$ Determination in Expeditions]. In: E. A. Ostroumov, 1980. [*Chemical Analysis of Marine Sediments*]. Moscow: Nauka, pp. 42–45 (in Russian).
11. Borovskiy, B.I. and Timchenko, Z.V., 2005. [Hydroenergetic Potentials of Crimean Rivers]. In: National Academy of Environmental and Resort Construction, 2005. *Construction and Technogenic Safety*. Simferopol: National Academy of Environmental and Resort Construction. Issue 11, pp. 182–186 (in Russian).
12. Min'kovaskaya, R.Ya., 2017. Assessment Pollution Export of Organochlorine Pesticides by the Rivers to the Sea of Azov. *Ecological Safety of Coastal and Shelf Zones of Sea*, (1), pp. 66–78 (in Russian).
13. García-Seoane, R., Fernández, J.A., Villares, R. and Aboal, J.R., 2018. Use of Macroalgae to Biomonitor Pollutants in Coastal Waters: Optimization of the Methodology. *Ecological Indicators*, 84, pp. 710–726. doi:10.1016/j.ecolind.2017.09.015
14. Amico, V., Oriente, J., Piattelli, M. and Tringali, C., 1979. Concentrations of PCBs, BHCs and DDTs Residues in Seaweeds of the East Coast of Sicily. *Marine Pollution Bulletin*, 10(6), pp. 177–179. doi:10.1016/0025-326X(79)90427-2
15. Polikarpov, G.G. and Zherko, N.V., 1996. Ecological Aspects of Studying of Pollution of the Black Sea by Organochlorine Xenobiotics. *Ecology of the Sea*, 45, pp. 92–100 (in Russian).
16. Montone, R.C., Taniguchi, S., Sericano, J., Weber, R.R. and Lara, W.H., 2001. Determination of Polychlorinated Biphenyls in Antarctic Macroalgae Desmarestia sp. *Science of the Total Environment*, 277(1–3), pp. 181–186. doi:10.1016/S0048-9697(00)00876-7
17. Pavoni, B., Caliceti, M., Sperni, L. and Sfriso, A., 2003. Organic Micropollutants (PAHs, PCBs, pesticides) in Seaweeds of the Lagoon of Venice. *Oceanologica Acta*, 26(5–6), pp. 585–596. doi:10.1016/S0399-1784(03)00052-5
18. Egorov, V.N., Gorbunov, R.V., Plugatar ,Yu.V., Malakhova, L.V., Sadogurskiy, S.E., Artemov, Yu.G., Proskurnin, V.Yu., Mirzoyeva, N.Yu., Marchenko, Yu.G. et al., 2021. Cystoseira Phytocenosis as a Biological Barrier for Heavy Metals and Organochlorine

Compounds in the SPNA Cape Martyan Marine Area (the Black Sea). *Regional Studies in Marine Science*, 41, 101572. doi:10.1016/j.rsma.2020.101572

19. Gavshin, V.M., Lapukhov, S.V., Saraev, S.V., Tanygin, G.I., Khrischev, H.G., Ruskova, N.P., Georgiev, V.M., Chochov, S.D, Aslanyan, S.O., Kozhukharov, E.D., Andreev A.P. and Kazansky Yu. P., 1988. [*Lithogenesis Geochemistry in the Presence of Hydrogene Sulfide Contamination (the Black Sea)*]. Novosibirsk: Nauka, 194 p. (in Russian).

Submitted 2.06.2022; accepted after review 25.06.2022;
revised 08.07.2022; published 25.09.2022

About the authors:

Lyudmila V. Malakhova, Senior Researcher, A.O. Kovalevsky Institute of Biology of the Southern Seas of RAS (2 Nakhimov Av., Sevastopol, 299011, Russian Federation), PhD(Bio), **ORCID ID: 0000-0001-8810-7264**, **Scopus AuthorID: 35604200900**, **ResearcherID: E-9401-2016**, *malakh2003@list.ru*

Veronika V. Lobko, Junior Research Associate, A.O. Kovalevsky Institute of Biology of the Southern Seas of RAS (2 Nakhimov Av., Sevastopol, 299011, Russian Federation), **ORCID ID: 0000-0001-9993-3764**, **Scopus AuthorID: 57219128787**, **ResearcherID: F-8156-2019**, *lobkoveronika@gmail.com*

Contribution of the authors:

Lyudmila V. Malakhova – problem statement, gas chromatographic analysis of OCs, analysis of results, discussion of results, preparation of graphic materials, writing the article

Veronika V. Lobko – sampling, primary processing of samples, determination of the natural humidity of precipitation, determination of carbonation, discussion of results, preparation of the text of the article

All the authors have read and approved the final manuscript.

DOI: 10.22449/2413-5577-2022-3-117-127

Organic Matter of the Bottom Sediments of the Ca Gau and Long Tau Rivers in the Can Gio Biosphere Reserve (Vietnam)

E. A. Tikhonova [1] *, O. V. Soloveva [1], Nguyen Trong Hiep [2]

[1] *A.O. Kovalevsky Institute of Biology of the Southern Seas of RAS, Sevastopol, Russia*
[2] *Southern Branch of Joint Vietnam-Russia Tropical Science and Technology Research Center, HoChiMinh, Vietnam*
**e-mail: tihonoval@mail.ru*

Abstract
The purpose of the work is to assess the level of organic substances, including oil hydrocarbons, and the effect of water dynamics on the content of these substances in the bottom sediments of the river – sea contact zone of the Ca Gau and Long Tau Rivers located on the territory of the buffer zone of the Can Gio Biosphere Reserve (Vietnam, Southeast Asia). The following indicators of the ecological well-being of the water area were identified: physical-chemical indicators of water (pH, eH, salinity, temperature), concentration of chloroform-extractable substances and oil hydrocarbons in bottom sediments. Determination of chloroform-extractable substances in bottom sediments was carried out by the gravimetric method, oil hydrocarbons were determined by infrared spectrometry. The measurements were carried out on an FSM-1201 spectrophotometer. In the bottom sediments of the river Ca Gau and Long Tau, the recorded concentrations of chloroform-extractable compounds (from 54 to 90 mg/100 g) and oil hydrocarbons (from 9.6 to 13.8 mg/100 g) were close to trace levels. The study of some rivers of the Can Gio Reserve showed that this water area can be characterized as relatively safe in terms of the determined parameters. As a result of active water circulation in estuarine areas of rivers flowing in mangroves, physical-chemical characteristics of the environment underwent significant changes during the high tide: increase in salinity (by 1–5 PSU) and pH (by 0.24–0.31 units on average), and decrease in redox potential (by 9–18 mV). However, no close correlation between the changes in physical-chemical characteristics of the environment and the content of organic substances was revealed. This phenomenon is probably associated with the movement of bottom sediments and is only significant for chloroform-extractable substances in the estuarine part of the Long Tau River.

Keywords: river bottom sediments, chloroform-extractable substances, oil hydrocarbons, Can Gio Biosphere Reserve, Vietnam

Acknowledgments: the study was carried out by researchers of the Joint Vietnam-Russia Tropical Science and Technology Research Center and the A.O. Kovalevsky Institute of Biology of Southern Seas of RAS according to their research projects: 1) Ekolan E-3.4. Ecosystem of the Mekong River in the context of global climate change and anthropogenic impact; and 2) Molismological and biogeochemical foundations of homeostasis of marine ecosystems. (no. 0556-2021-0001, state registration no. 121031500515-8). The authors express their sincere gratitude for providing primary prepared and delivered material to the staff of the Department of Radiological and Chemical Biology of IBSS: N. N. Tereshchenko, leading research associate, Ph.D., I. G. Sidorov, junior research associate, and O. D. Chuzhikova-Proskurnina, leading engineer.

For citation: Tikhonova, E.A., Soloveva O. V. and Nguyen Trong Hiep, 2022. Organic Matter of the Bottom Sediments of the Ca Gau and Long Tau Rivers in the Can Gio Biosphere Reserve (Vietnam). *Ecological Safety of the Coastal and Shelf Zones of the Sea*, (3), pp. 117–127. doi:10.22449/2413-5577-2022-3-117-127

Органическое вещество донных наносов рек Кагау и Лонгтау в биосферном заповеднике Канзё (Вьетнам)

Е. А. Тихонова [1] *, О. В. Соловьёва [1], Нгуен Чонг Хиеп [2]

[1] *ФГБУН ФИЦ «Институт биологии южных морей имени А. О. Ковалевского РАН»,*
Севастополь, Россия
[2] *Южное отделение Совместного Российско-Вьетнамского*
Тропического научно-исследовательского и технологического центра,
Хошимин, Вьетнам
**e-mail: tihonoval@mail.ru*

Аннотация

Цель работы – оценка уровня содержания органических веществ, в том числе нефтяных, и влияния динамики вод на содержание данных веществ в донных наносах контактной зоны река – море рек Кагау и Лонгтау, расположенных на территории буферной зоны биосферного заповедника Канзё (Вьетнам, Юго-Восточная Азия). В качестве показателей экологического благополучия акватории были выбраны: физико-химические показатели воды (pH, Eh, соленость, температура), концентрация хлороформ-экстрагируемых веществ и нефтяных углеводородов в донных наносах. Определение хлороформ-экстрагируемых веществ в донных отложениях проводили весовым методом, нефтяных углеводородов – методом инфракрасной спектрометрии. Измерение проводили на спектрофотометре «ФСМ-1201». В донных наносах рек Кагау и Лонгтау зафиксированные концентрации хлороформ-экстрагируемых соединений (от 54 до 90 мг/100 г) и нефтяных углеводородов (от 9.6 до 13.8 мг/100 г) близки к следовым количествам. Проведенное исследование рек заповедника Канзё показало, что по определяемым параметрам данную акваторию можно характеризовать как относительно благополучную. В результате активной циркуляции вод в эстуарных районах рек, протекающих в мангровых зарослях, в период прилива происходят существенные изменения физико-химических показателей среды: рост солености (на 1–5 епс), повышение показателей pH (в среднем на 0.24–0.31 ед.), снижение окислительно-восстановительного потенциала (на 9–18 мВ). Однако тесной зависимости изменения физико-химических характеристик среды от содержания органических веществ не выявлено. Данное явление, вероятно, связано с перемещением донных наносов и носит достоверный характер только для хлороформ-экстрагируемых веществ в эстуарной части р. Лонгтау.

Ключевые слова: речные донные отложения, хлороформ-экстрагируемые вещества, нефтяные углеводороды, биосферный заповедник Канзё, Вьетнам

Благодарности: настоящее исследование выполнено в рамках НИР Совместного Российско-Вьетнамского Тропического научно-исследовательского и технологического центра (СРВТНИиТЦ) «Эколан Э-3.4. Экосистема реки Меконг в условиях глобальных климатических изменений и антропогенного воздействия», темы гос. задания ФГБУН ФИЦ «Институт биологии южных морей имени А. О. Ковалевского РАН (ФИЦ ИнБЮМ) «Молисмологические и биогеохимические основы гомеостаза морских экосистем» (№ 0556-2021-0001, № гос. регистрации: 121031500515-8). Авторы выражают искреннюю благодарность сотрудникам отдела радиационной и химической безопасности (ОРХБ ФИЦ ИнБЮМ) вед. н. с., к. б. н. Н. Н. Терещенко, м. н. с. И. Г. Сидорову, вед. инж. О. Д. Чужиковой-Проскурниной за предоставленный первичный подготовленный и доставленный материал.

Для цитирования: *Тихонова Е. А., Соловьева О. В., Нгуен Чонг Хиеп.* Органическое вещество донных наносов рек Кагау и Лонгтау в биосферном заповеднике Канзё (Вьетнам) // Экологическая безопасность прибрежной и шельфовой зон моря. 2022. № 3. С. 117–127. doi:10.22449/2413-5577-2022-3-117-127

Introduction

Can Gio Nature Reserve (Vietnam, Southeast Asia) acquired a biosphere reserve status in 2000. It includes mangrove forests southeast of Ho Chi Minh City. These forests are the green lungs of the country's biggest industrial city and harbour some of the largest diversity of mangrove plant species, invertebrates living in the thicket, and associated fishes and mollusks (URL: https://en.unesco.org/biosphere/aspac/can-gio).

The Can Gio region has a subequatorial tropical monsoon climate with two distinct seasons: the rainy season from May to October and the dry season from November to April with an average temperature of 25–29°C [1].

The total area of the Reserve is 757.4 km². It is divided into three key areas: the major area of 47.21 km², the buffer area of 411.39 km² (of which 38 km² is water area), and the transition area of 298.8 km² (of which 5.7 km² is water area). There are no settlements in the major and buffer zones. Shrimp fishing is carried out in some channels. Today, people living in the transition area (about 70,000 people) produce an additional pressure on the Reserve. Previously, in 1997, 54,000 people lived there, and before the Reserve was opened, in total 58,000 people lived in the area. Nowadays, the main fields of activity for the local population are agriculture and water management, fishing, salt mining and tourism.

The proximity of Ho Chi Minh City, the largest industrial city in Vietnam, cannot but affect the environmental situation in the protected area. This provides the need to control pollutants in the components of the Reserve's ecosystem.

Different ecosystems are represented within the Reserve: mangrove forests (40 % of the area), salt and mud marshes, grassy marine area (45 %) and agricultural land (15 %). The Kan Gio mangrove forest grows on swampy soils formed by alluvial clay deposits of the Saigon and Ong Nai Rivers. In addition, there are many large estuaries (Long Tau, Ca Gau and other rivers) along the coast. The area of the rivers and canals is 22,161 hectares accounting for 31.5 % of the Ho Chi Minh City area. Water from the East Sea enters the river system mainly at high tide. In the mixing zone, the most intensive processes of sedimentation of suspended solids brought by river water occur [1] and active accumulation of pollutants takes place [2].

At high tide, the movement of water masses transports surface bottom sediments. The nature of sediment movement depends on its physical characteristics (particle size distribution, particle density, hydraulic grain size etc.) and on the speed and depth of the water flow. In turn, various pollutants are actively accumulated in the bottom sediments. Tides are known to transfer particles up to 2 mm in diameter [3] with a predominance of particles up to 0.5 mm. It is this fraction of bottom sediments that can most actively accumulate organic molecules [4, 5]. Thus, it can be assumed that the content of organic compounds, including pollutants, in the downstream bottom sediments, in the river – sea contact zone, may to some extent alter the environmental indicators of the Reserve.

In that context, the aim of this work is to assess the levels of organic substances, including oil ones, and the impact of water dynamics on the content of those substances in the bottom sediments of the river – sea contact zone of the Ka Gau and Long Tau Rivers located within the buffer zone of Kan Gio Biosphere Reserve.

Materials and methods

The material for the study was sediment samples (0–2 cm) collected from the Ka Gau (Area 1: Stations 1.1, 1.2, 1.3) and Long Tau (Area 2: Stations 2.1, 2.2, 2.3) Rivers in the buffer zone of Kan Gio Biosphere Reserve (Fig. 1). In each area, river sediment was sampled at three points located across the riverbed: two nearshore points near the right and left banks and in the middle of the riverbed. The nature of the river sediment taken at Station 2.2 (mixture of sand and coarse pebbles) did not allow further chemical analysis. Samples were taken at two time periods: low tide (*R*) and high tide (*L*). Chemical-physical characteristics of water (pH, Eh, salinity) of the studied rivers were determined *in situ* with a Hanna HI9829 Multimeter by the staff of the environmental analysis laboratory of the Southern Branch of Joint Vietnam-Russia Tropical Science and Technology Research Center (JVRTSTRC). The temperature during the sampling period averaged 29.9 °C.

Determination of chloroform-extractable substances and petroleum hydrocarbons. Initial processing of sediment samples was carried out at the South Branch of JVRTSTRC by the staff of the IBSS Department of Radiological and Chemical Biology. Raw sediment samples were air dried, weighed and ground to a uniform dry mass, the sample was mixed and a subsample was taken for analysis. Further processing of the bottom sediments was carried out in the IBSS Chemoecological Laboratory. The resulting air-dry mixture (5 g) was extracted with chloroform until discolouration of the washing portions, the extracts were collected in a 100 ml conical flask, the solvent was distilled off in a water bath to a residual volume of 2–3 ml and transferred to weighing bottles. After evaporation of the chloroform, the weighing bottles were weighed and the weight of the chloroform-extractable substances (CES) in the test material was thus determined. After re-dissolving the CES in carbon tetrachloride, the mixture was applied to an aluminium oxide column for determination of oil hydrocarbons (OH) on a spectrophotometer

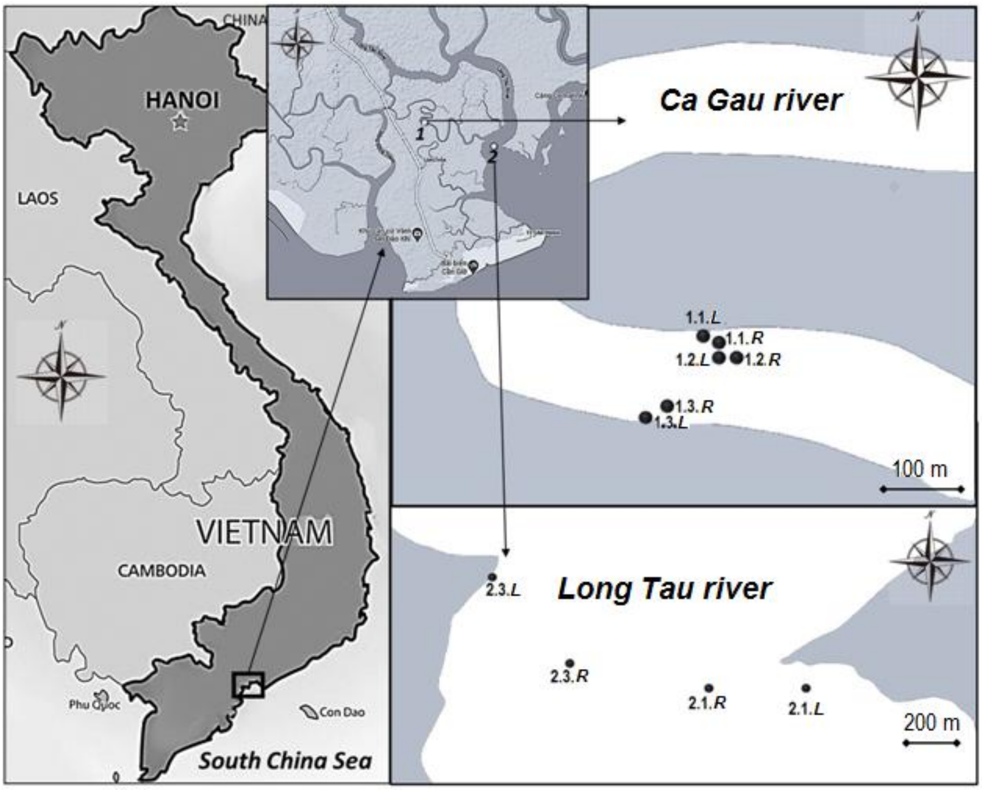

F i g . 1 . Map of sampling bottom sediment stations in the Ca Gau and Long Tau rivers in the Can Gio Biosphere Reserve, May 2021 (*R* is for sampling stations at low tide, *L* – at high tide)

FSM-1201 [1), 2)]. CES and OH concentrations were converted to 100 g weight of air-dry weight of sediments. Correlation analysis (p = 0.05) was performed using a Microsoft Excel 2010 analysis package.

Results and discussion

Bottom sediment sampling stations (Areas 1, 2) are located in river reaches in the zone of tidal influence. Water dynamics impacted on changes in physical-chemical water parameters (Fig. 2). During the high tide, water salinity increased by 1 PSU in the water area of Area 1 and by 5 PSU in Area 2 located almost at the mouth of the Long Tau River. Salinity increase in the river water during high tides is natural and related to the inflow of saltier sea water. Following the salinity

---

[1)] Matveeva, I.S. and Ignatchenko, A.V., 2014. [*РД 52.10.803-2013. Weight Content of Petroleum Hydrocarbons in Marine Sediment Samples. Methodology for Measurements by Infrared Spectrometry*]. Moscow, 24 p. (in Russian).

[2)] Oradovskiy, S.G., ed., 1977. [*Guideline for Methods of Sea Water Chemical Analysis*]. Leningrad: Gidrometeoizdat, 118–131 p. (in Russian).

gradient, physical-chemical characteristics of water changed (Fig. 2): hydrogen ion concentration shifted towards alkalinity; redox potential slightly decreased. Redox potential slightly decreased. The decrease of Eh values (down to –40 mV) during the high tide is consistent with the increase of pH values (up to 7.58). This fact indicates an improvement in oxygen conditions when the seawater enters the river water in the studied wetlands [6]. The change in pH values (in Area 1 water area by 0.24 units on average and in Area 2 by 0.31 units) was more pronounced than the change in redox potential. Similar fluctuations in pH due to water movement within the tidal cycle were observed in other estuarine systems [7, 8]. Water temperature tended to increase during the high tide. At low tide, the mean value of surface water temperature was 29.5 °C in Area 1 and 29.9 °C in Area 2; at high tide it was 30.0 °C in Area 1 and 30.2 °C in Area 2. The tide was at night (9–10 p.m.), which may have been a factor in the decrease in surface water temperature. The tide was in the afternoon (around 3 p.m.), when the surface water could be warmed by the sun's rays. According to long-term satellite observations, the average sea water temperature off the coast of Kan Gio Reserve in May is 29.8°C, ranging from 28.6 to 31.0 °C (URL: https://www.seatemperature.org/asia/vietnam/cn-th-may.htm). The fact that the temperatures recorded at high tide are higher than

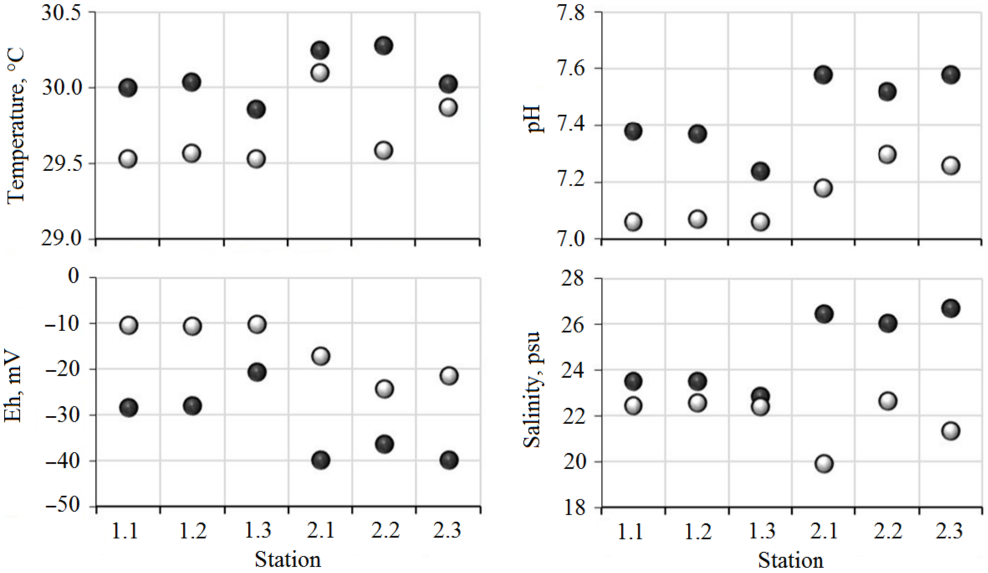

F i g . 2 . Physico-chemical parameters of water at the bottom sediments sampling stations at low tide (●) and high tide (○) in the Ca Gau and Long Tau rivers in the Can Gio Biosphere Reserve, May 2021 the long-term observations may indicate that the surface water warms up during the day, which was recorded during the survey.

Concentrations of CES in bottom sediments in the coastal water area of Kan Gio Reserve ranged from 54 mg/100 g to 90 mg/100 g (Fig. 3). The maximum values of CES in Area 1 were found at Station 1.3 *R* and the minimum values – at Station 1.2 *R*; in Area 2 – at Stations 2.3 *L* and 2.3 *R*, respectively. The increased content of CES in the bottom sediments of the Ka Gau River compared with that of the Long Tau River may be due to the fact that the first area is located in the depth of the river system and the second area is at the direct influx of the river into the sea where organic-rich river water is diluted with marine water. A similar phenomenon has also been observed by other authors, where an increased content of organic matter in river sediments has generally been observed mainly in the river basins in the central part of the mangroves compared to those in their estuarine sections [9].

It is known [10] that the most active processes of primary diagenesis of organic matter take place at the water – bottom interface, so the previously noted changing pH and Eh values of water, which directly influence the course of these processes, may influence the quantitative indicators of organic matter accumulated in bottom sediments and transported by tidal currents. However, no close correlation between the concentration of organic matter and physical-chemical indicators of water was observed, with the exception of a weak positive correlation for salinity (r = 0.48). Although in our case it is difficult to speak about the relationship between salinity and the studied components of organic matter, the literature [11] contains data on a significant inverse proportional relationship between the content of organic and inorganic matter and salinity[3]. The influence of these factors is probably hard to detect due to their variability over a short period of time making it impossible to determine the specifics of sedimentation conditions.

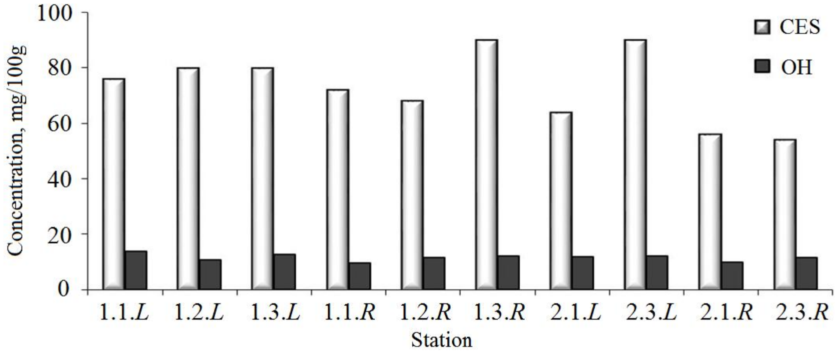

Fig. 3. CES and OH concentrations in bottom sediments of Ca Gau and Long Tau rivers in the Can Gio Biosphere Reserve, May 2021

---

[3] Ovsepyan, A.E., 2007. [*Distribution, Migration and Transformation of Mercury in the Northern Dvina Estuary*]. Ph.D. Thesis. Rostov-on-Don, 178 p. (in Russian).

A comparison of CES levels in river sediments, the composition of which changes due to their active transport by sea water, indicated that the total CES content was decreasing during low tide. In Area 1 (deep in the Kan Gio Peninsula), this decrease was negligible, but in Area 2 (the estuarine part of the Long Tau River), it decreased by almost 30 %. This is probably due to the fact that estuarine areas are generally characterized by intense circulation [4] and deposition [9] of various substances caused by water dynamics. A similar trend existed for OH but it was not significant. This is probably due to the low OH level and lack of significant differences in their content in both river and sea sediments.

There is a regional classification of levels of organic pollution in bottom sediments [12]:

- Level I – less than 50 mg/100 g;
- Level II – 50–100 mg/100 g;
- Level III – 100–500 mg/100 g;
- Level IV – 500–1000 mg/100 g;
- Level V, the most dangerous, – over 1,000 mg/100 g.

In accordance with this classification the values obtained in this study for the whole water area refer to pollution levels I–II, and the studied area can be classified as conditionally clean [13, 14]. These levels are comparable with similar indicators of coastal bottom sediments in other protected areas, in particular, the Kazantip Nature Reserve (North-Eastern Crimea) [15] and the Laspi Landscape Reserve (Southern Coast of Crimea) [16]. Recorded levels of organic matter are significantly lower than, e. g., in the estuarine part of the Yazna River, South-East Asia [17].

OH concentrations ranged from 9.6 mg/100 g to 13.8 mg/100 g (Fig. 3). If we compare the obtained results with the standards from Dutch Lists [5], the values were rather low and only by 1.9–2.8 times exceeded the concentration threshold, at which the exposure under chronic pollution is insignificant (5 mg/100 g). The percentage of OH in CES ranged from 13 % to 21 %. The obtained values indicate a low level of oil contamination, and therefore the recorded hydrocarbons are of predominantly autochthonous origin.

Conclusion

The recorded concentrations of chloroform-extractable compounds (54–90 mg/100g) and oil hydrocarbons (9.6–13.8 mg/100g) in bottom sediments of the Ka Gau and Long Tau Rivers (the buffer zone of Kan Gio Biosphere Reserve)

---

[4] Denisov, V.V., ed., 2004. [*Ecology. A College Textbook*]. Rostov: ITS MarT M, 672 p. (in Russian).

[5] Available at: esdat.net/Environmental%20Standards/Dutch/annexS_I2000Dutch%20Environmental%20Standards.pdf (Accessed: 5 September 2022).

are close to trace levels. Consequently, the status of this component of the river ecosystems is favourable in terms of organic and oil pollution content. Active water circulation in estuarine areas of mangrove rivers at high tide results in significant changes in physical-chemical environmental indicators: salinity increase (by 1–5 eps), pH increase (on average by 0.24–0.31 units), redox potential decrease (by 9–18 mV). However, no close correlation was found between changes in the physical-chemical characteristics of the environment and the content of CES and OH. This phenomenon is probably associated with the movement of bottom sediments and is only significant for CES in the estuarine part of the Long Tau River. In other cases we can only speak of a trend.

REFERENCES

1. Gugliotta, M., Saito, Y., Ta Thi Kim Oanh and Nguyen, V.L., 2019. Valley-Confinement and River-Tidal Controls on Channel Morphology along the Fluvial to Marine Transition Zone of the Đồng Nai River System, Vietnam. *Frontiers in Earth Science*, 7, p. 202. doi:10.3389/feart.2019.00202
2. Wu, Y., Zhang, J., Cho, K.W., Hong, G.H. and Chung, C.S., 2004. Origin and Transport of Sedimentary Organic Matter in the Yalujiang Estuary, North China. *Estuaries*, 27(4), 583–592. Available at: http://www.jstor.org/stable/1353472 [accessed: 15 August 2022].
3. Gorbunov, A.O., Kovalev D.P. and Kovalev, P.D., 2019. The Sediment Transported by the Flow in the Eroding Area of the Mordvinov Gulf Coast (Sakhalin Island). *Geosystems of Transition Zones*, 3(2), pp. 209–218. doi:10.30730/2541-8912.2019.3.2.209-218 (in Russian).
4. Krein, A. and Schorer, M., 2000. Road Runoff Pollution by Polycyclic Aromatic Hydrocarbons and its Contribution to River Sediments. *Water Research*, 34(16), pp. 4110–4115. https://doi.org/10.1016/S0043-1354(00)00156-1
5. Burgess, R.M., Terletskaya, A.V., Milyukin, M.V., Povolotskii, M., Demchenko, V.Y., Bogoslavskaya, T.A., Topkin, Yu.V., Vorobyova, T.V., Petrov A.N. [et al.], 2009. Concentration and Distribution of Hydrophobic Organic Contaminants and Metals in the Estuaries of Ukraine. *Marine Pollution Bulletin*, 58(8), pp. 1103–1115. https://doi.org/10.1016/j.marpolbul.2009.04.013
6. Shigaeva, T.D., Polyak, Yu.M. and Kudryavtseva, V.A., 2020. The Redox potential as an Index of the State of Environmental Entities. *Biosfera*, 12(3), pp. 111–124. doi:10.24855/BIOSFERA.V12I3.549 (in Russian).
7. Jansen, S., Walpersdorf, E., Werner, U., Billerbeck, M., Böttcher, M.E. and de Beer, D., 2009. Functioning of Intertidal Flats Inferred from Temporal and Spatial Dynamics of O_2, H_2S and pH in their Surface Sediment. *Ocean Dynamics*, 59, pp. 317–332. doi:10.1007/s10236-009-0179-4
8. Davies, O.A., 2014. Tidal Influence on the Physico-Chemistry Quality of Okpoka Creek, Nigeria. *International Journal of Biological Sciences and Applications*, 1(3), pp. 113–123. http://article.aascit.org/file/pdf/9030758.pdf [accessed: 15 August 2022].
9. Tam, N.F.Y. and Wong, Y.S., 2000. Spatial Variation of Heavy Metals in Surface Sediments of Hong Kong Mangrove Swamps. *Environmental Pollution*, 110(2), pp. 195–205. doi:10.1016/s0269-7491(99)00310-3
10. Belkina, N.A., 2015. [The Role of Bottom Sediments in the Formation of the Chemical Composition of Surface Waters in the Humid Zone (Case Study of Lakes in Karelia)]. In: V. G. Pryazhinskaya, ed., 2015. [*Scientific support for the implementation of the Water Strategy of the Russian Federation until 2020: Collection of Academic Papers, Petrozavodsk, 6–11 July 2015*]. Petrozavodsk: Karelian Research Centre, RAS, pp. 395–400 (in Russian).

11. Lomakin, P.D., 2018. Field of the Dissolved Organic Matter Content in the Taganrog Bay (the Sea of Azov). *Physical Oceanography*, 25(6), pp. 459–471. doi:10.22449/1573-160X-2018-6-459-471
12. Tikhonova, E.A., 2021. Organic Matter of Bottom Sediments of the Crimean and Caucasian Coasts (Azov and Black Seas). *Ecological Safety of Coastal and Shelf Zones of Sea*, (3), pp. 52–67. doi:10.22449/2413-5577-2021-3-52-67 (in Russian).
13. Tikhonova, E.A., Kotelyanets, E.A. and Soloveva, O.V., 2021. Sea Bottom Sediments Pollution of the Crimean Coast (The Black and Azov Seas). In: T. Chaplina, ed., 2021. *Processes in GeoMedia. Vol. 2*. Cham, Switzerland: Springer Nature Switzerland AG, pp. 199–211. https://doi.org/10.1007/978-3-030-53521-6_23
14. Mironov, O.G., Milovidova, N.Yu. and Kiryukhina, L.N., 1986. On Maximum Permissible Concentrations of Petroleum Products in Bottom Sediments of the Black Sea Littoral. *Hydrobiological Journal*, 22(6), pp. 76–78 (in Russian).
15. Tikhonova, E.A., Soloveva, O.V. and Burdiyan, N.V., 2022. Bottom Sediments of the Kazantip Nature Reserve Coastal Water Area (Azov Sea) as an Indicator of the Water Area Wellbeing. In: T. Chaplina, ed., 2022. *Processes in GeoMedia*, *Vol. 5*. Cham, Switzerland: Springer Nature Switzerland AG, pp. 253–262. https://doi.org/10.1007/978-3-030-85851-3_28
16. Tikhonova, E.A., Soloveva, O.V., Mironov, O.A. and Burdiyan, N.V., 2020. Sanitary and Biological Characteristics of the Laspi Reserve Coastal Waters (the Black Sea). *Ecological Safety of Coastal and Shelf Zones of Sea*, (3), pp. 95–106. doi:10.22449/2413-5577-2020-3-95-106 (in Russian).
17. Han, L., Wang, Y., Xu, Y., Wang, Y., Zheng, Y. and Wu, J., 2021. Water- and Base-Extractable Organic Matter in Sediments From Lower Yangtze River-Estuary-East China Sea Continuum: Insight Into Accumulation of Organic Carbon in the River-Dominated Margin. *Frontiers in Marine Science*, 8, 617241. doi:10.3389/fmars.2021.617241

Submitted 10.06.2022; accepted after review 25.06.2022;
revised 6.07.2022; published 26.09.2022

About the authors:

Elena A. Tikhonova, Senior Research Associate, A. O. Kovalevsky Institute of Biology of the Southern Seas of RAS (2 Nakhimova Ave, Sevastopol, 299011, Russian Federation), Ph.D. (Biol.), **ORCID ID: 0000-0002-9137-087X, Scopus Author ID: 57208495804, ResearcherID: X-8524-2019**, *tihonoval@mail.ru*

Olga V. Soloveva, Senior Research Associate, A. O. Kovalevsky Institute of Biology of the Southern Seas of RAS (2 Nakhimova Ave, Sevastopol, 299011, Russian Federation), Ph.D. (Biol.), **ORCID ID: 0000-0002-1283-4593, Scopus Author ID: 57208499211, ResearcherID: X-4793-2019**, *kozl_ya_oly@mail.ru*

Nguyen Trong Hiep, Head of Laboratory, Southern Branch of Joint Vietnam-Russia Tropical Science and Technology Research Center, (No. 3, 3/2 St., Dist. 10, HoChiMinh, 740500, Vietnam), Ph.D. (Chem.), *hiepnguyen@vrtc.org.vn*

Contribution of the authors:

Elena A. Tikhonova – statement of the problem, determination of chloroform-extractable substances and oil hydrocarbons, discussion of the results

Olga V. Soloveva – analysis of the results obtained, discussion of the results, writing and formatting of the article

Nguyen Trong Hiep – sampling planning and sampling of bottom sediments, determination of physico-chemical parameters of water

All the authors have read and approved the final manuscript.

DOI: 10.22449/2413-5577-2023-3-128-141

Algorithmic and Software Data Registration of Hydrological Meters Based on the Distributed Thermoprofilemeters

P. V. Gaisky

Marine Hydrophysical Institute of RAS, Sevastopol, Russia
e-mail: gaysky@inbox.ru

Abstract

The paper describes developed and software-implemented algorithms for primary regulation and processing of measurement data of hydrological meters built on the basis of distributed temperature sensors – thermoprofilemeters. Thermoprofilemeters are spatial temperature sensors made of heat-sensitive continuous conductors (in particular, copper), which are laid in a busbar of a given length in a protective shell-tube. The spatial resolution of the meter is determined by the placement and length of each sensor section. Algorithmic-software data processing of conductor resistances makes it possible to recover temperature values averaged on sections of continuous profile using matrix of calibration coefficients. Interpolation and approximation of the resulting discrete series provides a calculation of the instantaneous spline profile of temperature, which is then used to sequentially plot a dynamic picture of the variability of the temperature field in the form of a colour gradient and isolines. In the online telemetry measurement mode, this method allows to clearly visualize the picture of spatial temperature distribution both during static installation of the sensor and during depth sensing, as well as algorithmically detect and control other hydrological parameters and processes in the aqueous medium: interfaces, surface and internal waves, upwelling, surge phenomena, vertical rates of transfer of water masses, etc. The spatial resolution and length of thermoprofilemeters can vary from several centimeters to tens of meters depending on the problems being solved. The use of sensors in hydrological measuring systems can be carried out in static and probing modes. At the same time, the application software for each type of sensor and measurement method allows using specialized data processing and display functions.

Keywords: program algorithm, distributed temperature sensor, thermoprofilemeter, isotherm, vertical profile, heat storage, thermocline, internal waves, temperature field, heat exchange, termistor chain

Acknowledgements: the research was performed under state assignment on topic no. 0555-2021-0004 of FSBSI FRC MHI RAS.

For citation: Gaisky, P.V., 2022. Algorithmic and Software Data Registration of Hydrological Meters Based on the Distributed Thermoprofilemeters. *Ecological Safety of Coastal and Shelf Zones of Sea*, (3), pp. 128–141. doi:10.22449/2413-5577-2022-3-128-141

Алгоритмически-программное обеспечение регистрации данных гидрологических измерителей на базе распределенных термопрофилемеров

П. В. Гайский

Морской гидрофизический институт РАН, Севастополь, Россия
e-mail: gaysky@inbox.ru

Аннотация

Описаны разработанные и реализованные программно алгоритмы первичной регистрации и обработки измерительных данных гидрологических измерителей, построенных на базе распределенных датчиков температуры – термопрофилемеров. Термопрофилемеры – пространственные датчики температуры, изготовленные из термочувствительных (в частности, медных) непрерывных проводников, ортогонально уложенных в шину заданной длины в защитной оболочке-трубке. Пространственное разрешение измерителя определяется укладкой и длиной каждого участка датчика. Алгоритмически-программная обработка данных сопротивлений проводников позволяет восстанавливать с помощью матриц градуировочных коэффициентов осредненные на участках непрерывного профиля значения температур. Интерполяция и аппроксимация полученного дискретного ряда обеспечивает расчет мгновенного сплайн-профиля температуры, который далее используется для последовательного построения динамической картины изменчивости поля температуры в виде цветового градиента и изолиний. В оперативном телеметрическом режиме измерений такой метод позволяет наглядно визуализировать картину пространственного распределения температуры как при статической установке датчика, так и при зондировании по глубине, а также алгоритмически обнаруживать и контролировать другие гидрологические параметры и процессы в водной среде: границы раздела, поверхностные и внутренние волны, апвеллинг, сгонно-нагонные явления, вертикальные скорости переноса водных масс и др. Пространственное разрешение и длина термопрофилемеров при изготовлении в зависимости от решаемых задач могут варьироваться от нескольких сантиметров до десятков метров. В гидрологических измерительных системах датчики могут применяться в статическом и зондирующем режимах. При этом прикладное программное обеспечение для каждого типа датчика и метода проведения измерений позволяет использовать специализированные функции обработки и отображения данных.

Ключевые слова: программный алгоритм, распределенный датчик температуры, термопрофилемер, изотерма, вертикальный профиль, теплозапас, термоклин, внутренние волны, поле температуры, теплообмен, термокоса

Благодарности: работа выполнена в рамках государственного задания ФГБУН ФИЦ МГИ по теме № 0555-2021-0004.

Для цитирования: *Гайский П. В.* Алгоритмически-программное обеспечение регистрации данных гидрологических измерителей на базе распределенных термопрофилемеров // Экологическая безопасность прибрежной и шельфовой зон моря. 2022. № 3. С. 128–141. doi:10.22449/2413-5577-2022-3-128-141

Introduction

Measurement of instantaneous spatial temperature profiles in the aquatic environment using distributed sensors or multipoint temperature transmitters from discrete sensors has been carried out for many years. The data obtained in this way are necessary for solving a number of hydrological problems, including monitoring and studying heat transfer and heat storage processes, detecting and studying the processes of water mass transfer through currents, surge phenomena and internal waves, monitoring boundaries of media separation and density distribution by heat transfer coefficients [1–10]. The electronic equipment of the measuring part of the sensors is being improved with the development of technical means and microelectronics, and new tasks of processing, comparison and analysis are set before the methodological and algorithmic-software parts. Along with the widespread relatively simple in technical implementation multipoint temperature transmitters [5–8], consisting of spatially discrete digital sensors, there are distributed temperature sensors – thermoprofilemeters (TP), built on the principle of orthogonally stacked thermally sensitive conductors [3, 10, 11]. Despite the relatively greater complexity in manufacturing and the need for individual calibration, TP have, in comparison with digital multipoint temperature transmitters, a number of advantages: greater measurement accuracy (error less than 0.1 °C), spatial continuity (the temperature in the area is constructively determined by averaging over the entire length, not at a point) and in some cases higher reliability due to the additional possibilities of a protective design and the absence of microelectronics in a controlled environment.

Equipment and data

The development and improvement of application software for working with the author's experimental and prototype TP samples [3, 10] has been carried out since 1996. During this time, distributed sensors for research in the Black Sea, in the Arctic and Antarctic regions, as well as for use on rivers and in systems for measuring the level and boundaries of media separation in coastal waters have been created. Since a number of created systems contain, in addition to TP, other measuring modules and sensors, let us focus on the algorithmic software for processing temperature profile data with spatial and temporal reference with a standard connection of the device to the computer interface via serial hardware (RS232/485) or virtual (USB modules, Bluetooth, etc.) COM port of the computer.

When creating the main specialized dialog software, Borland Pascal and C (MS DOS), C++ and Delphi (MS Windows) programming languages and environments were chronologically used. During the measurements, data were recorded and processed in autonomous and telemetric modes. In the post-processing mode, the primary tasks were the prompt preparation of reports and the transfer of visual numerical and graphical results to the data bank. Since the created hydrological TP had different lengths (from 20 cm to 50 m), spatial resolution (section length

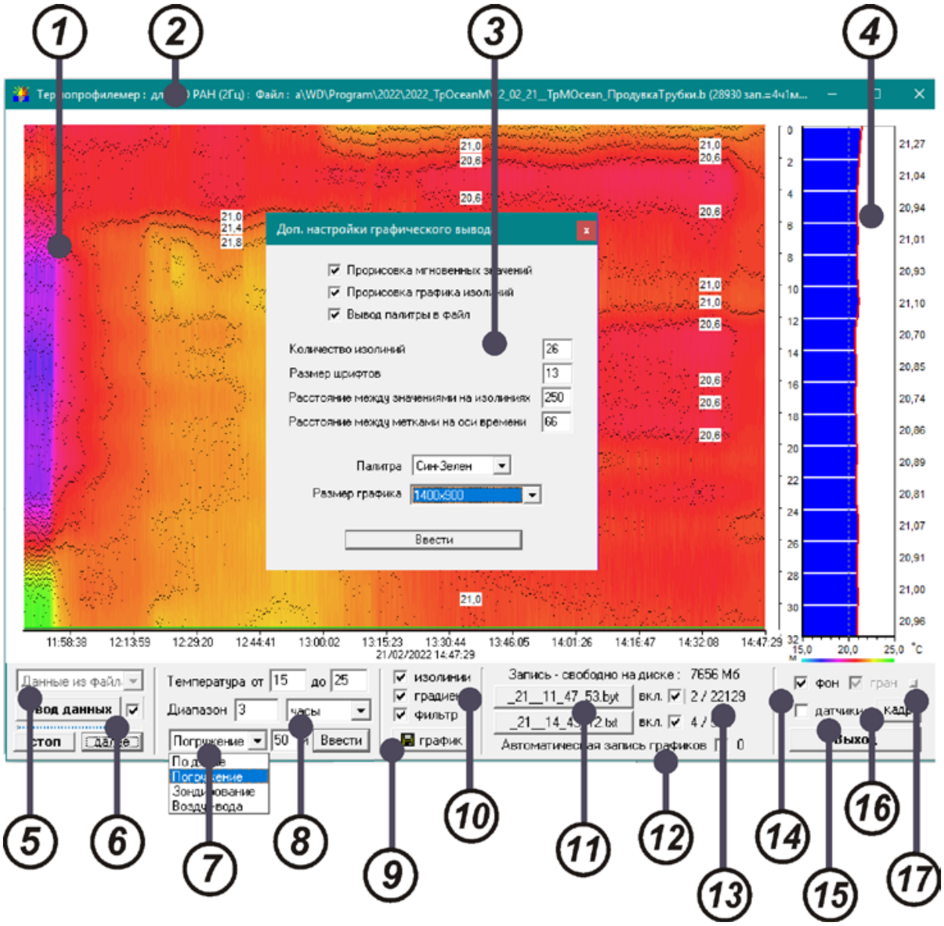

Доп. настройки графического вывод

☑ Прорисовка мгновенных з ачений

☑ Прорисовка графика изол ний

☑ Вывод палитры в файл

Количество изолиний 26

Размер шрифтов 13

Расстояние между значениями на изолиниях 250

Расстояние между метками на оси времени 66

Палитра Син-Зелен

Размер графика 1400x900

Ввести

Данные из файл

вод данных ☑

стоп

далее

Температура от 15 до 25

Диапазон 3 часы

Погружение 50

Ввести

По д е

Погр жение

Зонди ование

Возд -вода

☑ изолинии

☑ градие

☑ фильтр

график

Запись - свободно на диске : 7656 Мб

_21__11_47_53.byt вкл. ☑ 2 / 22129

_21__14_4 12.txt вкл. ☑ 4 /

Автоматическая запись графиков ☐ 0

☑ фон ☑ гран

☐ датчики

Кадр

Выхо

F i g . 1 . View of the main window of the program interface for initial recording and processing of measuring data of thermoprofilemeters: *1* – gradient and temperature profile isolines over time area; *2* – information line; *3* – advanced graphics window settings and temperature isolines output; *4* – moment averaged temperature values in sections and calculated spline-interpolated profile; *5* – control and indication of data input (from file (post-processing) / from COM port (telemetry mode)); *6* – flow control and input indication of primary data; *7* – selection of graphical mode of measurement data display with reference to depth or space; *8* – settings of time ranges and temperature scale of graphic output; *9* – option of saving graphs to files (bmp/jpg); *10* – setting options for isolines output, color gradient, median filtering and data averaging; *11* – options for recording primary data and measurement results into files (code (byt) and text (dat/txt)); *12* – option for settings of automatic frame-by-frame saving of graphs to graphic files; *13* – indication for recording code files and text files of measurement processing results; *14* – adjustment of the background of graphs (black/white); *15* – option for displaying the window of numerical and graphical output of secondary sensor data (pressure sensors, etc.); *16* – option of displaying the window of numerical output of statistical and code values as well as settings for post-processing of data; *17* – selection of the calibration coefficient file from 2 cm to 2 m), and also different applications (stationary, towed and sounding), universal software algorithms for processing primary information and graphical output were developed, which allow, under various experimental conditions, to quickly observe the dynamics of the temperature field with direct reference to space and time (Fig. 1). Unlike the output of a standard set of graphs, which is most often used for discrete sensors of multipoint temperature transmitters on separately specified horizons [1, 4, 6–9], this type of measurement information display is preferable. However, it can only be ensured by obtaining highly accurate and methodically complete primary data.

Results

The complete package of algorithmic software for TP includes a number of separate programs:

– program for modeling distributed sensors in terms of length, spatial resolution, matrices of orthogonal functions and materials for the manufacture of temperature-sensitive elements for specified application conditions (real dynamics and spatial variability of temperature profiles);

– program for metrological verification of the sensor and automatic calculation of matrices of calibration coefficients for TP sections;

– program for numerical and graphical display and registration of TP measurement data [1];

– complex data processing program.

In the user mode, a dialog program for primary registration and processing of measurement data is used (Fig. 1).

The use of hydrological TP when using up to two built-in pressure sensors (depth control) is carried out in four main modes (Fig. 2). Binding of the measuring temperature profile to the depth or boundaries of media separation (air and water) in stationary (platform, pier, moored buoy) or dynamic (bleeding, sounding, towing, submerged or surface drifting buoy) modes is provided depending on the tasks and equipment with pressure sensors. Accordingly, the user sets (Fig. 1 (designation *7*)) the selected type of measurement information display. The simplest option in this case is a stationary setting of a TP with a rigid spatial reference of the sensor to a given profile and primary boundaries of media separation without using pressure sensors (Fig. 2, *a*).

---

[1] Gaisky, P.V., 2022. [*Program for Registration and Processing of Thermoprofilemeter Measurement Data "THERMOPROF"*]. Sevastopol: MHI. State Registration no. 2022611315.

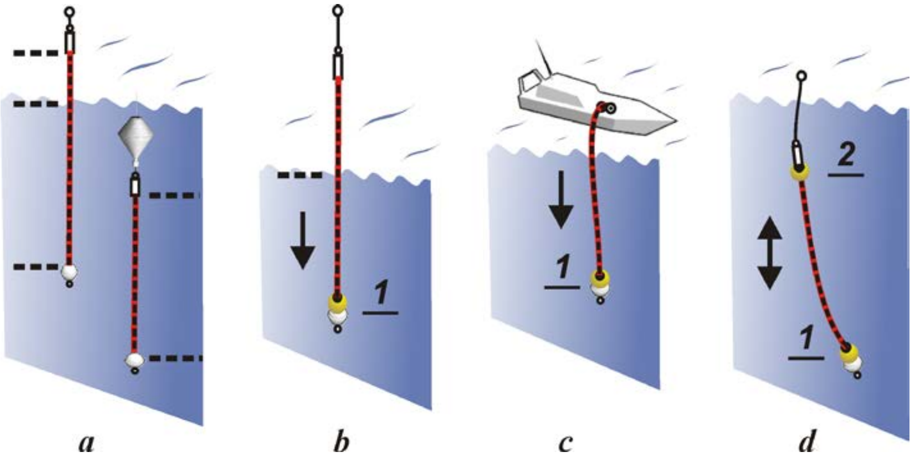

F i g . 2 . Methods of setting and using hydrological distributed sensors: stationary (rigid binding to spatial coordinates and boundaries of media separation) (*a*), vertical installation or sounding with one pressure sensor in the lower part (*b*), bleeding or towing from the side of the floating craft with one pressure sensor in the lower part (*c*), towing or sounding with two pressure sensors at the upper and lower ends of the thermoprofilemeter (*d*) (*1*, *2* – pressure sensor position)

The construction of measurement graphs is carried out in the telemetric mode, including in the data post-processing mode. The right side displays instantaneous temperature values in the form of columnar (conditionally discrete) diagrams calculated for all distributed sections of the TP profile (Fig. 3). This data is used to reconstruct a continuous approximated profile using spline interpolation. In this case, the spline coefficients are calculated and are quantitatively equal to a number of graph points for the current vertical graphic resolution of the user's display.

Despite the achievement of almost zero deviation from the uniformly discrete initial data of the primary measurement series, the spline in some cases exhibits intermediate outliers (Fig. 4), when the spline bend goes beyond the values of neighboring boundary points. Statistical analysis of these calculated outliers with the initially correct correspondence of the design resolution of the TP to the spatial variability of temperature in a controlled environment (which can be determined, if necessary, by preliminary modeling using real data) showed their error in 99 % of the cases. Correction of these outliers upon detection is carried out automatically (Fig. 4) using logarithmic or power-law interpolation on a given segment, depending on the nature of the deviation

$$T = a + b \times \log_{10} X \quad \text{and} \quad T = \pm a \times X^{b},$$

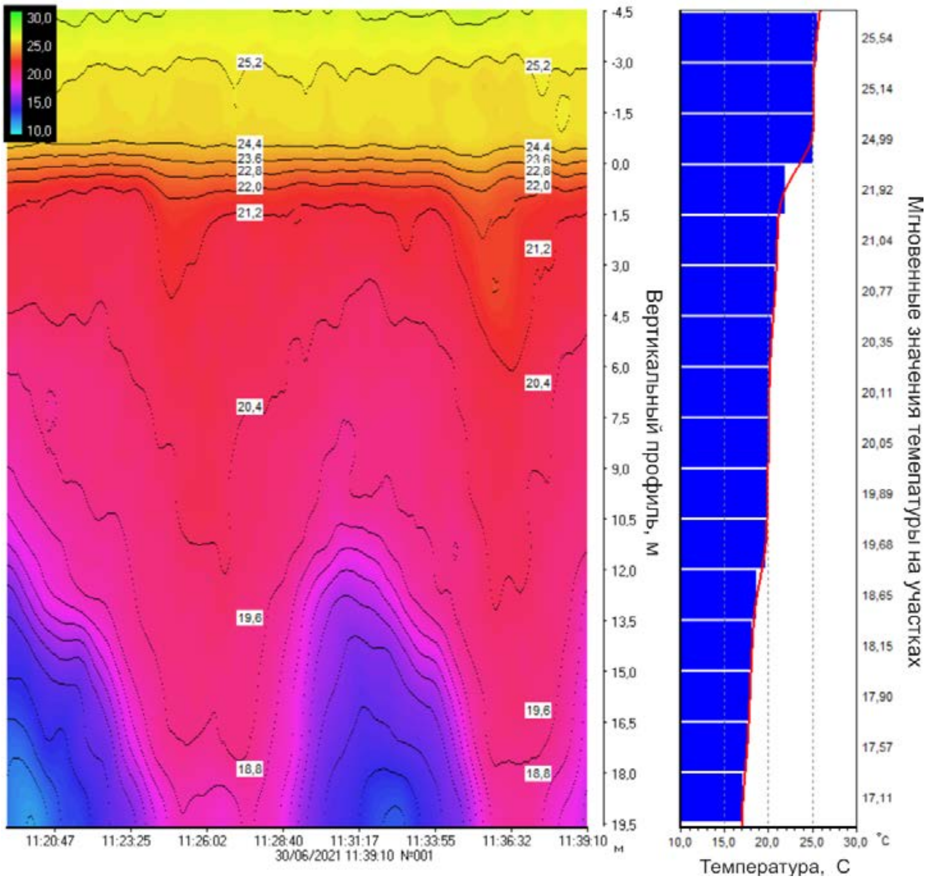

Fig. 3. Example of graphical display of measurements on oceanographic platform of thermoprofilemeter fixed vertically at air-water interface up to a depth of 19.5 m

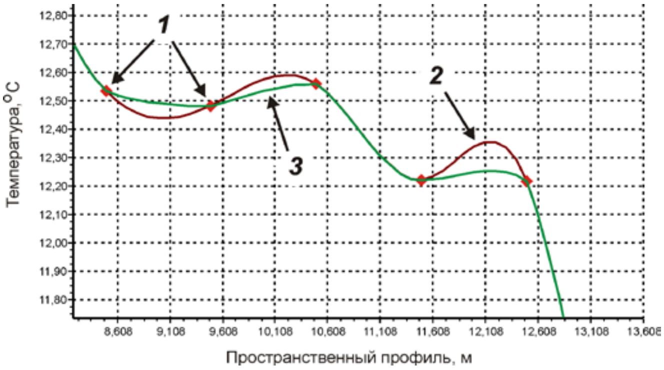

Fig. 4. Example of additional correction of the spline section of temperature measurement: initial measurement data on thermoprofilemeter sections (*1*), calculated profile after spline interpolation (*2*), resulting continuous profile after correction (*3*)

where *X* is spatial coordinate of a point; *T* is calculated temperature at the point; *a* and *b* are interpolation coefficients.

The resulting graphical pixel-continuous temperature profile series is compared with a user-specified color gradient over the range and displayed on the window of graphs (isolines) along the time base. The drawing of the isoline point on the resulting gradient strip is ensured by hitting the specified value of the isoline in the interval of value of neighboring pixels. Thus, in a given time range, regardless of previous measurements, a picture of the temperature field is formed sequentially with shifts in dynamics and with reference to a spatial profile. This method makes it possible to display the gradient and isolines promptly without two-dimensional interpolation, which requires long-term data accumulation and much more computational resources. However, the guarantee of the visual quality of this processing, expressed in the smoothness of the gradient and continuity of the isolines, is reliability (in terms of errors, inertia and spatial resolution) of the obtained primary measurement information.

Graphical display of TP data in dynamic operating modes (when changing position in space) is based on data from hydrostatic pressure sensors and user settings of the program. In particular, the “Immersion” program mode optimally displays the measurements obtained by bleeding the lower part of the TP from the vessel into the water (Fig. 5). The depth of the sensor is fixed according to the readings of the lower pressure sensor (Fig. 6), while the upper part is on the deck. In this case, interpolation and output to the isoline graph is carried out only for the submerged part. Provided that the underwater part of the TP is located vertically, the spatial reference of measurements will be correct, otherwise the depth can be corrected only if there are visual marks on the sensor or there is a pronounced temperature difference between water and air. To obtain a reliable vertical profile, it is also necessary to take into account the inertia of the sensor (Fig. 5) and the ship's motions during towing (Fig. 6).

An example of operation of “Sounding” program mode when using two pressure sensors is shown in Fig. 7. The TP position is assumed to be conditionally linear in depth.

One of the most important tasks in the application of hydrological TP is detection of internal waves and control of their parameters. Since the internal wave manifestation is well tracked in the thermocline region, where, with the proposed graphical display, the highest concentration of continuous temperature isolines is observed, it is proposed to use data on spatio-temporal characteristics of the isoline

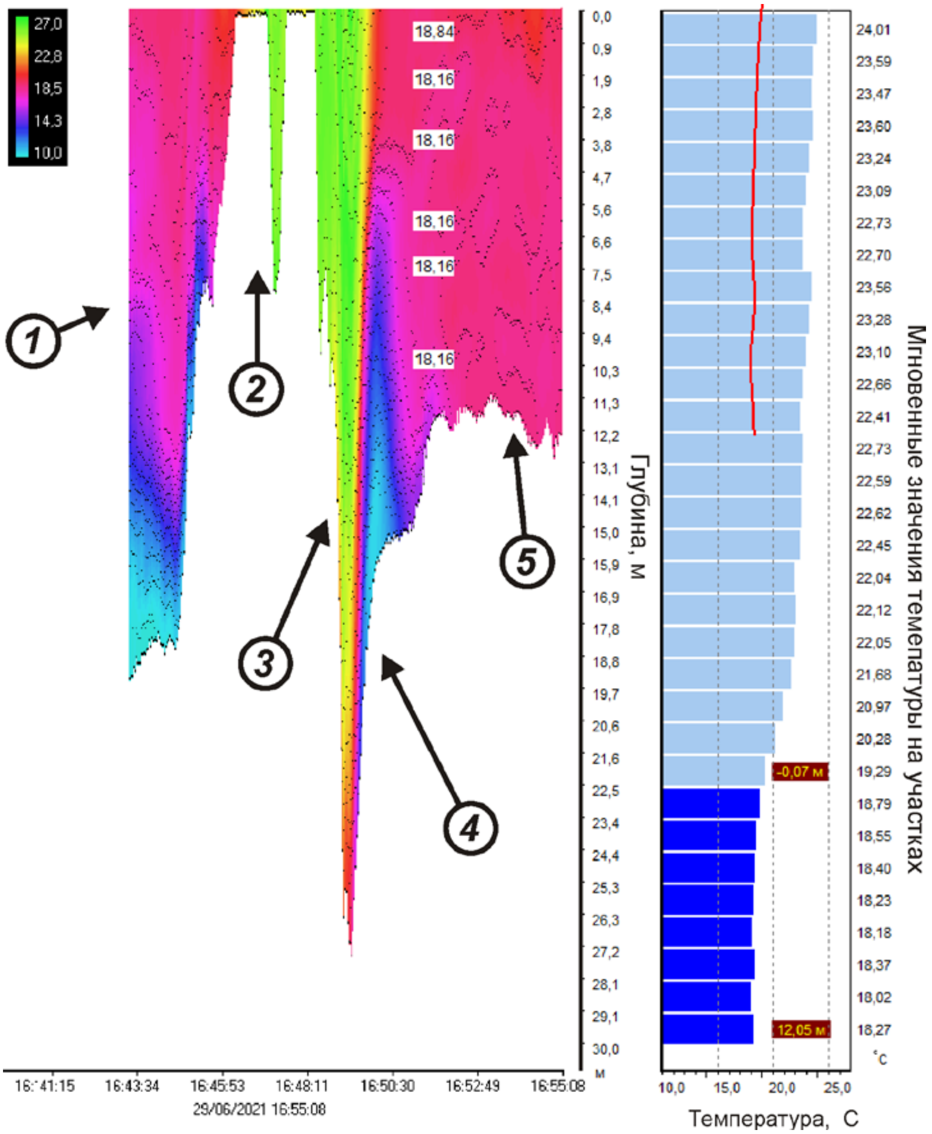

Fig. 5. Example of recording measurements during immersing and towing of the buried part of the TP: the end of towing (*1*), lifting on board (*2*), partial immersing overboard and inertial cooling (3), the beginning of towing and inertial heating (*4*), drift and surface swell (*5*)

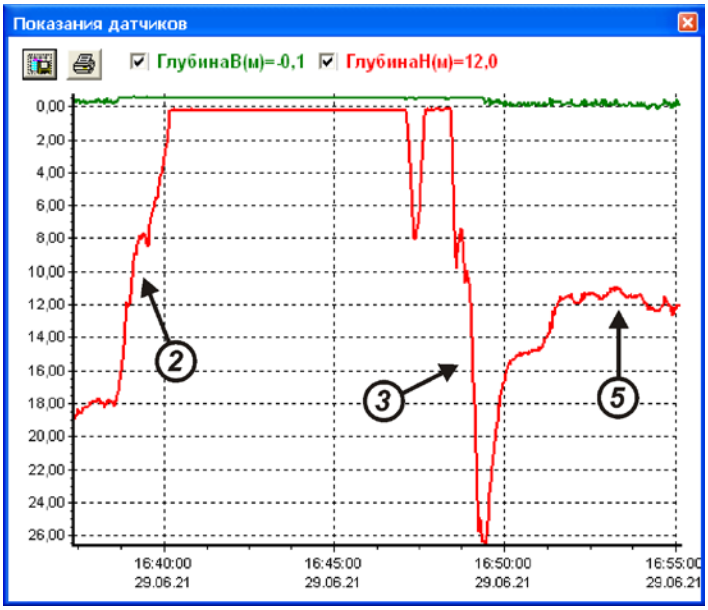

Показания датчиков

☑ ГлубинаВ(м)=-0,1 ☑ ГлубинаН(м)=12,0

F i g . 6 . Readings of device pressure sensors (upper and lower) to record measurements in Fig. 5: lifting onboard (*2*), partial immersing overboard (*3*), drift and surface swell (*5*)

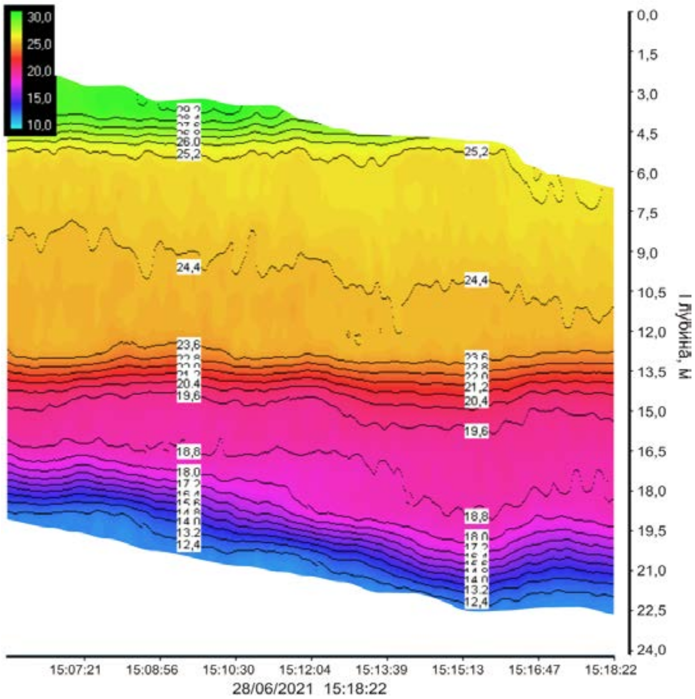

F i g . 7 . Example of plotting isolines in "Sounding" mode

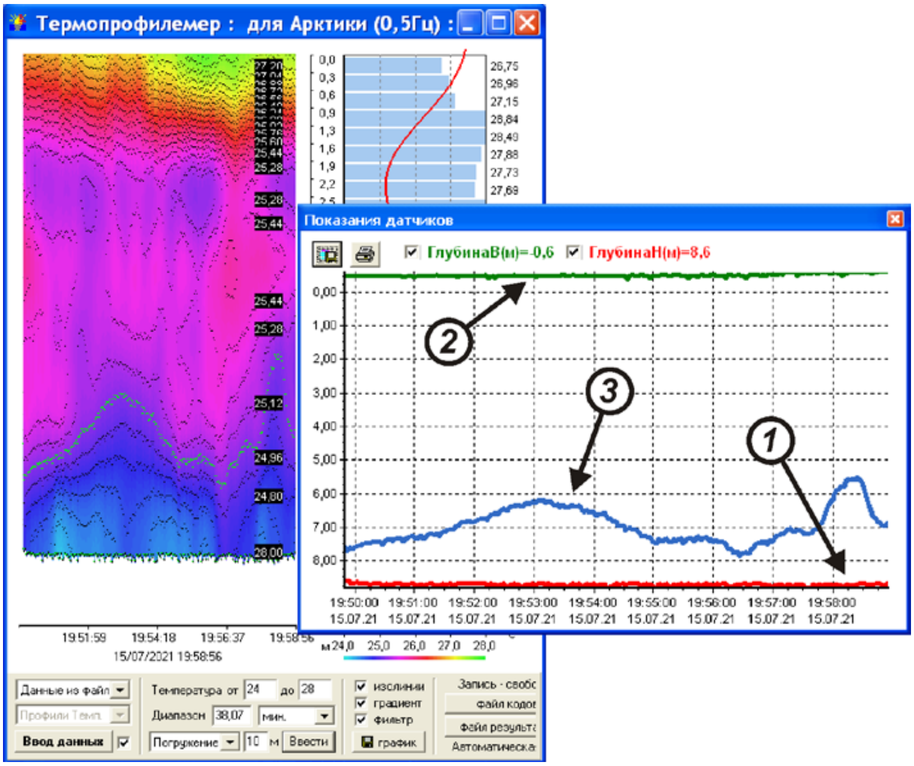

Температура от 24 до 28

Диапазон 38,07 мин.

Погружение 10 м

☑ изолинии

☑ градиент

☑ фильтр

F i g . 8 . Tracking and output graph of user selected isotherm: lower pressure sensor plot (*1*), upper pressure sensor plot (*2*), plot of monitored (from depth bottom) isotherm 25.12 °C (*3*)

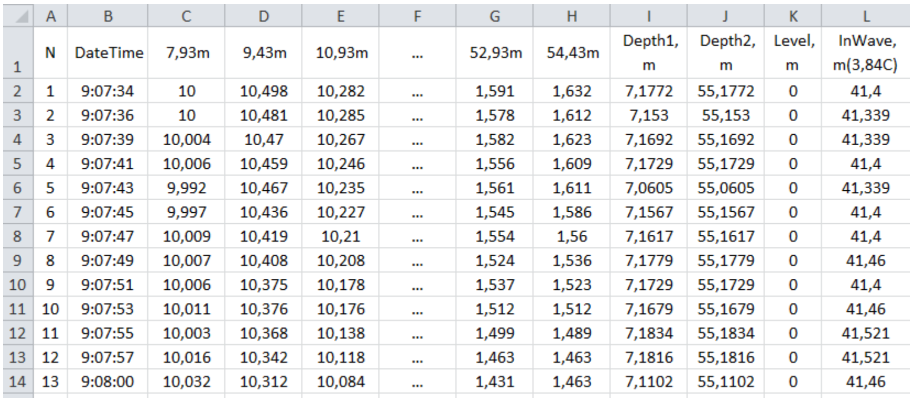

	A	B	C	D	E	F	G	H	I	J	K	L
1	N	DateTime	7,93m	9,43m	10,93m	...	52,93m	54,43m	Depth1, m	Depth2, m	Level, m	InWave, m(3,84C)
2	1	9:07:34	10	10,498	10,282	...	1,591	1,632	7,1772	55,1772	0	41,4
3	2	9:07:36	10	10,481	10,285	...	1,578	1,612	7,153	55,153	0	41,339
4	3	9:07:39	10,004	10,47	10,267	...	1,582	1,623	7,1692	55,1692	0	41,339
5	4	9:07:41	10,006	10,459	10,246	...	1,556	1,609	7,1729	55,1729	0	41,4
6	5	9:07:43	9,992	10,467	10,235	...	1,561	1,611	7,0605	55,0605	0	41,339
7	6	9:07:45	9,997	10,436	10,227	...	1,545	1,586	7,1567	55,1567	0	41,4
8	7	9:07:47	10,009	10,419	10,21	...	1,554	1,56	7,1617	55,1617	0	41,4
9	8	9:07:49	10,007	10,408	10,208	...	1,524	1,536	7,1779	55,1779	0	41,46
10	9	9:07:51	10,006	10,375	10,178	...	1,537	1,523	7,1729	55,1729	0	41,4
11	10	9:07:53	10,011	10,376	10,176	...	1,512	1,512	7,1679	55,1679	0	41,46
12	11	9:07:55	10,003	10,368	10,138	...	1,499	1,489	7,1834	55,1834	0	41,521
13	12	9:07:57	10,016	10,342	10,118	...	1,463	1,463	7,1816	55,1816	0	41,521
14	13	9:08:00	10,032	10,312	10,084	...	1,431	1,463	7,1102	55,1102	0	41,46

F i g . 9 . Example of writing a 48-meter TP sensor measurement results to a text file

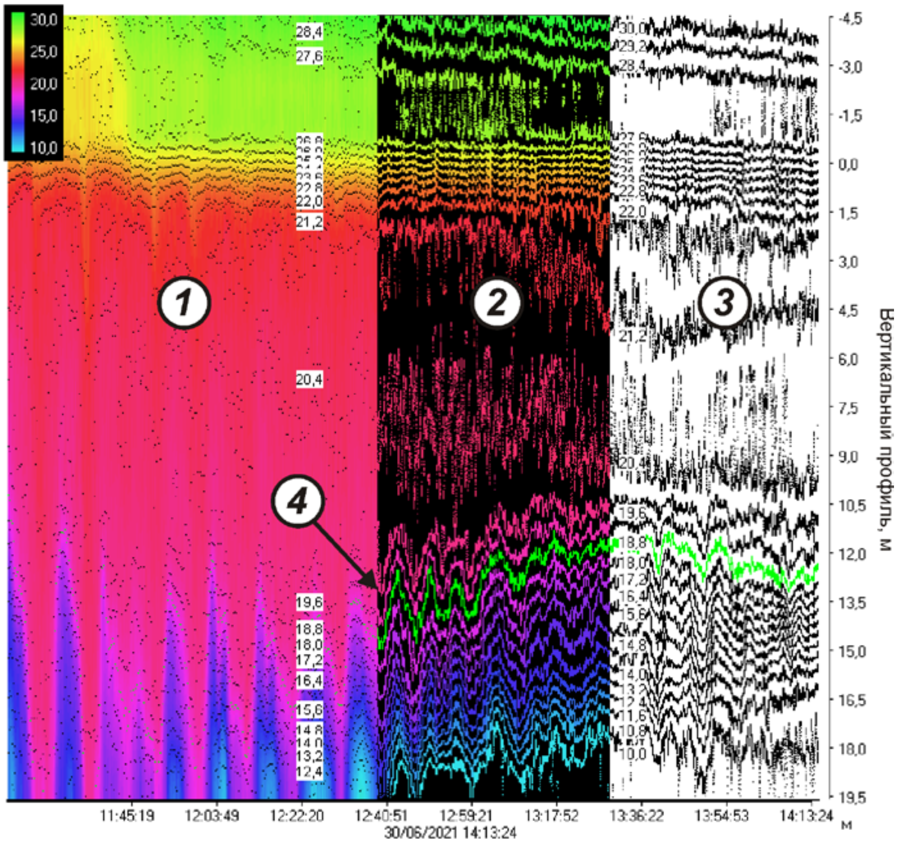

Fig. 10. Demonstration of the output of the gradient-isolines graph at various settings: colour gradient and isolines (*1*), colour isolines without gradient (*2*), black-and-white output of isolines (*3*), indication of the selected internal wave isoline (*4*)

selected by the user for spectral-wave analysis. In this case, the selected isoline, when processing measurements, is marked with a separate color and displayed on the graph (Fig. 8), and its spatial displacements in depth and time are recorded in the general text file of the results (Fig. 9).

Various modes of information output on isoline graphs are shown in Fig. 10. The time ranges for the output of isolines are set by the width of the time interval with an automatic shift of the graph to the left when a new data packet is received on the right. For the post-processing mode, one can set a specific time interval with a start and an end. The daily display mode uses a 24-hour scale. For processing large data arrays or for telemetric operation of the device in an offline mode, automatic frame-by-frame (daily, etc.) saving of graph windows and text files of measurement results in standard formats is provided.

Conclusion

As practical experience has shown, the developed algorithmic software for the primary registration, processing and numerical and graphical output of measurement data from hydrological distributed temperature sensors TP is a reliable tool for obtaining operational and visual information about the processes of heat transfer and transfer of thermally bound masses in water environment. The possibility of adaptive display of data in various modes of using the TP provides high-quality telemetric binding of measurements to spatio-temporal coordinates and, therefore, accelerates further interpretation of the results and planning of experiments. A necessary factor in obtaining reliable graphic information is qualitative metrological characteristics of the meter and a verified method of its use in specific conditions of environmental variability.

REFERENCES

1. Ocherednik, V.V., Baranov, V.I., Zatsepin, A.G. and Kyklev, S.B., 2018. Thermochains of the Southern Branch, Shirshov Institute of Oceanology, Russian Academy of Sciences: Design, Methods, and Results of Metrological Investigations of Sensors. *Oceanology,* 58(5), pp. 661–671. https://doi.org/10.1134/S0001437018050090
2. Nikolaev, N.I., Vasilyeva, N.V. and Nikolaeva, I.V., 2021. Development of a Device for Remote Monitoring of “Thermo-Braid” Temperature Environment. *Science and Business: Ways of Development*, (11), pp. 17–23 (in Russian).
3. Gaisky, V.A. and Gaisky, P.V., 2001. Distributed Thermoprofilometers and Their Capabilities in Oceanographic Investigations. *Physical Oceanography*, 11(6), pp. 543–577. https://doi.org/10.1007/BF02509846
4. Ocherednik, V.V. and Zapevalov, A.S., 2018. Investigation of the Short-Period Variability of the Temperature Field on the Black Sea Hydrophysical Training Ground of the Institute of Oceanology RAS. *Ecological Safety of Coastal and Shelf Zones of Sea*, (1), pp. 44–49. https://doi.org/10.22449/2413-5577-2018-1-44-49 (in Russian).
5. Tolstosheev, A.P., Lunev, E.G. and Motyzhev, S.V., 2014. Analysis of In-Situ Experiments with Temperature-profiling Drifters in the Black Sea and Other Areas of the World Ocean. *Morskoy Gidrofizicheskiy Zhurnal*, (5), pp. 9–32 (in Russian).
6. Motyzhev, S.V., 2016. Creation of Drifter Technology for the Ocean and the Atmosphere Monitoring. *Physical Oceanography*, (6), pp. 67–81. https://doi.org/10.22449/1573-160X-2016-6-67-81
7. Tolstosheev, A.P., Lunev, E.G. and Motyzhev, S.V., 2008. Research of the Upper Layer of the Black Sea by Means of Thermoproffiling Drifters. In: MHI, 2008. *Ekologicheskaya Bezopasnost' Pribrezhnykh i Shel'fovykh Zon i Kompleksnoe Ispol'zovanie Resursov Shel'fa* [Ecological Safety of Coastal and Shelf Zones and Comprehensive Use of Shelf Resources]. Sevastopol: MHI. Iss. 16, pp. 116–123 (in Russian).
8. Ocherednik, V.V., Silvestrova, K.P., Myslenkov, S.A. and Mashura, V.V., 2018.[Study of Internal Waves using Data of Three Anchored Thermistor Chains]. In: V. A. Gritsenko, 2018. [*Coastal Zone of Sea: Studies, Management, Prospects. Proceedings of the International Youth Summer School*]. Kaliningrad, pp. 12–16 (in Russian).

9. Dubravin, V.F., Kapustina, M.V. and Myslenkov, S.A., 2019. Intra-Annual Variability of the Diurnal Water Temperature Variations on Curonian-Sambian Plateau (South-Eastern Baltic Sea) in 2016. *Processes in GeoMedia*, (1), pp. 32–39 (in Russian).
10. Gayskiy, V.A. and Gayskiy, P.V., 2018. *Use of Distributed Sensors for Sea Temperature Measurements*. Sevastopol: IPTS, 175 p. https://doi.org/10.33075/978-5-6040795-4-6 (in Russian).
11. Gaysky, P.V., 2014. The Results of the Annual Observations of the Vertical Profile of Temperature on an Oceanographic Platform with Distributed Thermoprofiles. In: MHI, 2014. *Monitoring Systems of Environment*. Sevastopol: MHI. Iss. 20, pp. 44–53 (in Russian).

Submitted 13.05.2022; accepted after review 5.06.2022;
revised 08.07.2022; published 25.09.2022

About the author:

Pavel V. Gaisky, Leading Research Associate, Head of Innovation Marine Instrument Engineering Laboratory of SCU of Marine Hydrophysical Institute of RAS (2 Kapitanskaya St., Sevastopol, 299011, Russian Federation), Ph.D. (Tech.), **Scopus Author ID: 7801588003**, **SPIN-code: 7789-0658**, *gaysky@inbox.ru*

The author has read and approved the final manuscript.